NEUTRONS IN COINCIDENCE WITH INTERMEDIATE MASS FRAGMENTS AT LARGE ANGLES FROM ^{14}N + Ag REACTIONS AT 20 AND 35 MeV/NUCLEON

By

Charles Bloch

A DISSERTATION

Submitted to
Michigan State University
in partial fulfillment of the requirements
for the degree of

DOCTOR OF PHILOSOPHY

Department of Physics and Astronomy

1987

ABSTRACT

NEUTRONS IN COINCIDENCE WITH INTERMEDIATE MASS FRAGMENTS AT LARGE ANGLES FROM ^{14}N + Ag REACTIONS AT 20 AND 35 MeV/NUCLEON

By

Charles Bloch

The spectral shape and multiplicity of neutrons from the reaction of ^{14}N+Ag at E/A = 20 and 35 MeV have been measured for neutrons in coincidence with intermediate mass nuclei emitted at 50, 70 and 90°. The spectral shape clearly suggests two moving sources. The slower source velocity is about 65% of the center of mass velocity for E/A=35 MeV and 80% of the center of mass velocity for E/A=20 MeV (7% and 9% of the beam velocity, respectively). The faster source velocity is slightly less than half of the beam velocity for each case. Knowledge of the neutron multiplicity is necessary for models which attempt to explain the low effective temperature which has been determined from recent measurements of excited state populations. The data are also compared to the Harp-Miller-Bern exciton model. In addition, the neutron decay of excited states of ^{7}Li, ^{8}Li, ^{10}Be, ^{11}Be, and ^{12}B has been investigated in the same reactions. The production of these excited states is compared to that of the ground state and other states of lower excitation energy for each isotope investigated. Under the assumption of a Boltzmann distribution of excited state populations, each of these comparisons imply a nuclear temperature. Furthermore, the feeding of the ^{7}Li ground state from the neutron decay of the 2.255 MeV unbound state in ^{8}Li (one of those measured) is another process that could lead to low temperature observations in previous experiments. The degree of feeding is compared to predictions made by a quantum statistical model to determine the total feeding from all possible channels. The net effect of this feeding is applied to these and other recent nuclear temperature measurements to determine if the data are consistent with a single nuclear emission temperature characterizing the energies of these reactions. In general, temperatures in the 2-3 MeV range are obtained.

What the hell...To my wife Amy.

ACKNOWLEDGMENTS

First and foremost, I must offer my sincere thanks to my advisor, Walt Benenson. From the first day we met his relaxed attitude, patience, humor, and understanding helped me gain a perspective that was absolutely crucial to the completion of my degree. I think it is remarkable that from the first day I worked for Walt he gave me, a perfect stranger, support equal to that of my closest friends and relatives. For that I owe him my deepest gratitude. It was that kind of support that gave me the confidence to do what I set out to do. It certainly made my work as easy as it could be. I also wish to thank my other friends and relatives for all they have done for me. Thank you Dad, Mom, Diane, Jim Miller, Dave Bonner, Tim Meert, Lorry Inglehart, George, Jim Houthoofd, my in-laws, and of course my wife Amy.

In addition, I must thank many of my co-workers and professors for their help, without which I could not have attained this goal. I'll omit the nature of their contributions, but let me thank Brad Sherrill, Dave Morrissey, Mark Lowe, Ed Kashy, John Winfield, Dick Blue, Reg Ronningen, Aaron Galonsky, MrDave, Bruce Remington, Greg Caskey, RJ, the staff of the National Superconducting Cyclotron Laboratory, George Bertsch, Wayne Repko, Vic Pol, and Russ Wong.

Finally, let me thank my producer, my agent, members of the academy, and all the little people who are too numerous to mention. You know who you are, and I thank you.

TABLE OF CONTENTS

Page

Chapter

LIST OF TABLES

TABLE PAGE

LIST OF FIGURES

CHAPTER I: INTRODUCTION

The concept of nuclear temperature has been relatively successful in describing heavy ion reactions at both low (E/A<10 MeV) and high (E/A>100 MeV) bombarding energies [Pu77, Ne82, Mo86, We76, Cu80]. The question arises as to whether the concept of temperature can be applied to intermediate energy heavy ion collisions in the course of which temperatures should comparable to the binding energy of a nucleon in the nucleus. This is the region in which a liquid-gas phase transition has been estimated to take place [Cu83, Be83, Bo84a]. Much of the experimental [e.g. Ch83, Cu83, Ja83, Ly83, Fi84, Hi84b, Mo84, We84, Po85a, So86] and theoretical [e.g. Bl81, Fa82, Fr83b, Bo84a, Bl85, Ha86, Pa84, Pa85] work in this energy region focussed on thermodynamic aspects. Data in this energy range indicate that the fragment yields depend on a power law [Ch83] with the exponent in the range predicted by the thermal liquid drop model [Fi67] for condensation around a critical point. Toward determining the validity of the temperature assumptions in this energy region, we have investigated the reaction of ^{14}N+Ag at E/A=20 and 35 MeV.

An important component of reactions of this nature has been the observation of intermediate mass fragments ($4<A<A_{beam}$) at large angles in the lab ($\theta>>\theta_{grazing}$) [Me80, We82, We84, Wo85, Fi86]. The importance of the large lab angle is to reduce the contribution from quasi-elastic processes [Fi86]. This technique has shown to be successful at biasing the data toward central, high multiplicity events [Me80, Wo85]. There are many inclusive measurements of the spectra of such particles [Po71, Ch83, Ja83, Fi84, We84, Wo85, Ch86, Fi86]. Simple one step processes would not produce such large fragments at such large angles. One model that is fairly successful at describing the energy spectra of such fragments is the moving source model [Ja83]. In that description, a set of nucleons moving in the lab frame emit fragments thermally. The thermal assumption means that the emission direction is isotropic in the rest frame and that the energy dependence contains a factor of $e^{-E/kT}$, where E is fragment energy in the rest frame and kT is an emission temperature. Such spectra may contain particles from pre-equilibrium processes and hence would not reflect the true temperature. Contributions from such processes are forward peaked, and in order to select central collisions, we have excluded the forward angles. A limited angular range of measurements may have a greater responsibility for the success of the moving source model than the actual physics of a thermal source [Wo85, Ch86b, Fi86].

In order to see if the slope parameter extracted from such fits is actually a temperature, a second technique for measuring nuclear temperature was developed [Mo84]. This technique relies on measuring the distribution of nuclei in their various quantum states. If the nuclei are from a thermalized source, their population distribution in excited states should be Boltzmann-like (ignoring spin factors), and the temperature should be the same as that predicted by the moving source model. The A=7 nuclei are particularly simple temperature probes since they have only one bound excited state [Aj84]. For two levels in statistical equilibrium, the ratio, R, of the population of the excited state to the population of the ground state is given by:

$$R = \frac{(2j_1+1)}{(2j_0+1)} \times \exp\left(\frac{-\Delta E}{kT}\right) \qquad (I.1)$$

where j_0 and j_1 are the spins of the ground and excited states, respectively, and ΔE is the energy difference between the states [Do78]. Recent experiments have measured the production of bound excited states of intermediate mass fragments emitted at large angles from reaction ^{14}N+Ag at E/A=20, 25, and 35 MeV [Mo84, Mo85, Bl86].

These recently reported measurements of the production of bound excited states of ^{7}Li and ^{7}Be nuclei emitted at large angles from the reaction of ^{14}N+Ag at E/A=35 MeV [Mo84, Mo85, Bl86] indicated a large discrepancy between the temperature calculated from the excited state populations (about 0.5 MeV) and the temperature extracted from the shape of the particle kinetic energy spectra (about 12 MeV). In addition, recent measurements of unbound state populations in similar reactions, yielded temperatures around 5 MeV [Po85a, Ch86a]. Two mechanisms frequently discussed that might explain these discrepancies are final state interactions [Bo84b] and sequential decay [Ha86]. The present work reports on the direct investigation of the former, and a more indirect investigation of the latter. Both of these bases for the discrepancies result from the difficulty involved in directly measuring the original ground state population. Experimentally, the accessible quantities are: the population of the excited state, obtained by observing its associated γ ray and the total fragment production in the ground and γ-emitting states, obtained with a silicon ΔE-E telescope. Dividing those two numbers gives the fraction, f, of fragments in the excited state. The fraction is related to the temperature through the ratio, R, in the following ways:

$$f = \frac{R}{(1 + R)} \quad \text{or} \quad R = \frac{f}{(1 - f)}. \qquad (I.2)$$

A possible difficulty arises in this type of measurement in that one of the states in the ratio has a unique property. The ground state of most of the nuclei studied here it is unique in that it does not decay. This makes it more susceptible to problems caused by final state interactions and sequential decay.

If we produce an equilibrated system, it will emit fragments with a distribution of excited states described by equation (I.1). In the first experiments which used this idea, the populations of the excited states were determined by observing the γ ray emitted in the de-excitation. If the excited fragment interacts with other particles emitted from the same reaction, it can de-excite without emitting this γ ray. This is what is meant by "final state interactions". Boal made one attempt to calculate the effect of this process [Bo84b]. In addition to several theoretical assumptions, Boal was forced to estimate the associated neutron multiplicity since no data for this existed. The first goal of this experiment, was to measure these multiplicities. Previously, there have been many experiments with neutron coincidences e.g. [Hi79, Ga83, Ho83, Hi84a, Ca85, Ca86, De86a, De86b, Ho86, Re86]. But in all previous experiments, the neutrons were measured in coincidence with one or more of the following: projectile-like fragments, fission fragments, or evaporation residues. The present measurement is unique in that it is the first time that neutrons have been measured in coincidence with intermediate-mass fragments at large angles. Considering the significance of these fragments in intermediate energy heavy ion collisions, these measurements could be a very important key to understanding the mechanisms involved in these reactions. This thesis reports the associated neutron multiplicities for neutrons in coincidence with ^{6}Li, ^{7}Li, ^{8}Li, ^{7}Be, ^{9}Be, ^{10}Be, ^{10}B, and ^{11}B fragments observed at 50°, 70°, and 90° in the lab from the reaction of ^{14}N+Ag at both E/A=35 MeV and E/A=20 MeV.

In addition to measuring the associated neutron multiplicities, we were also able to observe quantitatively sequential decay of several intermediate mass fragments using a technique developed by Kiss et al. [Ki87]. These measurements are important in the attempt to resolve the discrepancies between nuclear temperatures extracted from various types of excited-state population measurements. Excited-state population temperature measurements can be divided into two categories: those that measure bound state populations and those that measure unbound state populations. This distinction seems to be important since more recent measurements of the populations of unbound states in light nuclei [Po85a, Ch86a] systematically yield higher temperatures (4 or 5 MeV) than do the measurements of bound state populations (temperatures from 0.5 to 1 MeV) [Mo84, Mo85, Bl86] for intermediate-energy (E/A=20 to 60 MeV) heavy-ion reactions.

Attempts to reconcile the differences described above have centered on preferential feeding of the ground state by sequential decay as discussed in Refs. Mo85 and Ha86. The bound state populations will, of course, fail to reflect the initial Boltzmann distribution if there is significant differential feeding of any of the observed states from particle unbound states in larger nuclei. This effect generally is expected to be greatest for those ratios which involve the ground state population. We have measured the extent of feeding from sequential decay for a system previously used in a bound state temperature measurement. This was done via a measurement of the neutron decay of the 2.255 MeV excited state of ^{8}Li nuclei observed from the reaction of ^{14}N+Ag at E/A=20 and 35 MeV. Specifically, the feeding of the ground state of ^{7}Li due to the production of the 2.255 MeV state in ^{8}Li has been measured.

In order to compare ^{7}Li excited state production to that of the ground state, a correction should be made for contamination of the ^{7}Li energy spectrum by pairs of α particles from the ground state decay of ^{8}Be [B186]. For this work, the nature of the contamination and the necessary correction are described in Appendix A. In the study of neutron decay of unbound states and to obtain absolute quantitative information about the excited state population, it is necessary to calculate the relative geometric efficiency of detecting the neutron from the particular decay. This calculation is described in detail in Appendix B. Comparison of the production of these two unbound states to the previously measured lower-lying excited states allows the calculation of a nuclear temperature. Furthermore, the fraction of the ^{7}Li and ^{6}Li nuclei from the neutron decay of these states is significant in that it can resolve some of the discrepancies between recent nuclear temperature measurements. In addition, neutron decay of the 7.371 MeV excited state of ^{10}Be, the 3.89 MeV excited state of ^{11}Be, and the 3.388 MeV excited state of ^{12}B was observed. Finally, while quantitative results were not obtained, it appears that the decay of the 1.69 MeV excited state of ^{9}Be has been observed.

The neutrons in coincidence with the intermediate mass fragments were binned in kinetic energy spectra. These spectra were fit with a two-source moving source model [Ja83]. This model has several benefits. First, it provides an excellent parameterization of the data in terms of six parameters. Two of the parameters in this model are the associated neutron multiplicities for the two apparent neutron sources. This allows us to extract immediately one of the physical quantities we are after, namely the associated neutron multiplicity. Second, this model provides an analytic expression for the neutron spectra (in the non-relativistic limit), which is easily integrated over solid angle to give an expression for the neutron energy distribution, $\frac{d\sigma}{dE}$. Putting the moving source fit parameters into that expression produces a histogram of the energy distribution. This histogram can be and is then readily compared to predictions made by a Harp-Miller-Berne Exciton Model as modified by Blann [Bl81]. A discussion of the physical implications of the other moving source parameters and the exciton model comparison is included. Finally, the sequential decay measurements are compared to predictions made by Hahn and Stocker's Quantum Statistical Model [Ha86]. The results are used to draw conclusions about the validity of the assumption of statistical equilibrium and to resolve apparent discrepancies of recent temperature measurements.

CHAPTER II: EXPERIMENTAL

II.1 Equipment

The experimental details are similar to those described in Re86. Neutrons and intermediate mass fragments were produced by the interaction of nitrogen ions with a silver target. Beams of 490 MeV $^{14}N^{5+}$ and 280 MeV $^{14}N^{4+}$ ions were provided by the K500 cyclotron of the National Superconducting Cyclotron Laboratory at Michigan State University. The cyclotron periods were 52.370 and 68.788 ns, respectively. The target was a self-supporting foil of natural silver, 1.8 mg/cm² thick. It was mounted in an aluminum target ladder inside a steel 40" cylindrical scattering chamber with domed lid and bottom. The chamber had 9" diameter ports at 0°, 90°, 180°, and 270°. The beam entered through the open 180° port and exited through the open 0° port. The 90° port had a Lexan plate with high-vacuum electronic feed-throughs, while the 270° port had a clear Lucite window. In addition, there were 5" ports at 135° and 315°. The 135° port had a clear Lucite window. The 315° port had a Lexan cover with feed-throughs for cooling for the detectors in the chamber with alcohol. The target ladder had vertical positions for 4 targets, and also could be rotated from outside the chamber. The beam passed through the target and the current was measured in a shielded Faraday cup, roughly 10 feet from the target.

The target was oriented with its normal at either 25° or 45° with respect to the beam. Charged particles (Z>2) were detected in four silicon ΔE-E telescopes each with a 300 mm² area. (Of course, these detectors were also sensitive to fragments with charge 1 or 2, but these events were rejected electronically, as described later). The silicon detectors were located inside the scattering chamber with azimuthal angles (with respect to the beam direction), θ, of 50°, 70°, and -90° in a horizontal plane (polar angle $\phi=0$), and the fourth detector was located at $\theta=50°$, $\phi=90°$ (below the beam axis in a vertical plane with the beam). The detectors were in aluminum mounts, which had provisions for liquid cooling. Refrigerated alcohol was run through channels in the mounts to keep the temperature at approximately -30° C throughout the experiment. The two telescopes at 50° had ΔE detectors 100 μm thick, while the other two telescopes had ΔE detectors 50 μm thick. The E detector of each telescope was 1000 μm thick. The front of each telescope was covered with a gold foil 3 mg/cm² thick to reduce the number of heavy reaction products hitting the ΔE detector. Rare-earth magnets were fastened to the detector mounts above and below the ΔE detector to deflect electrons. Each of the four telescopes was placed approximately 17.6 cm from the target. The solid angles of these detectors were determined by placing a 1.5 μCi ^{241}Am source in the target ladder. The ΔE elements of the telescopes were found to have solid angles of about 9.6 msr. For the data runs the E element of the telescopes limited the solid angle. These were approximately 0.7 cm behind the ΔE elements, which gives a telescope solid angle of 8.9 msr. With the use of these cooled detector telescopes, isotopically-resolved inclusive energy spectra were obtained for fragments which were identified as ^{6}Li, ^{7}Li, ^{8}Li, ^{7}Be, ^{9}Be, ^{10}Be, ^{10}B and ^{11}B.

Neutrons were detected in coincidence with the fragments listed above in any of ten liquid scintillators. The scintillators were approximately 1 liter of NE213 in a sealed glass cell approximately 12.7 cm in diameter and 7.6 cm thick. These were located in the horizontal plane at angles of 20°, 50°, 70°, 120°, 160°, -30°, -70°, -90°, -110°, and -140° with respect to the beam. A schematic diagram of the detector positions is given in Figure II.1.1. The front of each of these detectors was located 125 cm from the target, with the exception of the 20° neutron detector, which was 200 cm from the target. The typical neutron detector had a geometric solid angle of approximately 7.5 msr. Table II.1.1 gives a complete list of the physical parameters of the neutron detectors. Immediately in front of each neutron detector was a plastic paddle (NE102A) 0.6 cm thick that was used to electronically veto events where charged particles struck the neutron detectors.

The in-beam background of scattered neutrons was measured by taking data with shadow bars between the neutron detectors and the target. The shadow bars were conical sections of brass, with the same solid angle as the neutron detectors and a length equal to half the flight path.

II.2 Electronics

Figure II.2.1 shows a schematic diagram outlining the basic electronic modules used for the particle telescopes and the neutron detectors. The pulse height of the silicon detector signals was

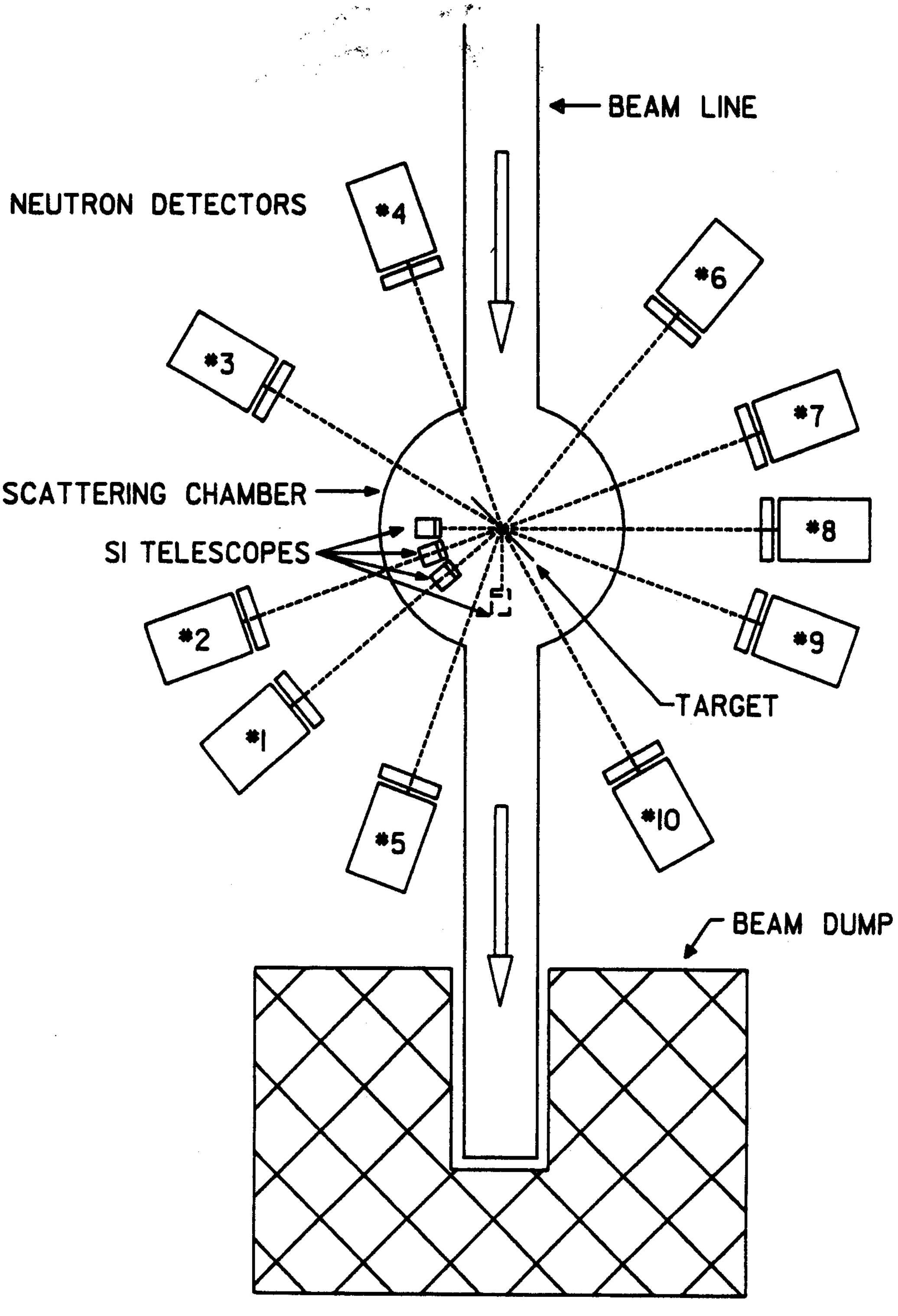

Figure II.1.1 Schematic of experimental set-up

TABLE II.1.1 Physical characteristics of the neutron detectors. (All dimensions given in cm).

Det. No.	Depth	Radius	Distance	$\Delta\Omega$ (msr)	Θ (Lab)
1	7.0	6.24	131	7.15	50°
2	7.5	6.35	130	7.49	70°
3	7.5	6.35	130	7.49	120°
4	7.6	6.35	129	7.59	160°
5	7.0	6.24	206	2.89	20°
6	7.5	6.35	130	7.49	-140°
7	7.5	6.24	131	7.13	-110°
8	5.7	5.56	129	5.82	- 90°
9	7.6	6.35	129	7.59	- 70°
10	7.0	6.24	131	7.15	- 30°

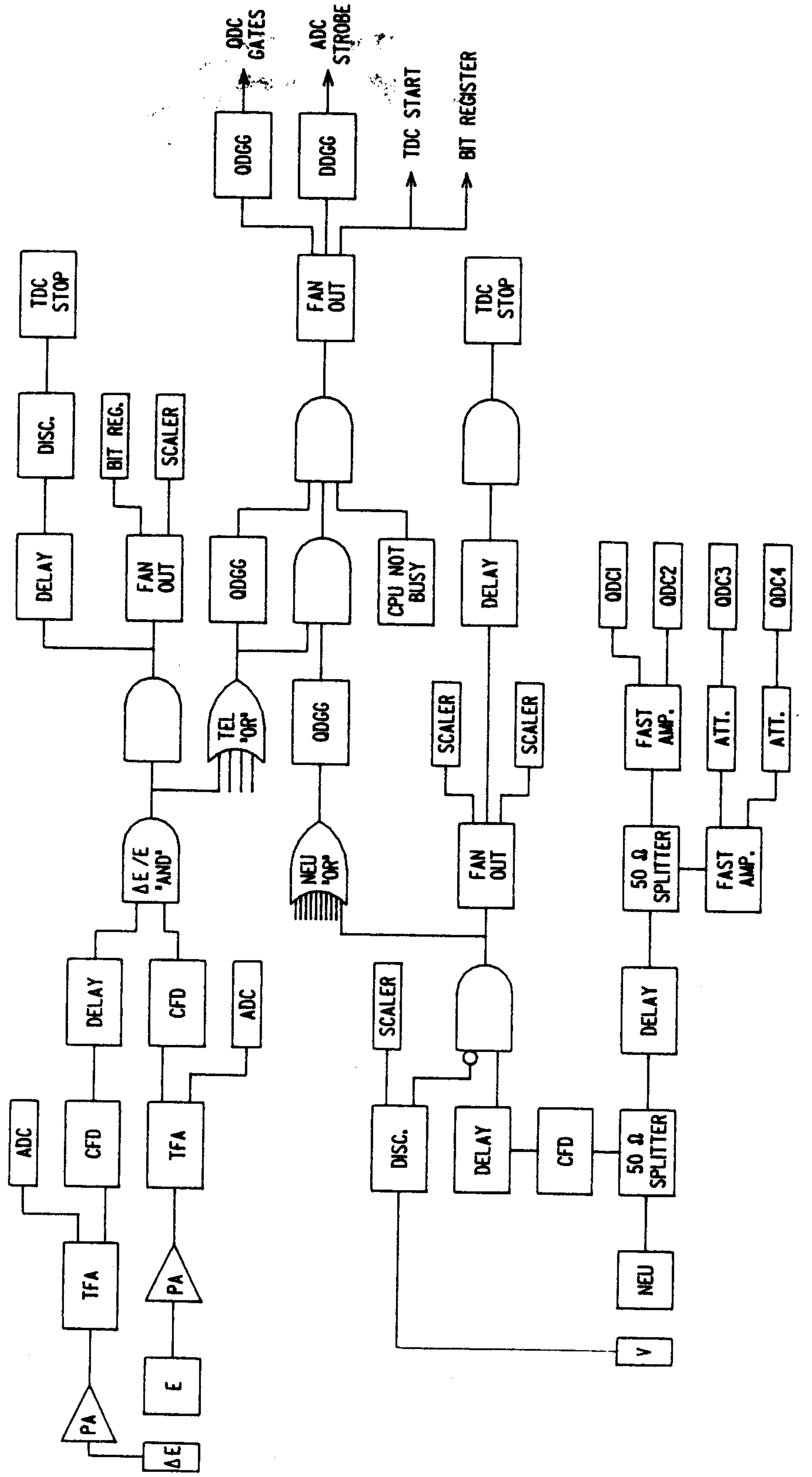

Figure II.2.1 Electronics schematic

digitized in analog-to-digital converters (12 bit Ortec AD811 ADC's). The area of the neutron detector signals (proportional to the charge) was digitized in charge-to-digital converters (LeCroy 2249W QDC's). The area of the first 30 ns of the neutron detector signal (charge collected in the first 30 ns) was also digitized to give pulse shape information to be used in discriminating between neutrons and γ rays. In addition, an amplified version of each of these latter two signals was also digitized to give additional resolution for small signals. Finally, the time information for all detectors that produced signals above threshold in a 500 ns window was digitized by time-to-digital converters (LeCroy 2228A TDC's).

For the data aquisition, there were 14 detectors: 4 ΔE-E telescopes and 10 neutron detectors. A valid telescope event required a coincidence between both silicon elements. A valid neutron event required a coincidence between a signal in a neutron detector and no signal in the plastic paddle in front of the same detector. In this way the 28 detector elements were reduce to 14 detectors. A bit register was set to record all the detectors in a valid event. Thus, for each event there was a sixteen-bit bit register, a ΔE pulse height, an E pulse height and a telescope time for each telescope that fired, a charge, a delta-charge, an amplified charge, an amplified delta-charge, and a neutron time for each neutron detector that fired. The data was read from the CAMAC by a system which employed a Motorola 68000 [Va85]. In conjunction with this, an LSI microprocessor read data rates (both raw and live) from scalers, including an integrated beam current signal. These two microprocessors filled buffers (data and scaler, respectively), and then sent them to a VAX 750. In addition to reading the data buffers from the CAMAC modules, the 68000 based system was programmed to discriminate against $Z \leq 2$ fragments in any of the telescopes and reject those events on-line. This was done primarily to reduce the amount of subsequent data analysis. Once the buffers were received by the VAX, they were written to tape at 6250 bpi and sampled on-line via the program SARA [Sh85]. The electronics was operated in one of three different modes: particle singles, particle-neutron coincidences, and neutron singles. Selection of the mode was done by pushing the appropriate buttons on a coincidence module.

In particle singles mode, only the silicon telescopes were necessary to trigger an event. The silicon detectors were biased at the voltages recommended by Ortec. The signal from each silicon detector went through an LBL pulser/preamplifier to a Tenelec 241S amplifier. The shaped output went to an Ortec AD811 ADC (12 bit). The fast output went to a constant fraction discriminator. This produced a relatively pulse-height independent timing NIM pulse. The width of this pulse was 50 ns for the ΔE detectors and 200 ns for the E detectors. The ΔE signal was delayed 30 ns relative to the E signal, as determined with the pulsers. For a given telescope, these two signals were sent to a coincidence module. A coincidence between both telescopes implies a good telescope event, and resulted in a 50 ns wide NIM signal fixed in time relative to the arrival of particles in the ΔE element of the telescope. An OR of the four telescopes was put into an AND coincidence unit with the computer not busy signal. The output of this coincidence unit was the master gate for particle singles.

Neutron/Y-ray identification in the liquid scintillators was done via a two-QDC method. This consisted of comparing the anode signal from the photomultiplier integrated over two different time periods. The different pulse shape produced by γ rays (compared to neutrons) allowed us to discriminate against γ-rays in our analysis. The neutron kinetic energy was determined by measuring the time of flight, relative to the pulse produced by the coincident intermediate mass fragment.

CHAPTER III: DATA ANALYSIS

3.1 Calibration

The energy calibration of the silicon detectors was determined with calibrated pulsers. Pulses in 5 MeV increments for the ΔE detectors (10 MeV increments for the E detectors) were recorded several times throughout the experiment. A linear fit between the known signal (read off the pulser dial) and the observed pulse height determined the calibration. The fit was very good, and changed negligibly over the duration of the experiment (recall that the detectors were cold; the width of the signal increased as a result of radiation damage to the detectors). A check of the calibration of the pulsers was made by comparing the energy range for a given isotope to what is expected based on the detector thicknesses and the stopping ranges given in Ziegler [Zi80]. In no case was any error discernable.

Before discussing the calibration of the TDC's, it is necessary to understand what their value represents, and in fact it will be convenient to replace the measured parameter with a related pseudoparameter. The relatively poorly defined time structure of the K500 cyclotron beam prevented timing against the rf signal. For this reason, meaningful time information was only obtained for coincidence events: when two detectors fired, the time of one would determine the time of the master gate. Then that detector's TDC would provide no new information. The time information would all be in the second detector's TDC. That TDC was started by the master gate and stopped by the second detector (actually a delayed signal from that detector). The only coincident events considered in this experiment were fragment-neutron coincidences. In that mode, the neutron signal time determined the master gate time, so the neutron TDC contained no useful information (at least for single neutron coincidences). The telescope's TDC would be started by the master gate (neutron time plus a constant) and stopped by a delayed telescope signal (fragment time plus a constant). Thus the neutron TDC value minus the fragment TDC value gives the difference between the neutron time of flight and the fragment time of flight within a constant. For any given event, the fragment time of flight independently can be calculated from the particle identification, fragment energy, and target-to-ΔE-detector distance. The constant can be determined by looking at γ-ray events as their time of flight is well known. Then the neutron time of flight is given by the neutron TDC value minus the fragment TDC value plus the fragment time of flight minus the constant. This value is a pseudo-parameter that will be used in place of the TDC parameter. Then, to determine the neutron time of flight in any event, we must have the neutron TDC value, the telescope TDC value, and the _fragment mass and energy_. In this way, the TDC histograms can be replaced by neutron time of flight histograms, which are more readily understood. The raw TDC histogram for any telescope is difficult to interpret since time runs from right to left, and the TDC start comes from the master gate, which can be determined by any one of ten neutron detectors, all of which have slightly different time characteristics. Conversely, the time-of-flight pseudo parameter for a given neutron detector in coincidence with fragments in any given telescope shows time running from left to right.

The TDC's were calibrated by comparing the periodicity of the time-of-flight histogram to the period of the cyclotron. The time-of-flight histogram gated on γ rays (eliminating the neutron signals by pulse shape discrimination) for each neutron detector in coincidence with a signal from any particle telescope showed six γ-ray peaks for the E/A=35 MeV data and five for the E/A=20 MeV data. Figure III.1.1 shows the time-of-flight histogram for γ rays in neutron detector-1 in coincidence with ^{7}Li fragments for the E/A=20 MeV data. The periodic structure is due to the cyclotron periodicity, and the large peak is due to real coincidences (the γ ray and coincident fragment from the same beam pulse) and the others to accidental coincidences (the γ ray and coincident fragment from different beam pulses). The centroids of these peaks were measured for each case. The average number of channels between peaks for each TDC was set equal to the cyclotron period (which is known to 5 significant figures) to obtain the number of seconds/division for that TDC. In no case did the discrepancy of the observed period exceed the width of the gamma peak. The TDC calibration was 0.227 ns/channel.

The electron equivalent energy of the neutron detector pulse heights was calibrated using three different γ sources: ^{22}Na, ^{60}Co, and ^{212}Pb. The neutron detectors are sensitive to the Compton electrons produced by the γ rays from these sources. The pulse height distribution of each source showed a step function at the Compton edge. The Compton edge for the observed γ rays was defined to be at half the maximum value of the step function. The γ rays observed were: 0.511 MeV

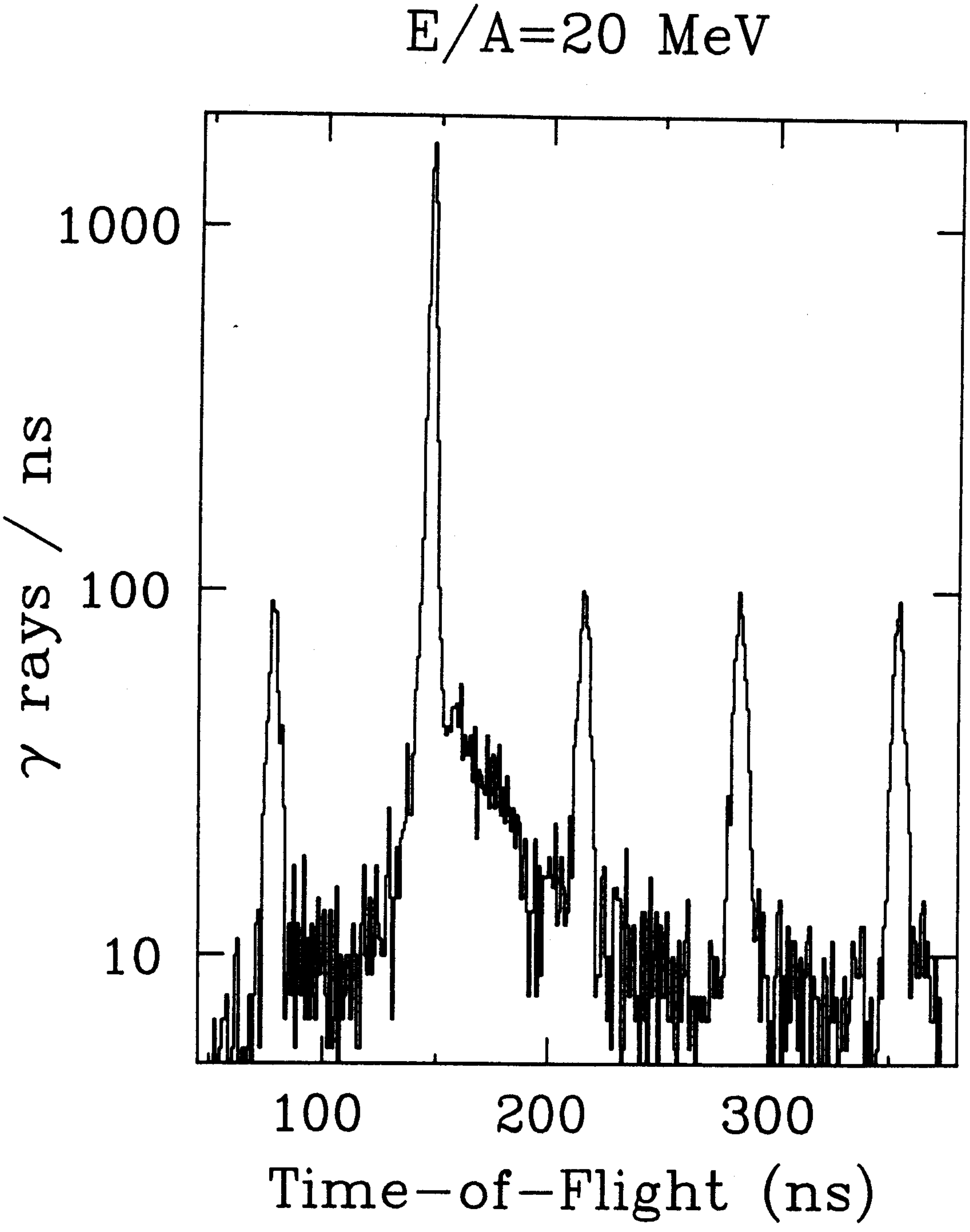

Figure III.1.1 Time-of-flight spectrum for γ rays in neutron detector-1 in coincidence with ^{7}Li fragments in any telescope, E/A=20 MeV.

and 1.27 MeV from the ^{22}Na, 1.25 MeV (average of the 1.17 and 1.33 MeV γ rays) from ^{60}Co, and 2.62 MeV from the ^{212}Pb. For Compton scattering, the scattered wavelength, λ', is related to the original wavelength, λ, by:

$$\lambda' - \lambda = \frac{h}{mc}(1-\cos\theta), \qquad (III.1)$$

where h/mc is 2π times the electron Compton wavelength and θ is the scattering angle of the γ ray. For $\theta=\pi$, this gives the scattered energy in terms of the original energy, E, as:

$$E' = \frac{0.511\times E}{2\times E+0.511}. \qquad (III.2)$$

A linear fit between the Compton edge channel number and these scattered energies calculated from the original energies and equation III.2 gave the calibration of the pulse height in electron equivalent energy. This information was used to determine the lower cutoff of the pulse height in electron equivalent energy, a necessary input to determine the neutron detector efficiency.

The neutron detector efficiency was determined by the code TOTEFF [Ku64]. In Ref. Re86, TOTEFF was compared to a Monte Carlo code developed by Cecil et al. [Ce79]. Based on that comparison, the uncertainty in the absolutely neutron detector efficiency is approximately 10%. Figure III.1.2 shows a typical neutron detector efficiency as a function of neutron kinetic energy.

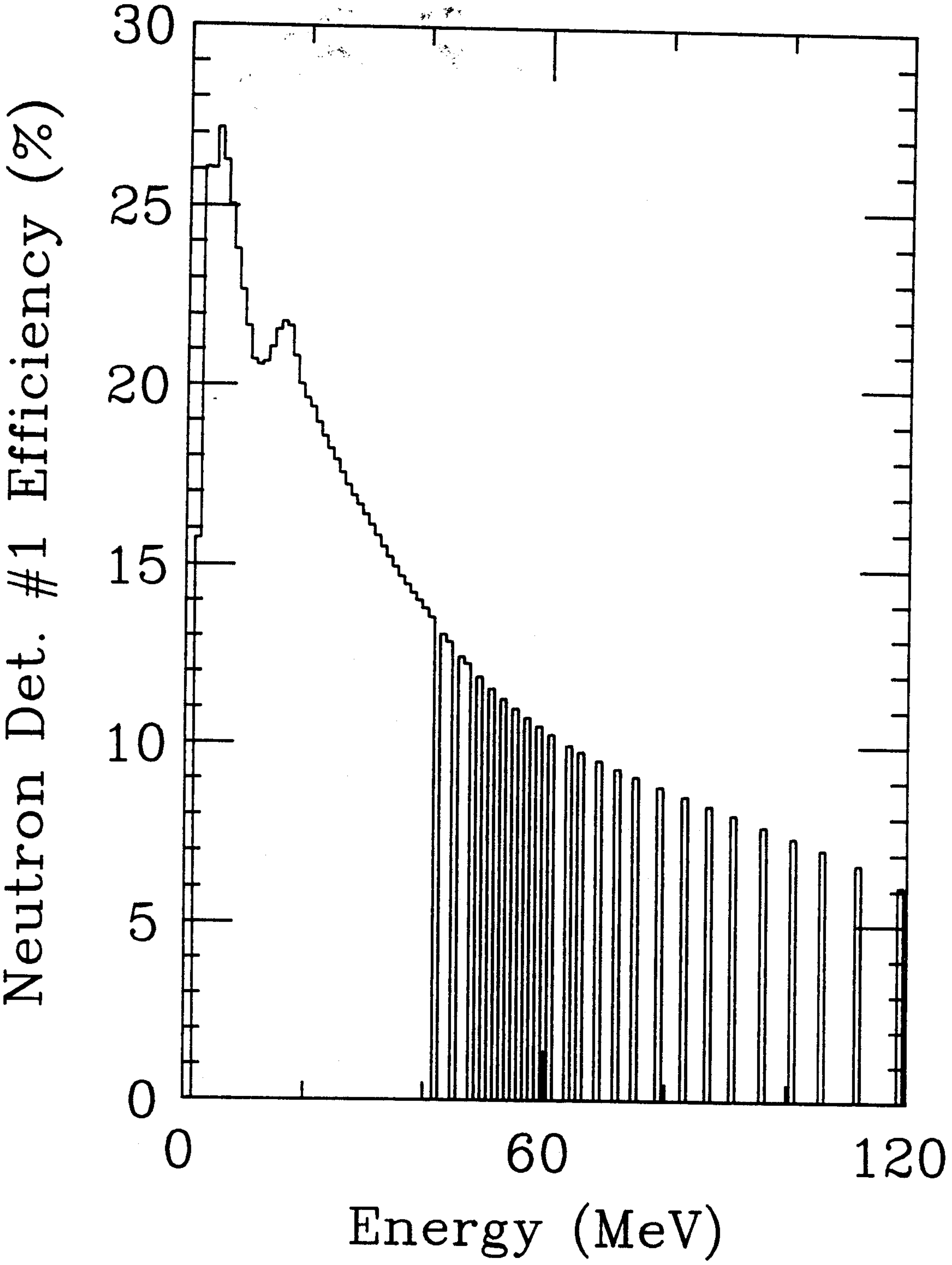

Figure III.1.2 Neutron detector efficiency as a function of neutron kinetic energy.

III.2 Single Particle Inclusive Data

Charged particle inclusive data were taken with the neutron coincidence requirement removed from the master gate. This was done for approximately one-half to one hour every four to eight hours throughout the duration of the experiment. All of these runs were binned into a single ΔE vs. E (the signal from the front silicon detector vs. the signal from the back silicon detector) histogram for each telescope. Figure III.2.1 shows the ΔE-E histogram for telescope-4. Particle identification gates were drawn for each of the following isotopes: ^{6}Li, ^{7}Li, ^{8}Li, ^{7}Be, ^{9}Be, ^{10}Be, ^{10}B, and ^{11}B. The same singles runs were then binned into kinetic energy spectra for each isotope in each telescope. Typical spectra are shown for the E/A=35 MeV data in Figure III.2.2 and for the E/A=20 MeV data in Figure III.2.3. The solid lines shown in these two figures represent the moving source analysis described next.

For each isotope identified, the kinetic energy spectra were fit by a moving source model [Ja83]. A single parameter set of normalization, slope parameter (kT in the temperature interpretation) and source velocity was obtained for all spectra of a given isotope. A Coulomb shift [We78] was employed, where the shift was a fraction of the Coulomb barrier between the observed fragment and the residual nucleus, transformed from center of mass to lab coordinates. The fit parameters (including the Coulomb shifts used) are given in Table III.2.1 for the E/A=35 MeV data and in Table III.2.2 for the E/A=20 MeV data.

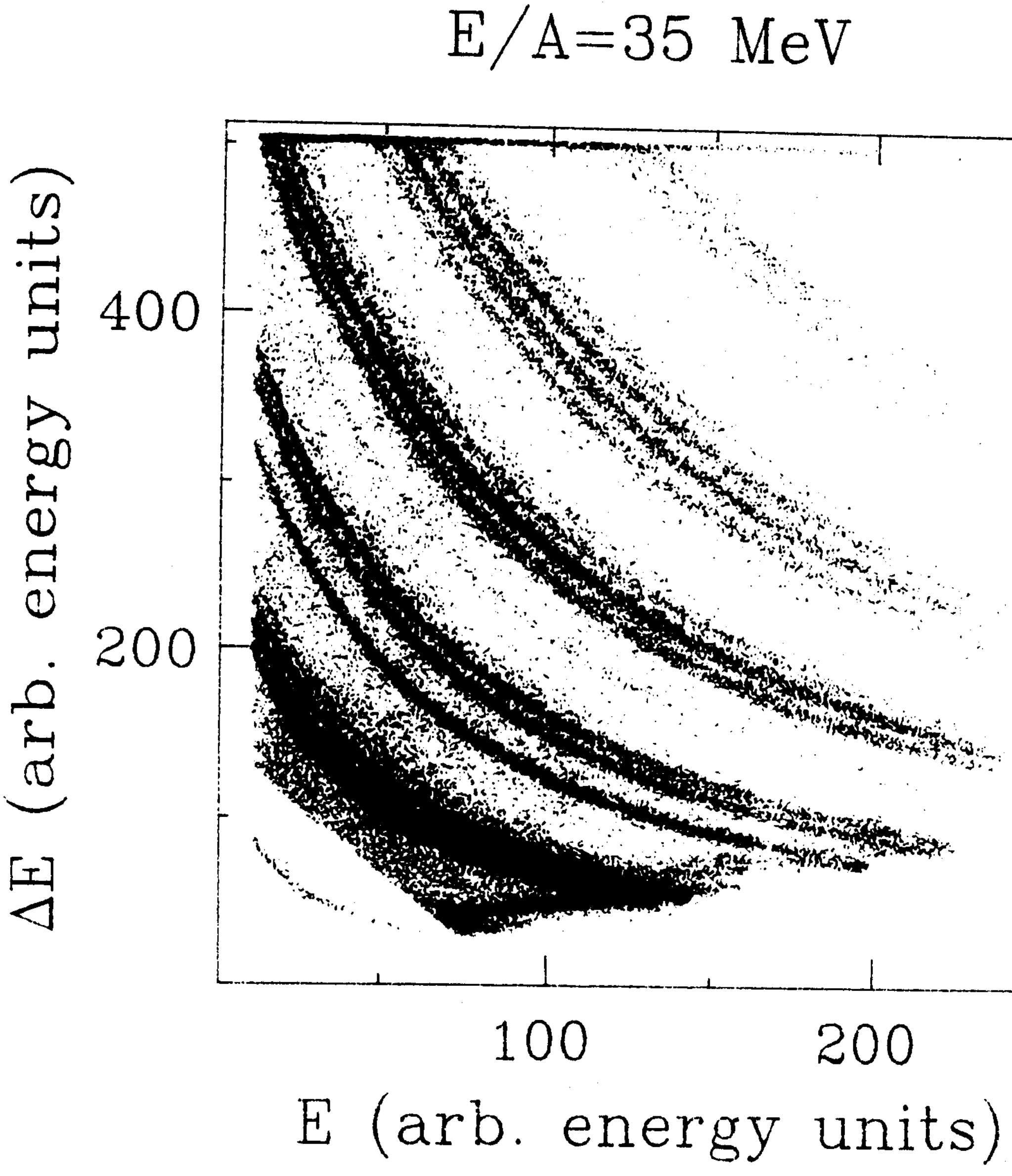

Figure III.2.1 ΔE vs. E particle identification map for telescope 4, E/A=35 MeV.

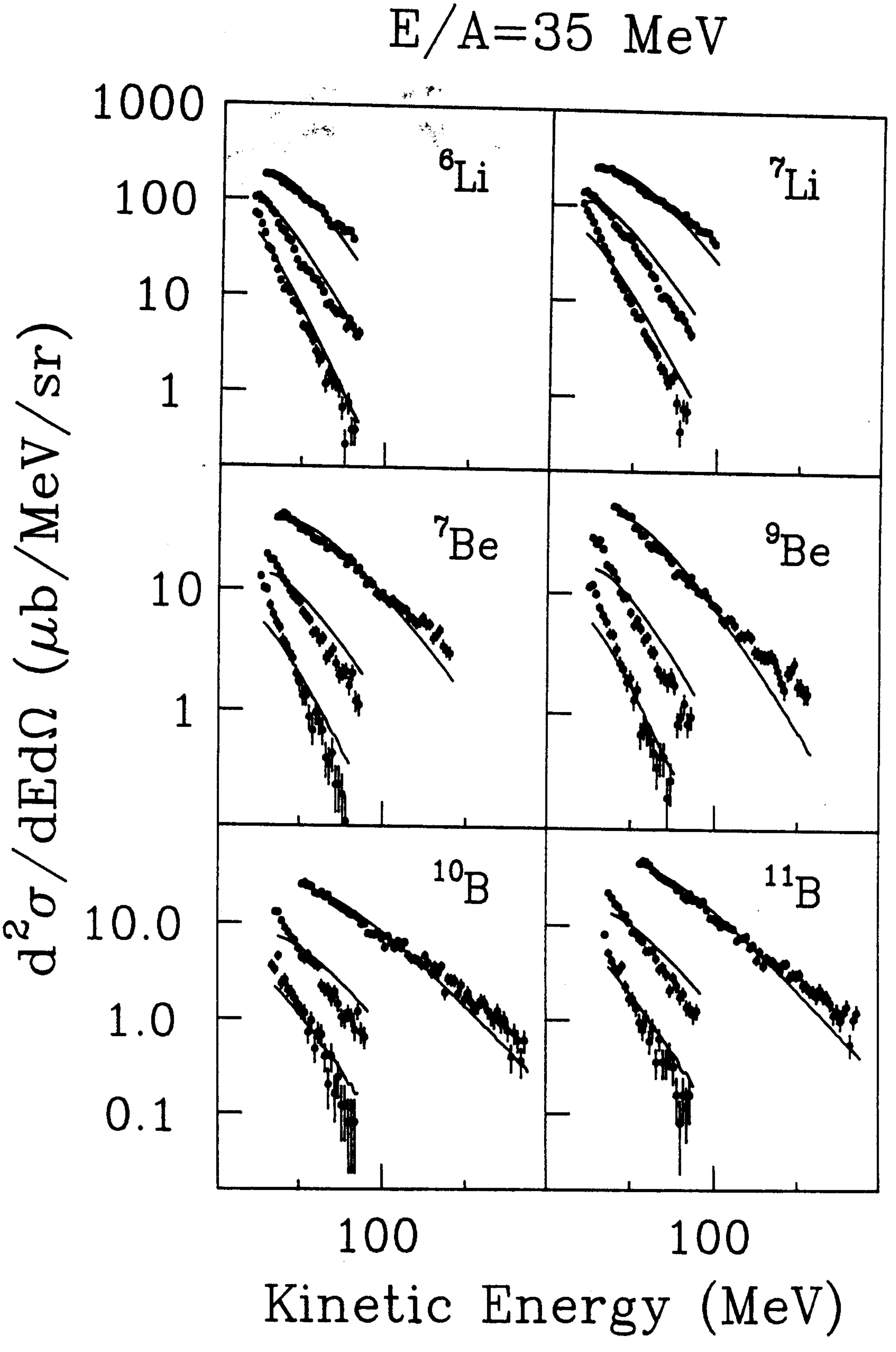

Figure III.2.2 Fragment kinetic energy singles spectra with moving source fit, E/A=35 MeV.

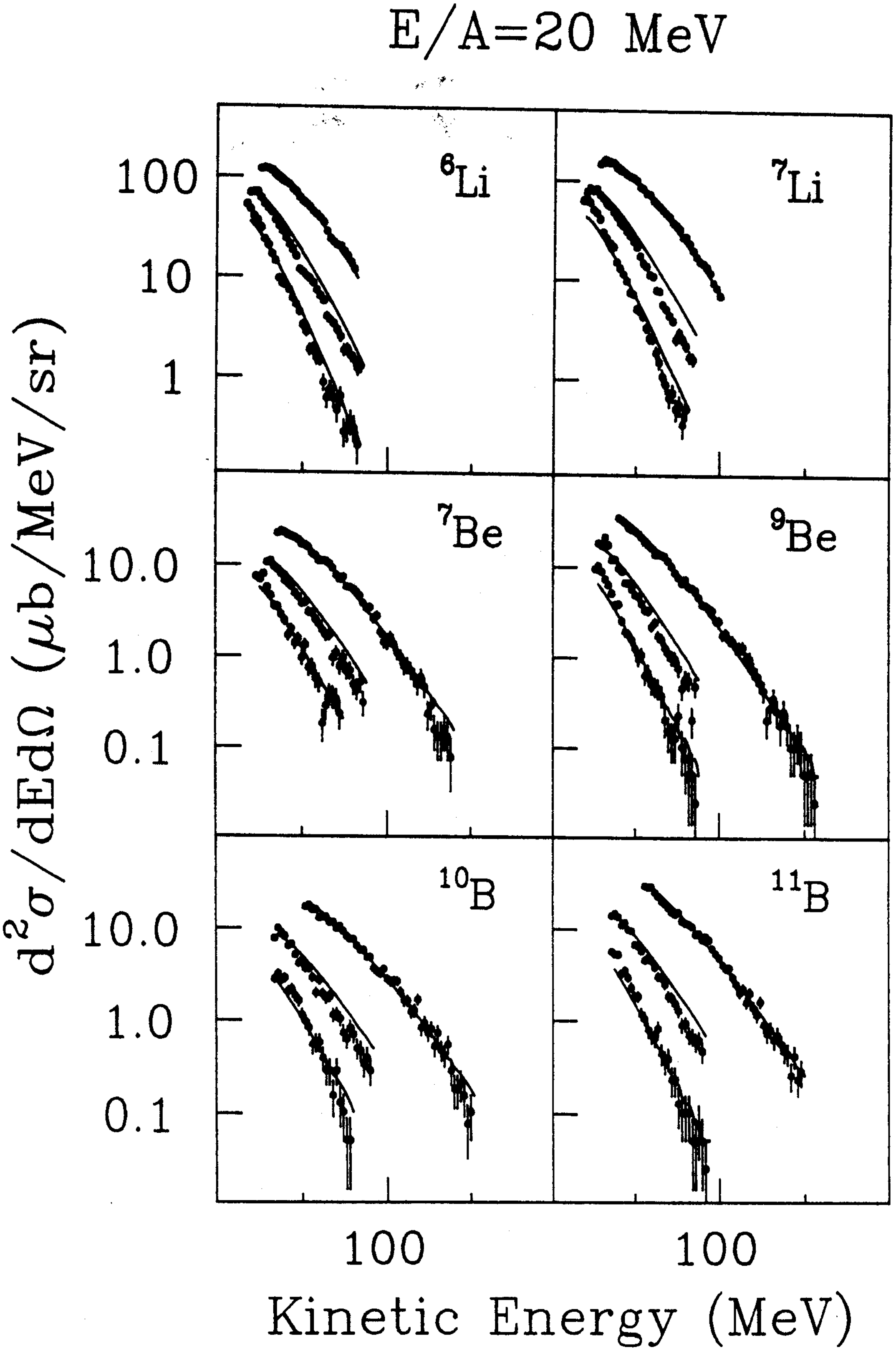

Figure III.2.3 Fragment kinetic energy singles spectra with moving source fit, E/A=20 MeV.

TABLE III.2.1 Fragment kinetic energy moving source fit parameters.

Isotope	Coulomb Shift (MeV)	E/A=35 MeV σ (mb)	T (MeV)	β	χ^2/dof	#dof
^{6}Li	10	54.8(1)	11.2(5)	0.075(2)	40.9	84
^{7}Li	10	92.4(2)	12.8(3)	0.081(1)	79.2	94
^{8}Li	10	12.9(1)	14.5(5)	0.070(4)	10.9	101
^{7}Be	13	18.0(1)	15.0(3)	0.098(3)	11.6	107
^{9}Be	13	20.5(1)	13.0(4)	0.083(2)	13.0	108
^{10}Be	13	13.2(1)	13.7(7)	0.082(1)	6.1	108
^{10}B	16	14.8(1)	15.0(4)	0.092(5)	6.8	119
^{11}B	16	28.1(1)	14.2(4)	0.086(4)	8.5	110

TABLE III.2.2 Fragment kinetic energy moving source fit parameters.

Isotope	Coulomb Shift (MeV)	E/A=20 MeV σ (mb)	T (MeV)	β	χ^2/dof	#dof
^{6}Li	10	32.5(1)	10.3(3)	0.067(3)	20.6	92
^{7}Li	10	49.8(1)	11.3(4)	0.068(2)	42.5	99
^{8}Li	10	6.1(1)	13.3(5)	0.058(1)	6.8	99
^{7}Be	13	8.0(1)	11.5(3)	0.072(3)	4.0	103
^{9}Be	13	12.4(1)	10.8(4)	0.066(1)	6.3	113
^{10}Be	13	6.9(1)	11.6(7)	0.067(1)	3.6	108
^{10}B	16	9.2(1)	11.6(3)	0.071(3)	3.9	99
^{11}B	16	18.0(1)	11.0(4)	0.069(1)	3.5	110

III.3 Coincident Neutron Data

III.3.1 Neutron/γ-ray Discrimination

Neutrons were distinguished from γ rays by pulse shape discrimination above a threshold of approximately 200 keV electron equivalent energy, independent of the time of flight. The pulse shape discrimination was done with a 2-QDC method. The signal from the anode of the neutron detector photomultiplier was split and fed into two QDC's. Each QDC began integrating at the same point in time, but one (QDC2) integrated the total charge (over approximately 300 ns) while the other (QDC1) only integrated the charge collected in approximately the first 30 ns. In Fig. III.3.1, QDC1 versus QDC2, two distinct groups can be seen. One group corresponds to γ rays, which deposit a greater fraction of their total energy in a short time than do neutrons, the other group. Software gates were set on the neutron groups for each neutron detector with thresholds near 200 keV electron equivalent energy. The gain on the neutron detector signals was set high to get maximum resolution at low energies, when the two groups (neutrons and γ rays) are close together. In order to retain the events that would otherwise end up in the overflow channel, attenuated versions of these signals where fed into a second pair of QDC's. The final neutron spectra are a combination of all events that could be identified as neutrons in either QDC map.

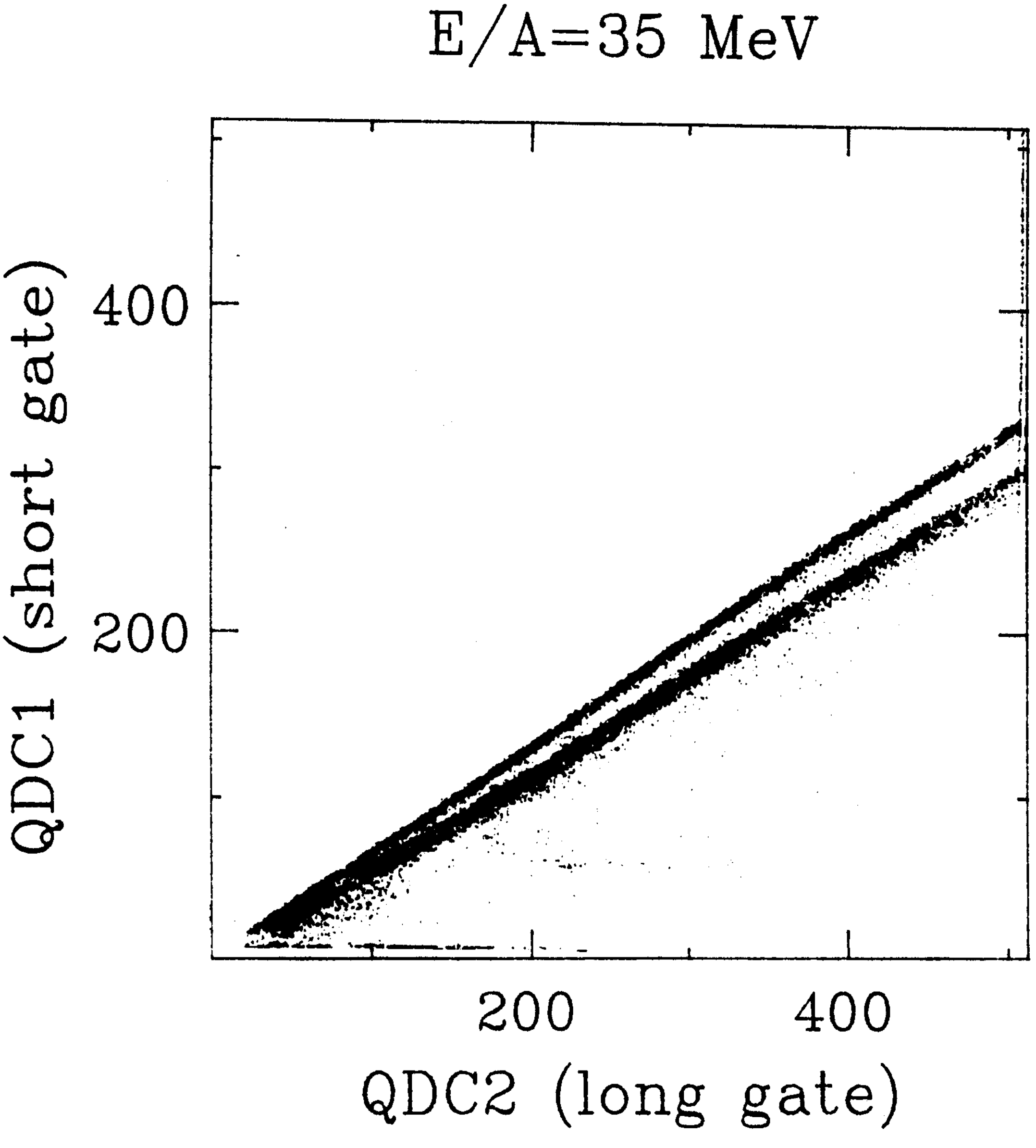

Figure III.3.1 QDC1 vs. QDC2 for neutron detector-8, E/A=35 MeV.

III.3.2 Neutron Time-of-flight

The neutron time-of-flight was measured relative to the charged particle signal from the front detectors of the telescopes. The time between the nuclear event and the silicon telescope signal was established from the distance from the target to the silicon detector, the particle mass, and the particle energy. Figure III.1.1 shows the total range of time information for events in the neutron detectors in coincidence with telescope events. This extends over nearly five cyclotron periods (for E/A=20 MeV) or about 340 ns. The true coincidences end before the end of two periods, so the first two periods (from 0 to 105 ns for E/A=35 MeV and from 0 to 138 ns for E/A=20 MeV) were considered the real plus the accidental coincidences. Figure III.3.2 shows this portion of the time-of-flight spectrum for neutrons in neutron detector-1 in coincidence with ^{7}Li fragments. This spectrum must be corrected for indirect neutron events by the subtraction of a scaled (by the ratio of the integrated beam currents) version of the same histogram for data runs with shadow bars in place (shown in dots in Figure III.3.2). The second two periods of the spectrum (from 105 to 209 ns for E/A=35 MeV and from 138 to 275 ns for E/A=20 MeV) were considered to be the accidental coincidences (shown in Figure III.3.3, with the dots representing the shadow bar data), and subtracted from the real plus accidental coincidences spectrum (after both were corrected for indirect neutrons by subtraction of the appropriate shadow bar histogram) to yield the true real coincidences (shown in Figure III.3.4). This technique was used throughout the analysis, for each type of neutron histogram.

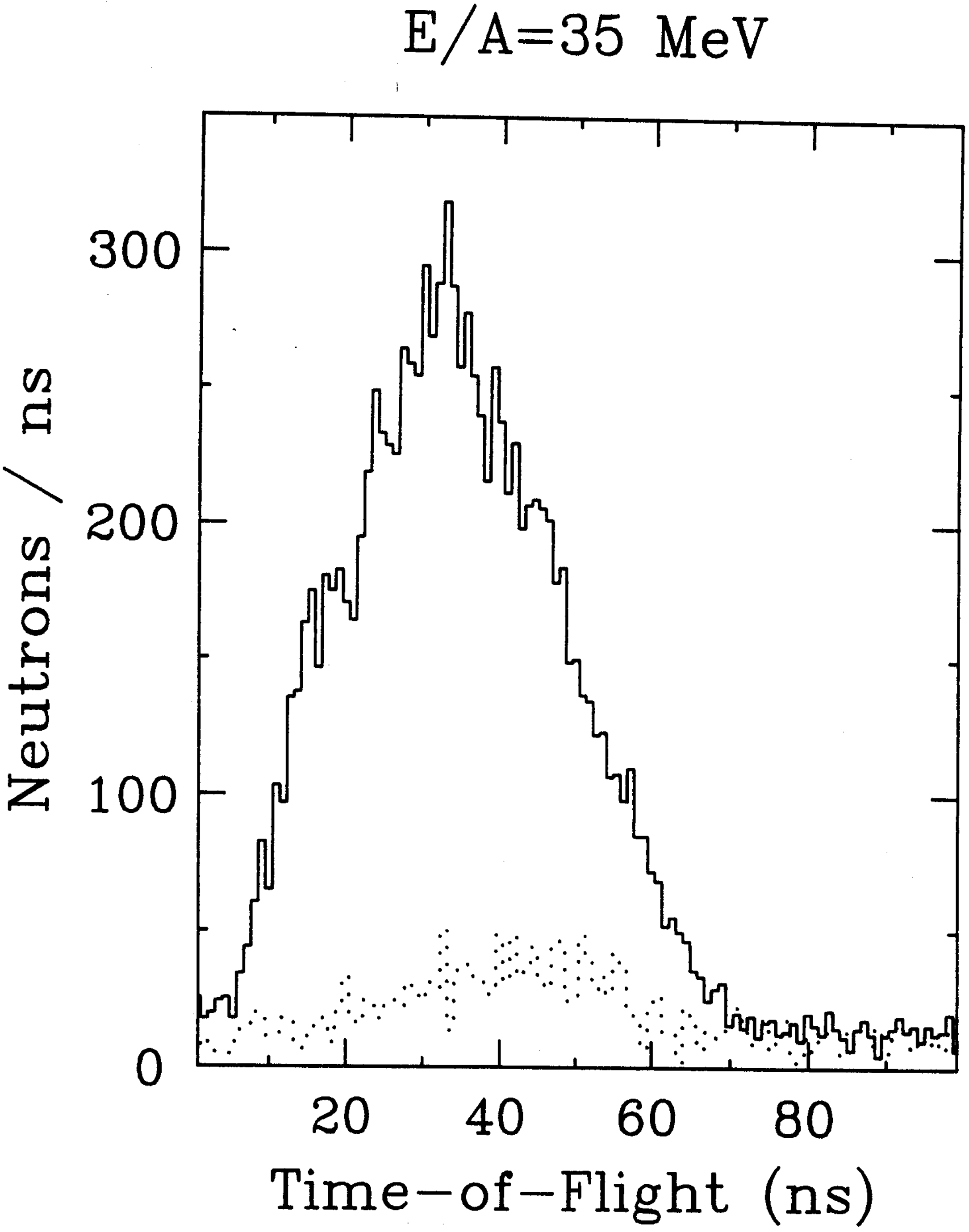

Figure III.3.2 Neutron real plus accidental time-of-flight histogram (solid) with corresponding shadow bar histogram (dots) for neutron detector-1, E/A=35 MeV.

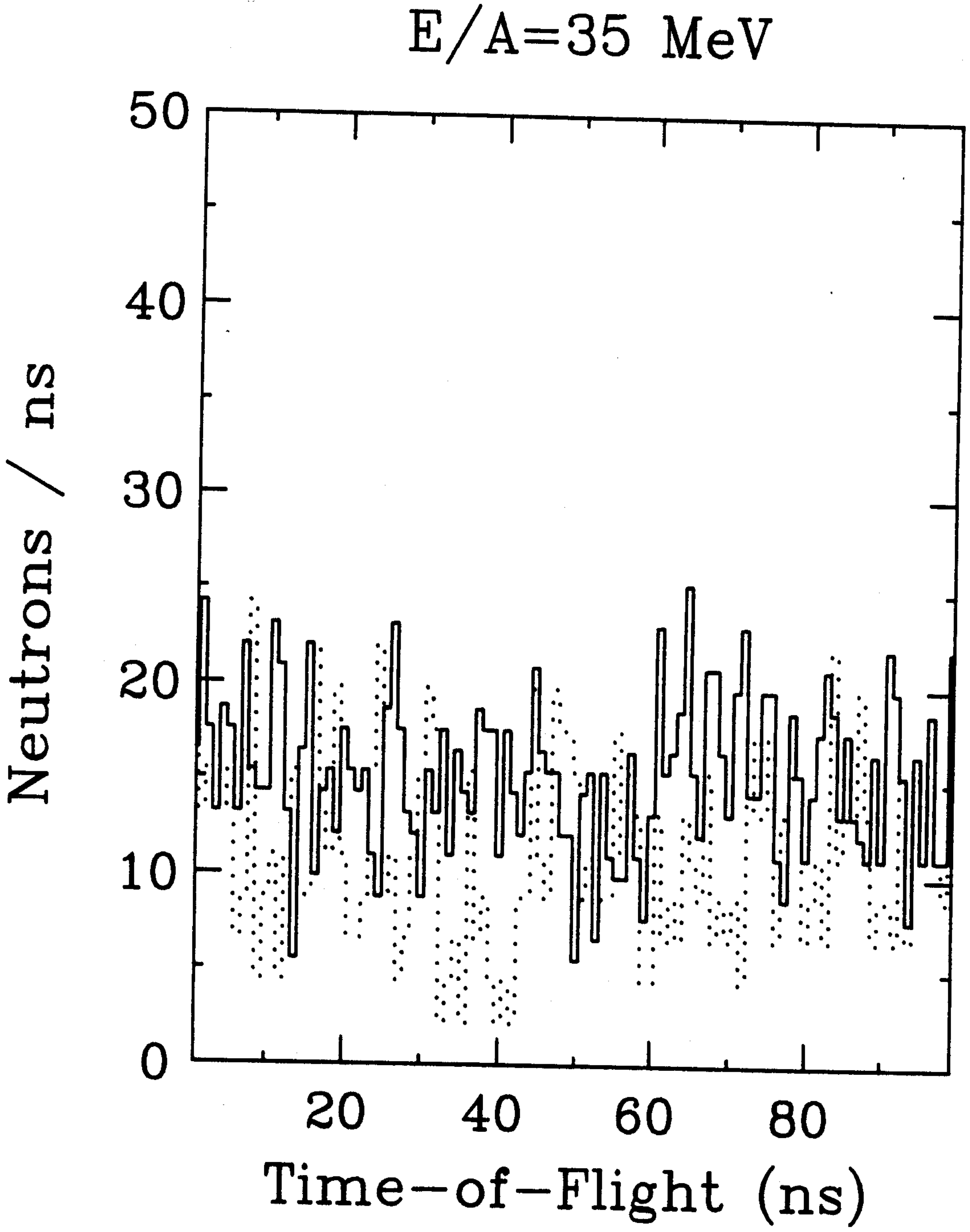

Figure III.3.3 Neutron accidental time-of-flight histogram (solid) with corresponding shadow bar histogram (dots) for neutron detector-1, E/A=35 MeV.

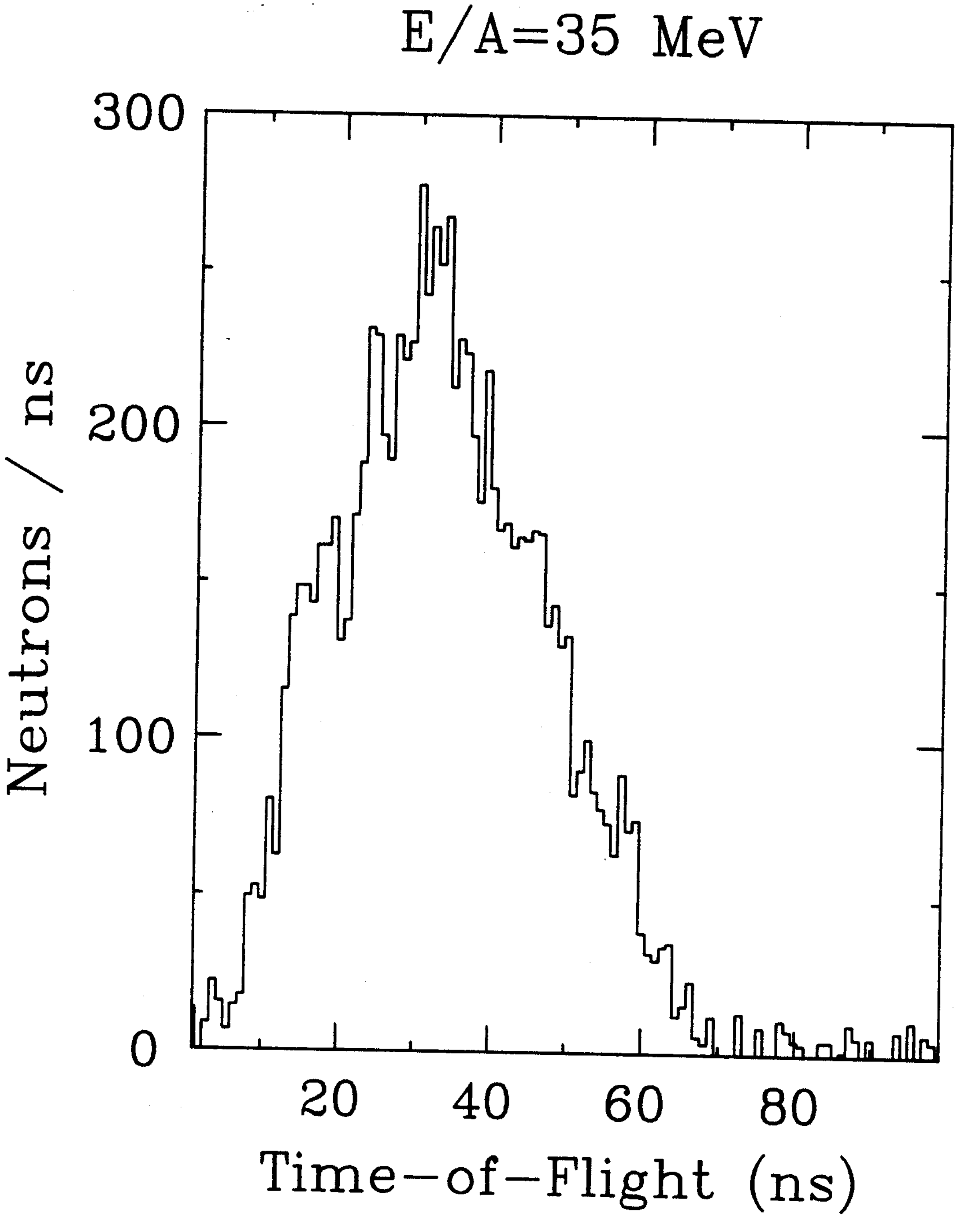

Figure III.3.4 Neutron real time-of-flight histogram for neutron detector-1, E/A=35 MeV.

III.3.3 Neutron Kinetic Energy

The distance from the target to each neutron detector was measured, and when combined with the neutron time-of-flight, allowed calculation of the neutron kinetic energy on an event-by-event basis. Figure III.3.5 shows a neutron kinetic energy spectrum (neutron detector-1 in coincidence with ^{7}Li in telescope-1) both before and after correction for the energy dependence of the neutron detector efficiency. The neutron detector efficiency as a function of energy was calculated with the code TOTEFF [Ku64] and folded into the neutron data. Figure III.3.6 shows all 10 neutron spectra with the neutron detector efficiency included. Similar kinetic energy spectra were generated for neutrons in coincidence with each charged particle, in each telescope, and for each neutron detector. These spectra were then fit with a two-source moving source model [Ja83]. The double differential multiplicity, $\frac{d^2M}{dEd\Omega}$, is given by:

$$\frac{d^2M}{dEd\Omega} = \sum_{i=1}^{2} \frac{M_i\sqrt{E}}{2\sqrt{(\pi kT_i)^3}} \exp[-(E-2\sqrt{\varepsilon_i E}\cos(\theta)+\varepsilon_i)/kT_i], \qquad \text{(III.3)}$$

where E is the neutron kinetic energy, θ is the neutron angle in the lab, M_i and kT_i are the associated neutron multiplicity and the slope parameter (temperature), respectively for each source, and ε_i is the kinetic energy per nucleon of the source, given by:

$$\varepsilon_i = 931.5 \times \left(\frac{1}{\sqrt{1-\beta_i^2}} -1\right), \qquad \text{(III.4)}$$

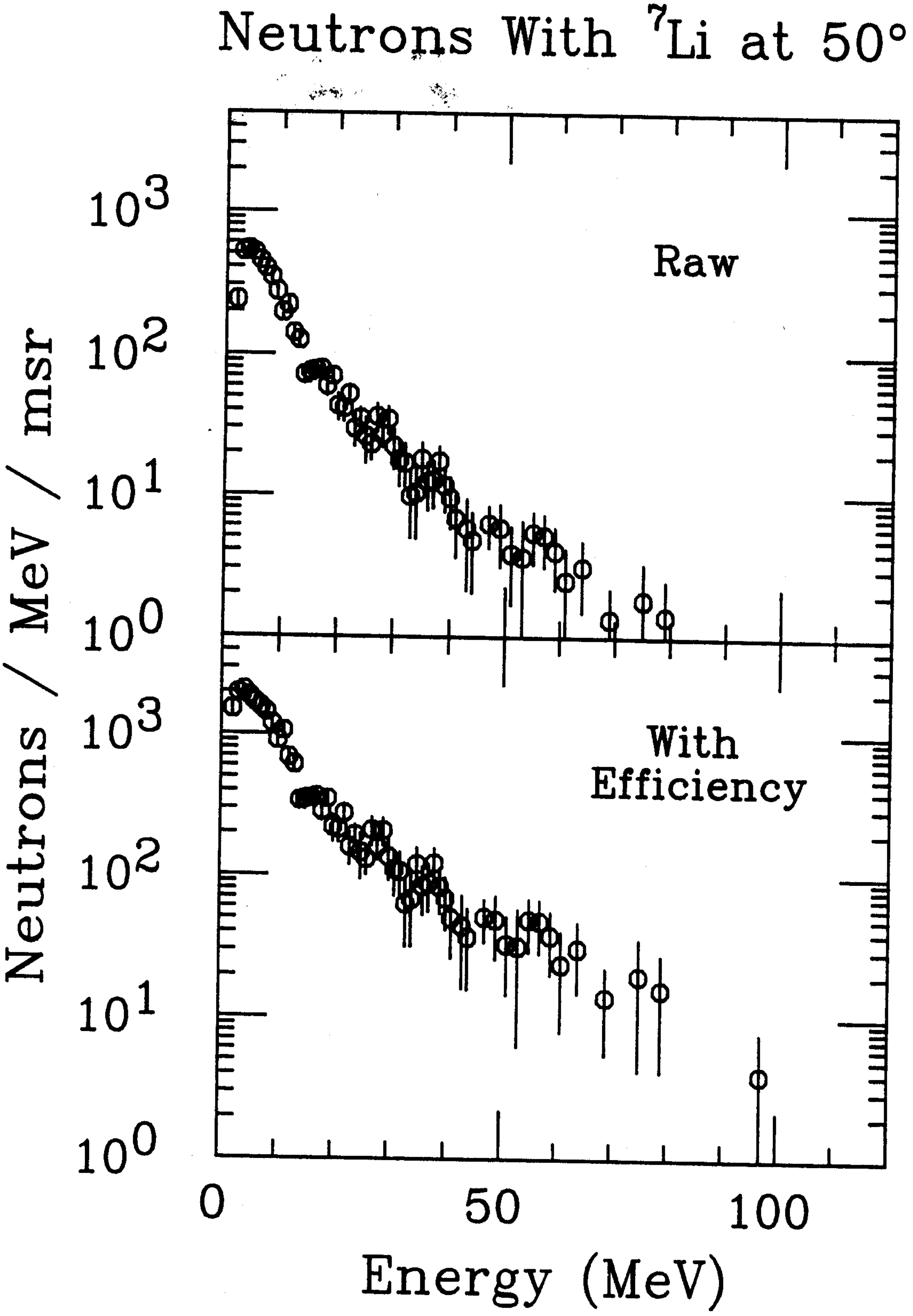

Figure III.3.5 Kinetic energy histogram for neutrons at 50° in coincidence with ^{7}Li at 50° before and after folding in the neutron detector efficiency.

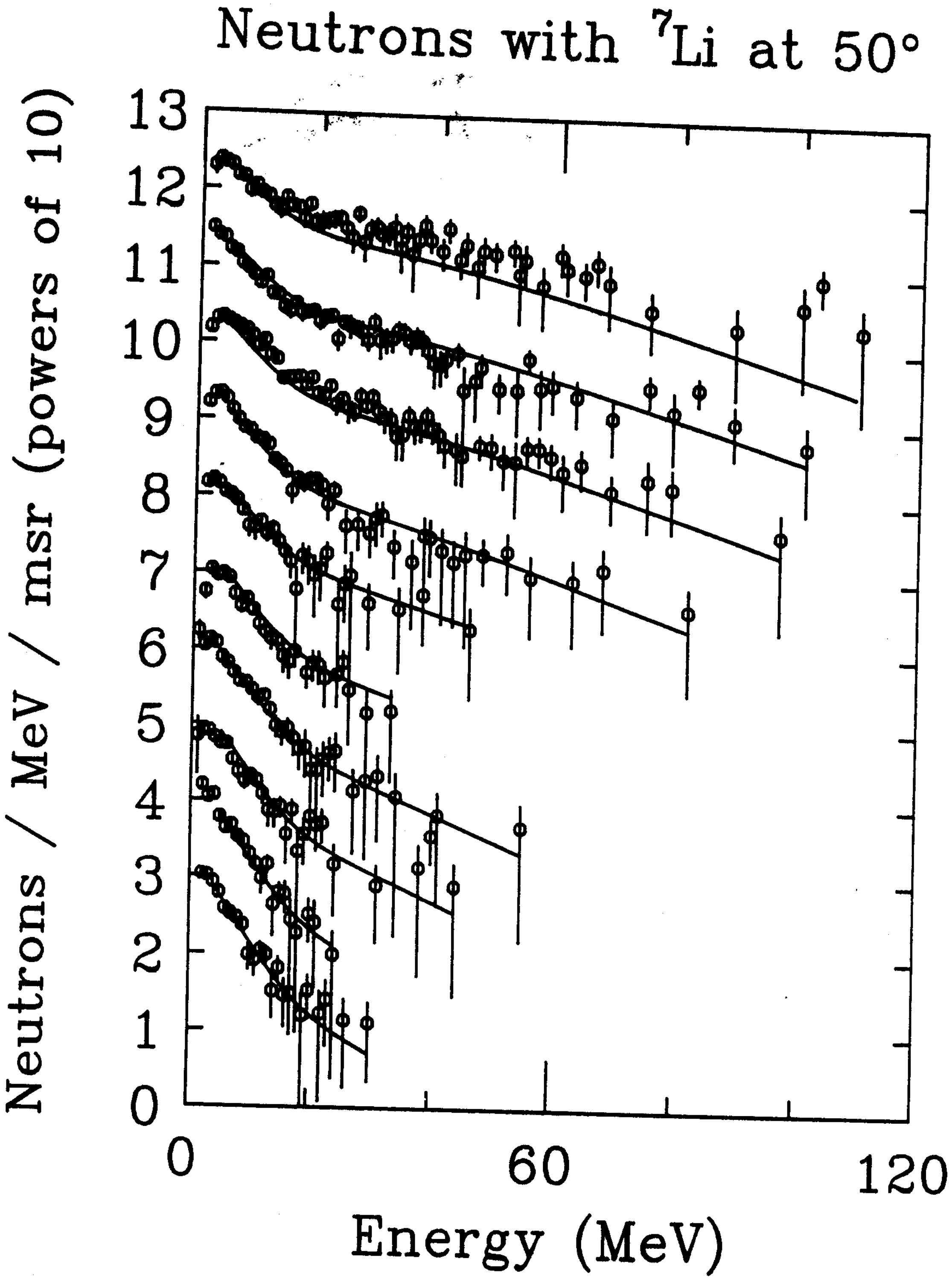

Figure III.3.6 Kinetic energy spectra for neutrons in coincidence with ^{7}Li at θ=50°, ϕ=0° (data points) with two-source moving source fit (solid lines). The order of the neutron detectors (from top to bottom) is: 20°, -30°, 50°, -70°, 70°, -90°, -110°, 120°, -140°, and 160° in the lab. The spectra are separated artificially by an order of magnitude each, with the 160° data at unit normalization.

where β_i is the source velocity for each source in units of c, the speed of light. The pre-factor of $\sqrt{E}$ in equation III.3 arises for two different reasons for the two different sources. For the slower source, the temperature parameter indicates a relatively low excitation energy per nucleon. This implies "surface emission" of the neutrons, which for single neutron emission corresponds to a pre-factor of E [Go78]. But the associated multiplicity indicates multiple neutron emission, which corresponds to a prefactor of $E^{5/11}$ [Le59]. This has been approximated by $\sqrt{E}$. In this case, kT is an effective temperature parameter. This is slightly less than the temperature of the daughter nucleus after the first neutron emission by a factor of 11/12 [Le59]. Throughout this thesis, only the effective temperature parameter is discussed. For the second source, the temperature parameters are much higher, and "volume emission" is assumed. In that case, the pre-factor is $\sqrt{E}$ [Go78].

The neutron kinetic energy spectra fit parameters (M_i, kT_i, and β_i;i=1,2) are shown in Table III.3.1 for the E/A=35 MeV data and in Table III.3.2 for the E/A=20 MeV data. The parameters are listed separately for neutrons in coincidence with each isotope observed (^{6}Li, ^{7}Li, ^{8}Li, ^{7}Be, ^{9}Be, ^{10}Be, ^{10}B, and ^{11}B) and for each position of silicon detector (θ=50°, 70°, 90°, φ=0°, and θ=50°, φ=90°). Generally, all 10 neutron detectors were included in each fit. The exceptions were for the θ=50°, 70°, φ=0° detectors when the coincident fragment was ^{6}Li, ^{7}Li, ^{9}Be, ^{10}Be, or ^{11}B. In those cases, the neutron detector that was colinear with the fragment detector was excluded from the fitted data. These cases were particularly sensitive to neutrons from the sequential decay of intermediate mass fragments in particle unbound states. The

TABLE III.3.1 Associated neutron kinetic energy moving source fit parameters.

E/A=35 MeV

		Source #1			Source #2				
IMF	Angle	M_1	T_1	β_1	M_2	T_2	β_2	χ^2/dof	#dof
^{6}Li	50°	6.32(7)	3.07(5)	0.021(6)	2.02(6)	12.7(5)	0.096(4)	1.269	249
^{6}Li	70°	6.54(11)	2.98(5)	0.022(2)	2.00(10)	14.0(9)	0.101(8)	0.932	194
^{6}Li	90°	6.19(16)	3.23(17)	0.020(3)	1.97(18)	16.1(10)	0.143(17)	0.762	135
^{6}Li	50°†	6.05(7)	2.72(4)	0.016(1)	1.46(5)	11.0(5)	0.092(5)	1.142	224
^{7}Li	50°	6.48(6)	3.07(3)	0.020(3)	1.88(3)	12.5(3)	0.099(3)	1.689	291
^{7}Li	70°	6.35(10)	2.91(6)	0.019(1)	1.97(8)	13.7(7)	0.103(6)	1.036	218
^{7}Li	90°	6.33(14)	3.0(3)	0.020(1)	2.48(17)	19.4(10)	0.105(15)	0.814	162
^{7}Li	50°†	5.55(5)	2.81(4)	0.015(1)	1.19(3)	9.7(9)	0.116(13)	1.463	260
^{8}Li	50°	6.43(15)	2.80(10)	0.022(9)	2.56(13)	12.0(10)	0.084(16)	0.848	171
^{8}Li	70°	5.7(3)	2.9(2)	0.023(4)	2.8(3)	12.8(10)	0.042(38)	0.654	89
^{8}Li	90°	5.8(4)	2.3(3)	0.024(5)	5.0(6)	13.8(10)	0.020(36)	0.547	61
^{8}Li	50°†	5.09(15)	2.91(10)	0.015(3)	1.43(15)	12.2(9)	0.090(11)	0.810	107
^{7}Be	50°	7.23(13)	3.02(8)	0.022(2)	2.12(11)	11.9(8)	0.101(9)	1.172	181
^{7}Be	70°	6.9(3)	2.57(15)	0.023(9)	4.3(4)	15.8(16)	0.05(6)	0.696	103
^{7}Be	90°	7.5(6)	2.5(4)	0.01(2)	9.2(4)	23(9)	0.24(10)	0.474	38
^{7}Be	50°†	6.17(14)	2.60(9)	0.015(2)	1.56(13)	13.5(10)	0.088(18)	0.747	135
^{9}Be	50°	6.76(12)	2.79(9)	0.021(3)	2.29(12)	12.5(7)	0.096(7)	1.012	149
^{9}Be	70°	6.7(3)	2.54(18)	0.019(3)	3.9(3)	19.2(10)	0.09(4)	0.543	81
^{9}Be	90°	7.6(10)	2.2(10)	0.01(5)	2.6(8)	6.0(16)	0.13(9)	0.318	29
^{9}Be	50°†	5.10(14)	2.81(12)	0.019(3)	1.47(14)	13.4(10)	0.101(17)	0.643	122
^{10}Be	50°	5.48(18)	2.88(16)	0.021(5)	2.7(2)	12.2(10)	0.076(12)	0.589	121
^{10}Be	70°	6.0(4)	2.0(4)	0.021(3)	4.6(5)	10.3(10)	0.07(3)	0.443	53
^{10}Be	90°	4.1(10)	3(7)	0.01(2)	6(9)	11(3)	0.1(7)	0.282	13
^{10}Be	50°†	5.30(18)	2.75(14)	0.011(9)	1.27(19)	11.3(10)	0.11(3)	0.708	85

TABLE III.3.1 (cont'd.)

^{10}B	50°	6.64(17)	2.79(11)	0.019(3)	2.5(2)	13.6(10)	0.077(14)	1.257	127
^{10}B	70°	6.4(3)	2.8(3)	0.028(5)	4.8(8)	14.6(10)	0.04(6)	0.483	54
^{10}B	90°	14.1(7)	3.4(5)	0.03(1)	4.5(10)	13.8(10)	0.128(11)	0.299	12
^{10}B	50°†	5.18(21)	2.38(8)	0.015(3)	2.4(2)	9.3(10)	0.053(16)	0.773	90
^{11}B	50°	7.06(14)	3.26(9)	0.025(4)	2.22(17)	21.0(17)	0.110(13)	1.081	151
^{11}B	70°	7.05(15)	2.8(2)	0.022(3)	4.0(5)	18.1(10)	0.02(4)	0.773	71
^{11}B	90°	9(14)	2(7)	0.02(5)	3.4(10)	10(4)	0.14(8)	0.492	15
^{11}B	50°†	5.14(15)	2.83(12)	0.015(4)	1.62(14)	10.4(10)	0.079(9)	0.833	121

†50° out of the reaction plane.

TABLE III.3.2 Associated neutron kinetic energy moving source fit parameters.

E/A=20 MeV

		Source #1			Source #2				
IMF	Angle	M_1	T_1	β_1	M_2	T_2	β_2	χ^2/dof	#dof
^{6}Li	50°	5.23(7)	2.54(6)	0.017(2)	0.91(5)	8.2(7)	0.089(6)	1.205	149
^{6}Li	70°	5.13(10)	2.44(8)	0.017(2)	1.38(10)	9.4(10)	0.05(4)	1.167	114
^{6}Li	90°	4.71(17)	2.1(9)	0.02(1)	1.83(17)	9.1(10)	0.034(18)	0.869	89
^{6}Li	50°†	4.71(7)	2.25(7)	0.015(1)	0.73(6)	11.1(10)	0.052(18)	1.196	131
^{7}Li	50°	5.07(5)	2.56(4)	0.019(1)	0.91(4)	11.8(8)	0.065(10)	1.573	176
^{7}Li	70°	4.75(9)	2.24(7)	0.019(1)	1.48(8)	8.5(10)	0.051(7)	1.556	125
^{7}Li	90°	4.91(12)	2.48(11)	0.021(2)	1.34(13)	11.0(10)	0.03(7)	0.818	107
^{7}Li	50°†	4.28(6)	2.36(3)	0.010(1)	0.57(3)	6.3(10)	0.08(4)	1.292	144
^{8}Li	50°	5.03(14)	2.51(12)	0.018(3)	1.08(17)	10.3(10)	0.07(3)	0.823	82
^{8}Li	70°	5.4(3)	2.6(2)	0.025(3)	2.1(4)	10.0(10)	0.02(4)	0.739	51
^{8}Li	90°	5.8(4)	0.59(14)	0.027(3)	5.0(4)	4.5(8)	0.011(1)	0.559	31
^{8}Li	50°†	4.01(18)	2.14(15)	0.009(7)	1.5(2)	9.7(10)	0.08(4)	0.773	62
^{7}Be	50°	3.74(13)	2.92(17)	0.026(3)	0.41(17)	8.2(10)	0.000(3)	1.299	65
^{7}Be	70°	3.8(3)	2.0(3)	0.018(5)	2.6(5)	9.8(10)	0.1(9)	0.894	37
^{7}Be	90°	5.2(7)	4.4(8)	0.02(2)	0.20(93)	9.5(10)	0.0(9)	0.379	8
^{7}Be	50°†	2.82(16)	2.8(3)	0.010(8)	0.01(26)	9.5(10)	0.00(3)	0.743	32
^{9}Be	50°	4.09(15)	2.08(13)	0.022(3)	2.40(15)	7.2(10)	0.028(25)	0.993	87
^{9}Be	70°	5.3(3)	2.20(19)	0.022(3)	3.4(5)	11.1(10)	0.03(6)	0.772	54
^{9}Be	90°	5.8(5)	2.4(6)	0.02(5)	1.9(10)	9.3(10)	0.1(8)	0.509	26
^{9}Be	50°†	3.31(14)	2.24(18)	0.020(3)	1.15(15)	6.1(10)	0.000(1)	0.775	64
^{10}Be	50°	4.84(19)	2.6(2)	0.021(4)	1.5(2)	11.3(10)	0.000(1)	0.819	60
^{10}Be	70°	5.4(4)	1.9(3)	0.024(4)	3.6(7)	11(2)	0.01(5)	0.663	35
^{10}Be	90°	6.4(9)	3.5(8)	0.02(10)	1.1(10)	9.5(10)	0.06(73)	0.229	10
^{10}Be	50°†	4.1(2)	2.5(3)	0.01(2)	0.8(9)	10.0(10)	0.10(17)	0.492	41

TABLE III.3.2 (cont'd.)

^{10}B	50°	4.28(17)	2.8(2)	0.017(5)	1.2(3)	10.0(10)	0.14(9)	0.793	60
^{10}B	70°	5.7(5)	1.4(2)	0.013(8)	6.8(8)	9.7(9)	0.061(57)	0.402	33
^{10}B	90°	9.6(7)	2.5(7)	0.008(8)	1.7(9)	5.0(10)	0.1(9)	0.627	5
^{10}B	50°†	4.7(2)	2.5(3)	0.012(6)	0.6(4)	9.8(10)	0.09(6)	0.548	42
^{11}B	50°	5.29(14)	2.71(13)	0.016(7)	0.97(19)	10.8(10)	0.12(8)	1.054	79
^{11}B	70°	6.5(3)	2.8(2)	0.016(7)	0.8(5)	1.7(6)	0.20(3)	0.667	47
^{11}B	90°	6.6(5)	1.8(7)	0.02(3)	5.0(10)	8.6(9)	0.13(11)	0.380	15
^{11}B	50°†	4.05(13)	2.5(5)	0.011(5)	1.0(3)	9.0(10)	0.15(5)	0.746	57

†50° out of the reaction plane.

coincident charged particle was then the residue from such a decay. For example, in Figure III.3.7 (neutrons in coincidence with ^{11}B at θ=50°, ϕ=0°, from the E/A=35 MeV data) the prominent peak near 7 MeV in the 50° neutron spectrum is due to such a process. The solid lines shown in Figures III.3.6 and III.3.7 represent the double-differential multiplicity as calculated by equation III.3 using the appropriate parameters from Table III.3.1 for each neutron detector angle. While such a line is drawn for the colinear neutron detector, it should be remembered that that detector was excluded when determining the fit parameters.

The errors quoted for the fit parameters are the change in that parameter that corresponds to increasing χ^2 by 1, with all other parameters optimized. For each set of fit parameters, χ^2 per degree of freedom (χ^2/dof) and the number of degrees of freedom (#dof) is given. (The number of degrees of freedom equals the number of data points in the set minus the number of fit parameters, which in this case is six). Caution should be exercised in interpreting the uncertainty of these fits. In some of the cases, the fit parameter errors are smaller than the maximum uncertainty of the fit parameters. This is because χ^2 is not a valid test for very small data sets.

III.3.4 Neutron Relative Velocity

Using a technique developed by Kiss et al. [Ki87] it was possible to interpret the neutron decay of certain states of various nuclides observed in the neutron detectors that were colinear with a silicon telescope and the target. In particular, the present work reports on the neutron decay of the 2.255 MeV excited state of ^{8}Li and

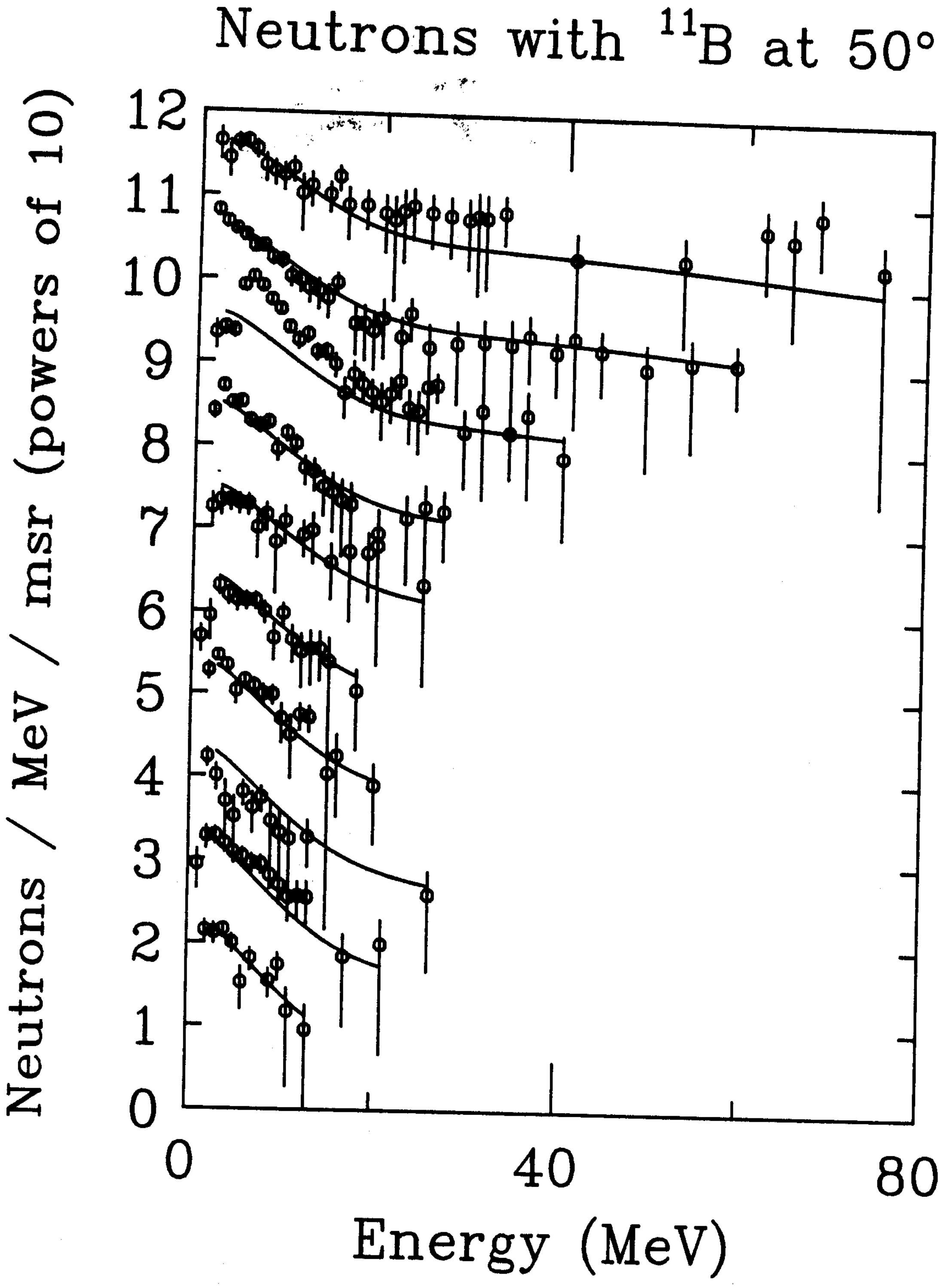

Figure III.3.7 Kinetic energy spectra for neutrons in coincidence with ^{11}B at θ=50°, ϕ=0° (data points) with two-source moving source fit (solid lines), as in Figure III.3.6.

the neutron decay of the 7.456 MeV excited state of ^{7}Li, which feed the ground states of ^{7}Li and ^{6}Li, respectively.

For neutrons in coincidence with each observed isotope, the data were binned into two-dimensional histograms, the x-axis corresponding to relative velocity and the y-axis corresponding to neutron energy. (The relative velocity is defined as the neutron velocity minus the coincident fragment velocity). Figure III.3.8 shows such a histogram for neutrons in coincidence with ^{7}Li from the E/A=35 MeV data. The value of each channel of these histograms was corrected for the neutron detector efficiency for neutrons of the appropriate kinetic energy (previously calculated, as described at the beginning of this chapter), to create a new two-dimensional probability histogram. Then, for each value of the relative velocity, the histogram bins were summed over neutron kinetic energy to give a one-dimensional histogram (with relative velocity the remaining axis). This resulting histogram is the velocity distribution of the neutrons shifted to the moving frame of the coincident fragment on an event by event basis. Figure III.3.9 shows such velocity distributions for neutrons in coincidence with various fragments from the E/A=35 MeV data.

Neutrons from the decay of a relatively narrow discrete state with a small excitation energy in a particular isotope give rise to a peak in the relative velocity distribution for neutrons in coincidence with the daughter nucleus. The histograms shown in Fig. III.3.9 correspond to the decay of the 7.456 MeV state of ^{7}Li, the 2.255 MeV state of ^{8}Li, the 7.371 MeV state of ^{10}Be, the 3.89 MeV state of ^{11}Be, and the 3.388 MeV state of ^{12}B [Aj84, Aj85]. These were observed in coincidence with ^{6}Li, ^{7}Li, ^{9}Be, ^{10}Be, and ^{11}B, respectively, all in the

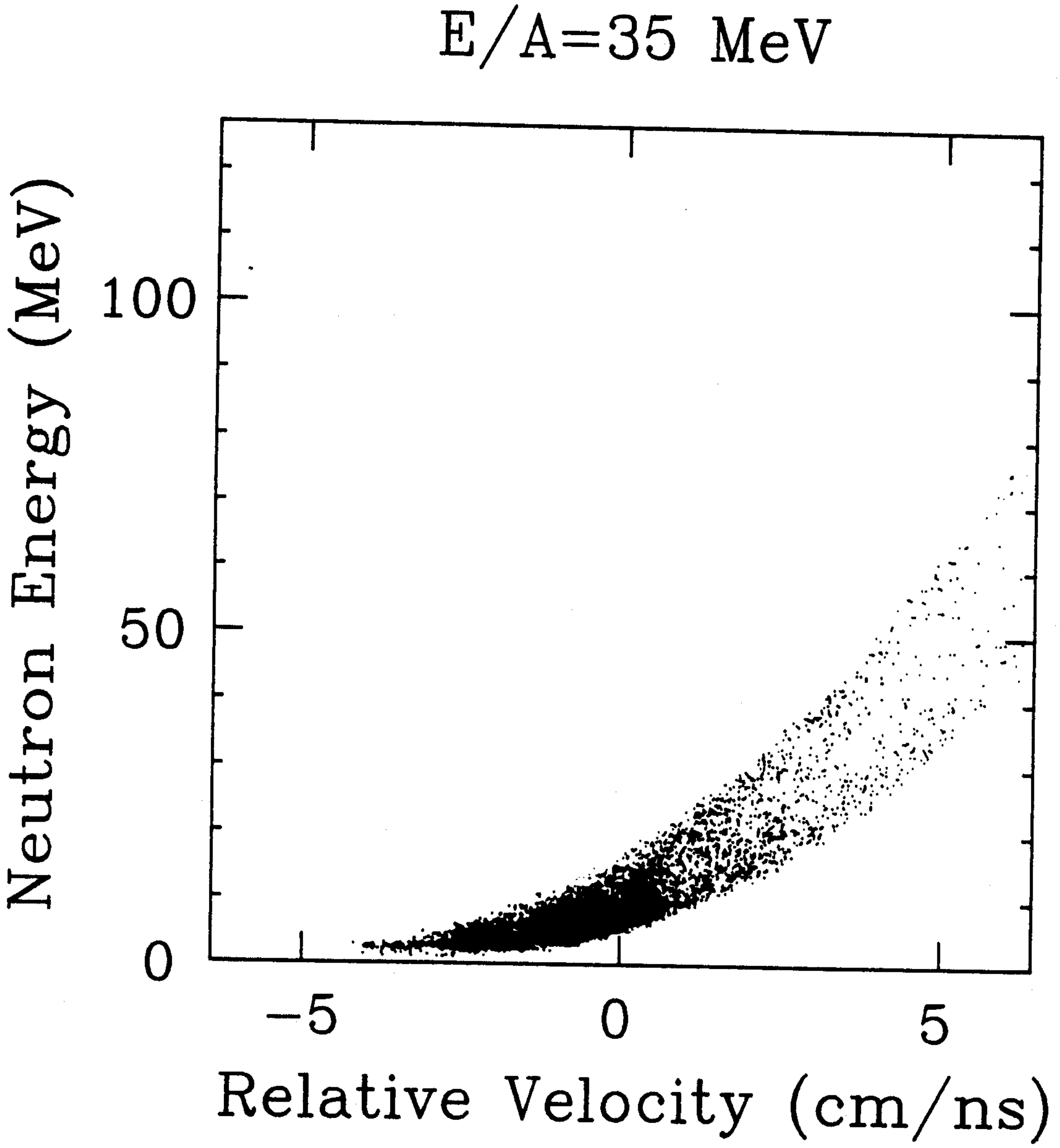

Figure III.3.8 Relative velocity vs. kinetic energy for neutrons in detector-1 in coincidence with ^{7}Li in telescope-1 (50°), E/A=35 MeV.

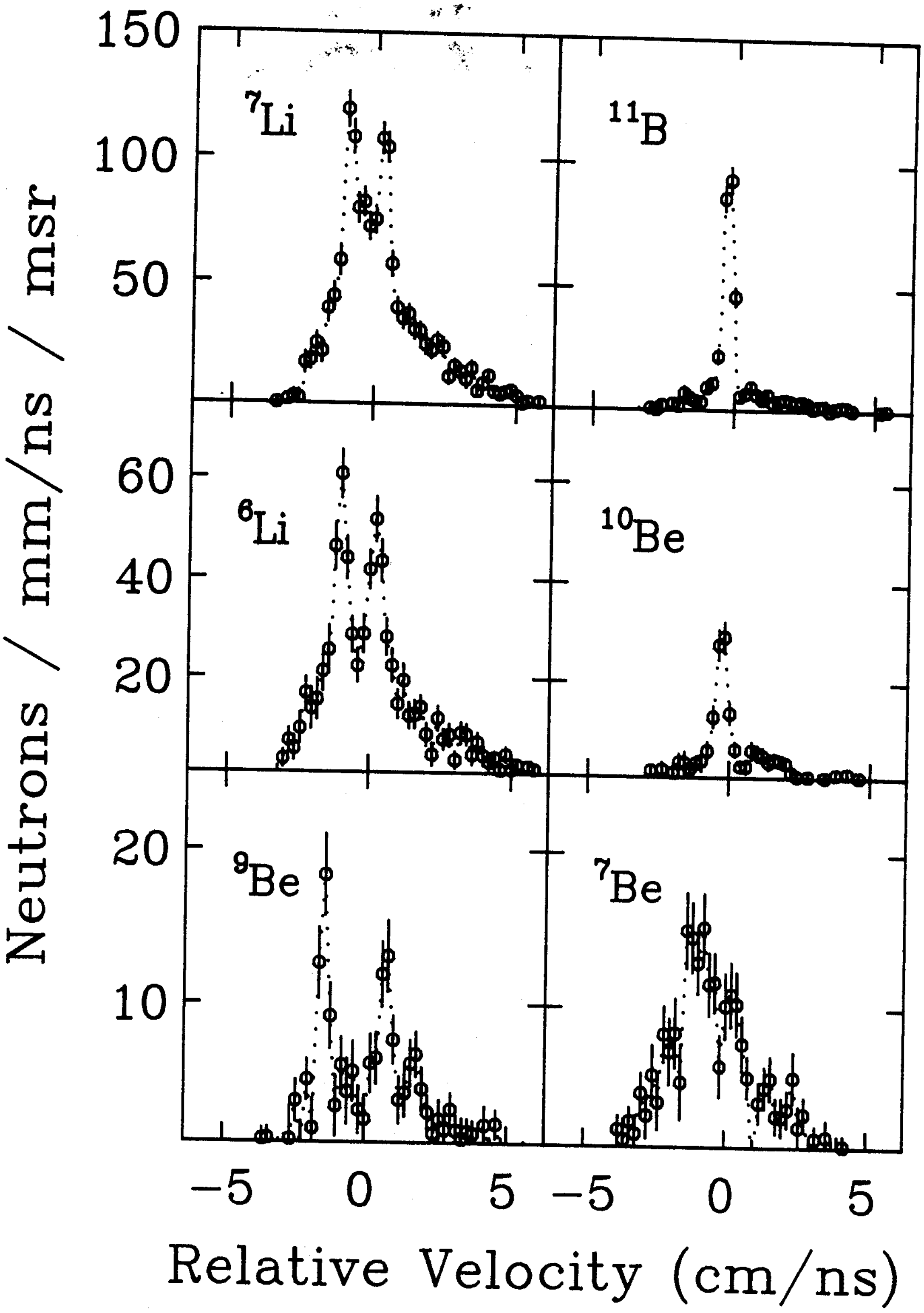

Figure III.3.9 Relative velocity histograms for neutrons in detector-1 in coincidence with fragments in telescope-1 (50°), E/A=35 MeV.

ground state except the ^{10}Be which was in the 3.3680 MeV excited state. Also, the same type of histogram is shown for neutrons in coincidence with ^{7}Be. This shape corresponds to random correlations, where no narrow state with small excitation energy contributes significantly to the coincidences.

In the frame of the parent nucleus, the available kinetic energy, T, is related to the nuclear binding energies, represented by B(Z,N), by:

$$T = B(Z,N-1) - B(Z,N) + E_{ex}(Z,N) - E_{ex}(Z,N-1)$$

where Z and N represent the number of protons and neutrons, respectively, in the parent nucleus, and $E_{ex}(Z,N)$ is the excitation energy of the level in the nucleus identified by Z and N. These kinetic energies (or Q values) are 206 keV, 222 keV, 559 keV, 20 keV, and 19 keV, respectively, for the decays listed [Aj84, Aj85], and correspond to relative velocities of 0.679 cm/ns, 0.698 cm/ns, 1.092 cm/ns, 0.205 cm/ns, and 0.199 cm/ns, respectively. Broad states are not observed because the emitted neutrons do not have a sharp relative velocity. Neutrons from states with large excitation energies are also not observed due to a greatly reduced efficiency (partly the inherent neutron detector efficiency but primarily the geometric efficiency due to kinematic focusing).

In order to determine the number of neutrons from a specific decay process, it was necessary to subtract a background spectrum of neutrons from other processes. Since both the charged particle spectra and the neutron spectra are easily parameterized in terms of moving source fits, their inclusive velocity distributions are equally well known. The parameters from the faster source of the neutron fit also provided a reasonable representation of the charged particle spectra. Using those neutron fit parameters as a representation of the charged particle kinetic energy distribution and the two-source neutron fit parameters as a representation of the neutron kinetic energy distribution, it was possible to calculate the relative velocity distribution between uncorrelated charged particles and neutrons. This uncorrelated thermal relative velocity distribution (shown in Figure III.3.10 as the solid line) was in excellent agreement with the data from non-colinear geometries (not shown) and was subtracted from the relative velocity histogram (the difference is shown in Figure III.3.11) to determine the number of fragments observed in the neutron unstable state.

The geometric efficiency of the neutron detector for observing the decay of a particular state in a given isotope depends on the velocity of the emitting system and the emission velocity of the neutron. This geometric efficiency, $\varepsilon_n(E)$, was determined by a Monte-Carlo calculation as a function of the parent nucleus energy both for neutrons emitted in the direction of the moving system and for neutrons emitted in the opposite direction. An average geometric efficiency, $\langle\varepsilon_n\rangle$, was then obtained by weighting $\varepsilon_n(E)$ by the yield of parent fragments, Y(E), which was determined from inclusive data, integrating over energy and dividing by the total yield. That is,

$$\langle\varepsilon_n\rangle = \frac{\int \varepsilon_n(E)Y(E)dE}{\int Y(E)dE}. \qquad \text{(III.5)}$$

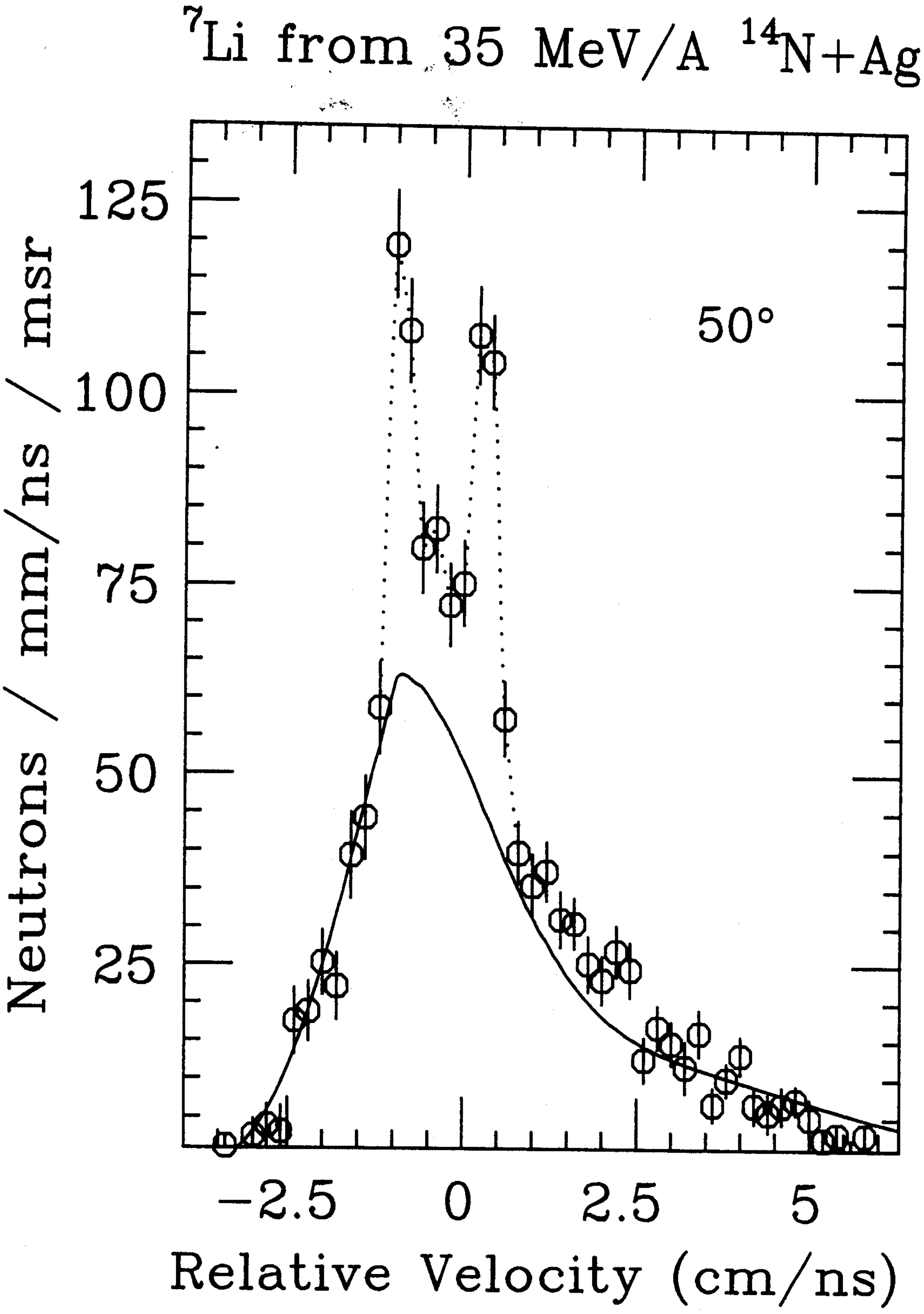

Figure III.3.10 Relative velocity histogram with thermal background for neutrons in detector-1 in coincidence with ^{7}Li in telescope-1 (50°), E/A=35 MeV.

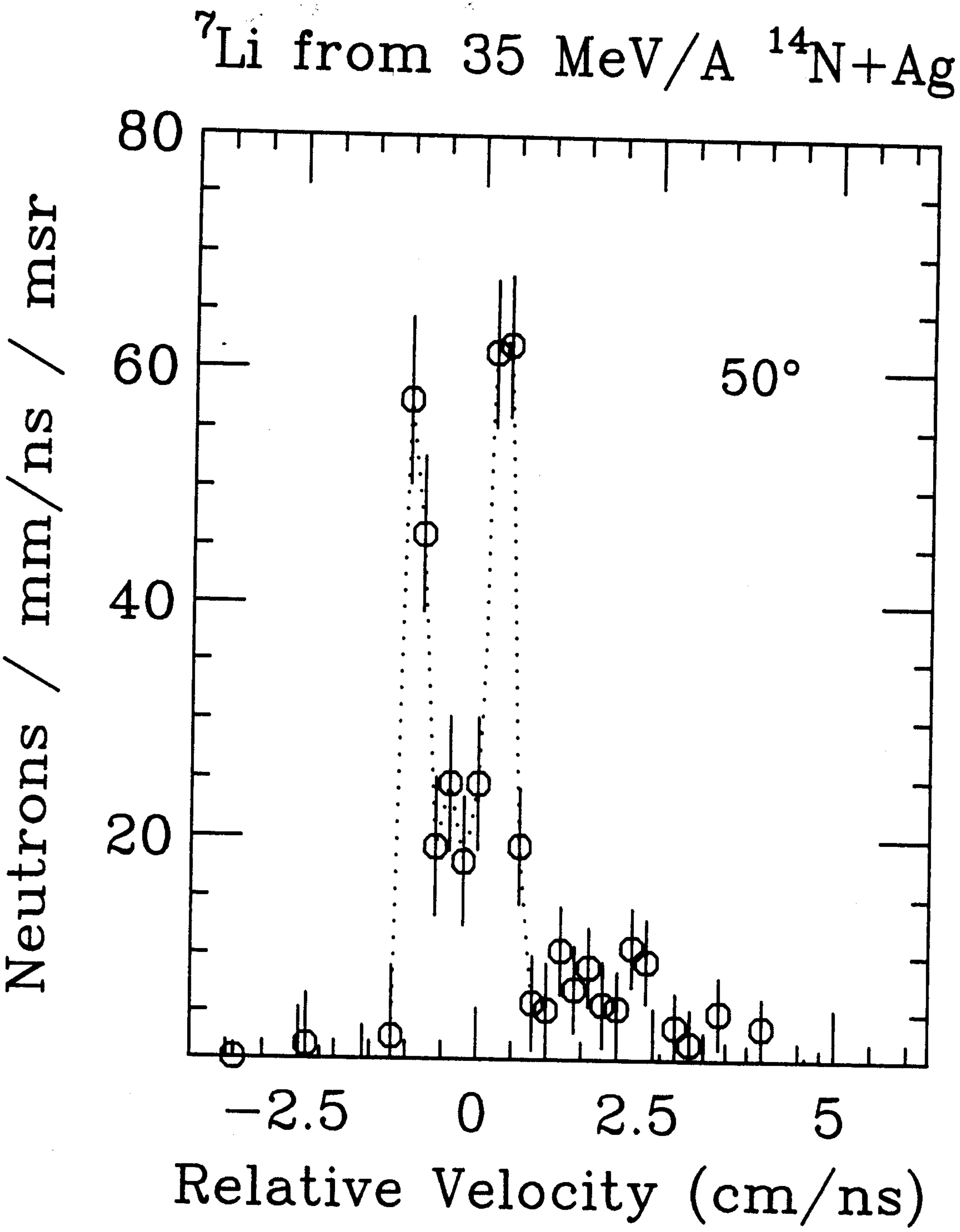

Figure III.3.11 Relative velocity histogram minus the thermal background, for neutrons in detector-1 in coincidence with ^{7}Li in telescope-1 (50°), E/A=35 MeV.

Appendix B gives a detailed description of the calculation of $\langle \varepsilon_n \rangle$ for each case, and the resulting values are listed in Table III.3.3. The number of neutrons observed in each peak was then divided by the average efficiency (for the 2.255 MeV state of ^{8}Li, $\langle \varepsilon_n \rangle$=4(1)% for the neutrons emitted forward in the moving system and $\langle \varepsilon_n \rangle$=2.5(6)% for those emitted backward in the moving system) to give the total number of fragments in the particular neutron emitting state. A similar analysis of neutron emission for each state and isotope listed above was used to determine the number of fragments in each of those excited states. In the case of the 7.456 MeV excited state of ^{7}Li, the total ^{7}Li yield was corrected for ^{8}Be contamination [Bl86] (about 20% of the observed ^{7}Li yield for E/A=35 MeV and 13% for E/A=20 MeV, as shown in Appendix A of this thesis). In addition, the results were corrected for the fact that this state branches to ^{6}Li+n 77% of the time (and to α+t the rest of the time) [Aj84].

Table III.3.4 contains the ratio of the population of neutron unbound excited states of various nuclei to the populations of the ground state and any bound excited states with previously measured populations of the same nuclei. The populations of the bound 0.478 MeV state in ^{7}Li and 0.9808 MeV state in ^{8}Li were taken from Refs. Bl86 and Mo85 respectively. Using equation (I.1) to relate these ratios to temperatures gives the values shown in Table III.3.4. The ratio of the populations of the second to the first excited state of ^{8}Li is beyond the maximum allowed by their spin factors (7/3), but this is primarily due to the large uncertainty in the excited state fraction reported in Ref. Mo85. The calculated temperature of 2.8(3) MeV (from ^{7}Li (7.456) and ^{7}Li (0.478)) is higher than the 0.54 MeV observed with the bound

TABLE III.3.3 $\langle \varepsilon_n \rangle$ (as described in the text) in percent for the decays and beam energies listed.

Decay	E/A=35 MeV forward	E/A=35 MeV backward	E/A=20 MeV forward	E/A=20 MeV backward
^{7}Li(7.456) to ^{6}Li(g.s.)	4.5(11)	2.8(7)	4.3(11)	2.6(6)
^{8}Li(2.255) to ^{7}Li(g.s.)	4.2(11)	2.5(6)	4.0(10)	2.3(6)
^{10}Be(7.371) to ^{9}Be(g.s.)	2.2(6)	0.9(2)	2.1(5)	0.8(2)
^{11}Be(3.89) to ^{10}Be(3.368)	32(10)	29(9)	30(10)	27(9)
^{12}B (3.388) to ^{11}B (g.s.)	34(11)	32(11)	33(11)	30(10)

TABLE III.3.4 Excited state ratios, R, and their corresponding temperatures, kT, from equation I.1. (not corrected for sequential decay).

States Compared	E/A=35 MeV: R (ratio)	kT (from Eq. I.1)
^{7}Li(7.456) to ^{7}Li(g.s.)	0.05(1)	2.2(2) MeV
^{7}Li(7.456) to ^{7}Li(0.478)[a]	0.24(6)	2.8(3) MeV
^{8}Li(2.255) to ^{8}Li(g.s.)	0.40(8)	1.8(3) MeV
^{8}Li(2.255) to ^{8}Li(0.9808)[a]	7.4±6.9	≧ 0.8 MeV
^{10}Be(7.371) to ^{10}Be(g.s.)	0.22(5)	2.13(15) MeV
^{12}B (3.388) to ^{12}B (g.s.)	0.334(7)	1.74(2) MeV

States Compared	E/A=20 MeV: R (ratio)	kT (from Eq. I.1)
^{7}Li(7.456) to ^{7}Li(g.s.)	0.031(7)	1.9(1) MeV
^{7}Li(7.456) to ^{7}Li(0.478)[a]	0.36(13)	3.3(6) MeV
^{8}Li(2.255) to ^{8}Li(g.s.)	0.32(6)	1.5(2) MeV
^{10}Be(7.371) to ^{10}Be(g.s.)	0.20(5)	2.07(15) MeV
^{12}B (3.388) to ^{12}B (g.s.)	0.270(6)	1.57(2) MeV

[a] Population of γ-emitting states from Refs. Mo85 and Bl86.

excited state [B186]. This is qualitatively consistent with feeding arguments since the present measurement does not involve the ground state and should therefore be less susceptible to the effects of feeding from sequential decay. However, the temperature of 2.8(3) MeV is still somewhat lower than those based on charged-particle unbound levels reported in Refs. Po85a and Ch86a.

The feeding of the ^{7}Li yield from the 2.255 MeV state in ^{8}Li is defined as the number of ^{8}Li in that state (as determined above) divided by the total number of observed ^{7}Li (corrected for ^{8}Be contamination). Table III.3.5 gives the feedings to the ground states from the observed neutron unbound states. In the case of the 3.89 MeV excited state of ^{11}Be, the observed decay was to the 3.3680 excited state of ^{10}Be. The quoted feeding is to the ground state of ^{10}Be via this branch. The branching ratio for the decay of the 3.89 MeV excited state to the ground state of ^{10}Be is unknown, and this feeding was not measured. The amount of feeding of the ^{7}Li inclusive yield from sequential decay of the 2.255 MeV state in ^{8}Li is 7(1) percent for the E/A=35 MeV data, a fairly small value. Similarly, the feeding of the ^{7}Li inclusive yield via the same decay channel is 4(1) percent for the E/A=20 MeV data. These feedings alone will produce only a small correction in the temperatures extracted in Ref. B186, which still gives temperatures less that 1 MeV. However, note that these measurements are only of one decay channel. These single values must be used in conjunction with a model for the sequential decay to estimate the total feeding from all possible decay channels, as discussed later in this thesis.

TABLE III.3.5 Feeding (in percent) of the ground state of A(Z,N) from the neutron-unbound excited state of A(Z,N+1).

Excited State	State Fed	E/A=35 MeV	E/A=20 MeV
^{7}Li(7.456)	^{6}Li(g.s.)	3.9(8)	2.7(6)
^{8}Li(2.255)	^{7}Li(g.s.)	7.1(13)	4.4(9)
^{10}Be(7.371)	^{9}Be(g.s.)	14(3)	11(3)
^{11}Be(3.89)	^{10}Be(g.s.)[b]	1.1(4)	1.1(4)
^{12}B (3.388)	^{11}B (g.s.)	4.39(4)	3.66(4)

[b] This is only the feeding through the ^{10}Be(3.3680) state; the feeding through the branch directly to the ground state is unknown.

III.4.Errors

Considerable beam time (about 1/3 of the total experiment) was devoted to the shadow bar runs so that their statistical uncertainty would not contribute significantly to the final data. On-line estimates of the coincident neutron count rate indicated a shadow-bar-in to shadow-bar-out ratio of ~1/4. In order to minimize the net statistical uncertainty, this implied the beam time ratio should be the square-root of that number, or 1/2. The net statistical uncertainty was obtained by taking the square root of the sum of the squares of the individual uncertainties. The systematic errors in the present data are primarily due to uncertainties in determining the neutron detector efficiency (±10%), the geometrical efficiency for observing the decay, and the thermal background subtracted from the relative velocity distributions.

A possible error in the geometric efficiency is that due to misalignment of the silicon telescope and the neutron detector in the colinear geometry. Any misalignment of the detectors will result in overestimating the geometric efficiency, and hence underestimating the yield from the state in question. However, due to the large target-to-detector distance of 130 cm, it was possible to position the neutron detectors such that their angles were known to ±0.1°, which introduced a relatively insignificant effect on the geometric efficiency. A finite-sized beam spot and possible error in centering the beam have much greater effect on the efficiency. In this experiment, the beam spot diameter was approximately 3 mm, and we estimate that it was within 2 mm of the geometric center. Therefore, the beam was contained within 3.5

mm of the geometric center with an average distance of less than 2 mm from the center. Since the ΔE elements of the silicon detectors were 176 mm from the target, this produced an average effective detector misalignment of about 0.6 degrees. The geometric efficiency is quite sensitive to this misalignment. For example, an error of 1° reduces $\langle \varepsilon \rangle$ by 1/3, which produces a 50% increase in the calculated populations. The values and uncertainties given throughout this thesis for the geometric efficiencies reflect the size and location of the beam spot.

The major source of error in the thermal background is not due to uncertainty in the parameters or the calculation, but rather in that we ignore the possibility of large angle correlations. Such correlations could reduce the normalization of the background by as much as 40%, which would increase the measured value of the unbound excited state populations. However, the model gives a good fit to the spectrum away from the peaks.

Combining these uncertainties with the statistical errors (12 to 20%) gives the results shown in Table III.3.4 (with total uncertainties typically less than 30%). While the uncertainty may seem large, it does not significantly change any of the conclusions made here. The dependence of the temperature given by equation (I.1) on the ratio is very slow in this neighborhood. For instance, increasing the ratio of the populations of the 7.456 MeV state to the 0.478 MeV states in ^{7}Li from 0.24 to 0.31 (a 30% increase) only increases the temperature from 2.8 to 3.1 (an 11% increase). To reflect a temperature of 5 MeV, this ratio would have to be 0.743, more than twice as large as observed.

CHAPTER IV: DISCUSSION

IV.1 Fragment Moving Source Fits

For each isotope identified, the kinetic energy spectra from each angle were fit by a moving source model with one single parameter set, as described in Chapter III. This is commonly done [e.g. Aw80, Aw81a, Aw81b, Aw82, Ch86b, Fi84, Fi86, Po85a, We78, We82, We84], and it is done here for two reasons: one, so this data would be easily comparable to other such measurements, and two, because it provides a reasonable parameterization of the data. It should be stressed that this is only a parameterization and the concept of a single moving source with a unique temperature is not to be taken literally. A more plausible description is that this source represents an ensemble average of sources with a continuum of velocities and temperatures [Fi86, Bl87b]. Chitwood et al. [Ch86b] show three models with distinct physical differences that can fit this type of data equally well over this angular range. The fit parameters depend strongly on the model used, with cross sections differing by as much as a factor of two [Ch86b].

The values observed here are entirely consistent with both previous measurements [Mo84, Mo85] and predictions based on similar reactions [We84, Fi86, Ch86b]. As mentioned previously, the resulting parameters are fairly independent of the isotope considered. This fact is one of the primary motivations for a thermal model. However, any such model could have systematic errors which affect each observed slope identically and which would change a set of self-consistent temperatures into a different yet still self-consistent temperatures. For example, thermal models generally ignore rotational energy. This energy is fixed by angular momentum conservation, and should not be treated thermodynamically. Secondly, the treatment of the Coulomb shift is fairly critical. Each different way of estimating this quantity produces a different set of self-consistent temperatures. (This correction is at best an estimate. The magnitude is generally unknown, unless the target residue is detected. Even then, a two body process must be assumed). While one method will usually produce the lowest value for χ^2, there is some uncertainty in the significance of that result. The dependence of χ^2 on the Coulomb shift is most sensitive to the shape of the spectrum near the peak which is due to a combination of effects including the Coulomb barrier. However, this is also usually quite near the lower threshold of typical silicon detectors, particularly for the heavier fragments. There is, naturally, always a question of whether the shape there is due to a change in the detector efficiency near its threshold. For these reasons, the kinetic energy slope parameter is best interpreted as being related to the temperature but not necessarily equal to it. (Certainly, for the same method of determining the fits and for the same detector, a higher slope parameter implies a higher temperature). In this data, we have inclusive spectra at only 3 angles (50°, 70°, and 90°) over a limited angular range (40° in the lab). The fits to this data are not to determine the moving source parameters but to show consistency with fits to previous measurements. Finally, it should be noted that the fits to the ^{7}Li spectra (at both E/A=20 and 35 MeV) have the largest value for χ^2. This can be attributed to the contamination of these spectra by α pairs from the decay of ^{8}Be [B186]. The spectra of α pairs has a different shape due to the geometric efficiency for detecting the coincident pair (see Appendix A for a detailed explanation).

IV.2 Neutron Kinetic Energy Spectra Fits

IV.2.1 Two-source Moving Source Model - Source #1

The spectral shape of neutrons in coincidence with intermediate mass nuclei emitted at 50°, 70°, and 90° from the reaction of both 20 and 35 MeV/A ^{14}N on Ag clearly suggests two moving sources. For E/A<5 MeV, neutron spectra can be parameterized as being emitted from a single moving source [Hi79]. For greater bombarding energies, another process of neutron emission, which can be characterized by a second moving source, is observed [Ga71]. For the present data, a two-source moving source fit provides an excellent parameterization (χ^2 typically less than 1.3) in terms of the source velocities, the associated neutron multiplicities, and the slope parameters ("temperatures"). Unlike the charged particle data, no Coulomb shift is necessary in these fits. While two moving sources provide an accurate description, a third source leads to ambiguous results. This was demonstrated by Holub et al. [Ho86] for very similar data with three-source fits. In the present work, the slower source source has a velocity of about 65% of the center of mass velocity for E/A=35 MeV and 80% for E/A=20 MeV (or 7 to 9% of the beam velocity), while the faster source has a velocity slightly less than half the beam velocity for each energy (actually about 35% of the beam velocity).

The mechanism responsible for the emission of neutrons from the slower source is certainly better understood than for the faster source. For sufficiently low beam energies (E/A<5 MeV) emission from this slower source is observed exclusively [Pe77, Ey78, Ge78, Hi78, We78b, Hi79]. At those energies, the projectile and target form a compound nucleus (for central collisions) which de-excites via neutron emission (among other processes). The compound nucleus is sufficiently long lived for the following to occur. First of all, no nucleons escape before the formation, so all of the beam's energy and momentum is transferred to the compound system. Secondly, the energy is distributed sufficiently throughout all of the nucleons in the system such that statistical descriptions are accurate. To that extent, the system has thermalized or reached equilibrium. The velocity obtained from moving source fits of the observed neutron spectra is the center of mass velocity. The slope parameter obtained from such fits will be related to the compound nucleus temperature by a factor of 12/11 [Le59]. (The temperature of the compound nucleus is before any neutron emission, and hence before any cooling. For multiple neutron emission, the typical sampled neutron is emitted after some cooling has occurred, and hence the slope parameter will be reduce by some amount. To get the original temperature, the slope parameter must be multiplied by 12/11 [Le59]).

As beam energies are increased beyond 5 MeV/nucleon to the levels studied here, this process evolves into a slightly different process. Less than all of the nucleons combine to form the resulting compound system. This process is called incomplete fusion, and the compound system that is formed is referred to as the target residue. The target residue is not unique; the number of nucleons involved will be a finite distribution about some average, reflecting the variations in impact parameters. Since some of the nucleons do not participate in the incomplete fusion, some of the momentum and energy from the beam will be "lost". The velocity of the target residue is determined by the center of mass momentum minus the "missing momentum". Similarly, the temperature of the target residue is determined by the energy available in the center of mass, minus that carried off by other particles. This is consistent with what is observed for the slower of the two moving sources. At each beam energy, the source velocity is somewhat less than the center of mass velocity, indicating incomplete momentum transfer from the beam. The lower beam energy is closer to energies at which compound nucleus reactions are observed, and the target residue velocity observed in that case is closer to the center of mass velocity than for the higher beam energy. An increase in the beam energy from 280 MeV to 490 MeV would correspond to a 32% increase in the temperature based on the simple equation applicable to a Fermi gas:

$$E^{*} = a\,T^{2} \qquad \text{(IV.1)}$$

(where E^{*} is available excitation energy, a is the level density, and T the temperature), but only a 20% increase is observed for typical values found in Table III.3.1 and III.3.2. This again suggests that an increase in the beam energy corresponds to a smaller fraction of that energy being transferred to the target residue. So this source is similar to the compound nucleus and can be readily understood in that framework.

The associated neutron multiplicities observed for the target residue source are consistent with those observed by Remington et al. [Re86], who measured the multiplicities for neutrons in coincidence with intermediate mass fragments (IMF's) observed at forward angles (7° to 30° in the lab) from the reaction of $^{14}N+^{165}Ho$ at E/A=35 MeV. Specifically, the "target-like source" multiplicities for "high energy" fragments from that work should be considered. The Remington data clearly exhibit an increase with increasing lab angle. Extrapolating to 50° would result in associated multiplicities of around 10, slightly higher than those reported here for reactions at E/A=35 MeV (typically 6 to 7). The multiplicities reported here do not show any dependence on the lab angle of the coincident IMF. The conclusion is that this dependence ends somewhere between 30° to 50°, where the maximum value is reached. In that sense, an IMF at a large lab angle ($\theta \geqq 50°$) is a good indication of a central collision. Additionally, no left-right asymmetry (i.e. difference between the associated multiplicity for neutrons on the same side of the beam as the coincident IMF and that for neutrons on the opposite side of the beam as the coincident IMF) is observed. This is consistent with what is observed for strongly damped projectile like fragments in similar reaction [Ca85, Ca86, Re86], in contrast to what is seen for quasi-elastic projectile-like fragments. This is evidence that an IMF observed at a large angle is a good trigger for central collisions. In addition, recoil effects [Ca86] are not going to be pronounced, since the coincident IMF is only a small fraction of the total mass and momentum, and is not a strong trigger for the reaction plane or the target residue recoil.

Finally, by comparing the multiplicities from the two θ=50° detectors (one in the plane of the neutron detectors, ϕ=0°, and the other at ϕ=90° with respect to the plane determined by the neutron detectors) we can determining the out-of-plane anisotropy,

$$A_2 = \left[\frac{d\sigma}{d\Omega}(\phi=0°) \;/\; \frac{d\sigma}{d\Omega}(\phi=90°)\right] - 1. \qquad \text{(IV.2)}$$

For both E/A=35 MeV and E/A=20 MeV data, A_2=0.2(1) for the target residue source. This anisotropy greater than zero indicates one of the limitations of the moving source model. The description of the neutron kinetic energy spectra given by equation III.3 assumes isotropic emission. The observed anisotropy indicates that there is actually a preferred plane of emission. Actually, one would expect emission to occur preferentially in the plane perpendicular to the angular momentum vector of the system. The observed anisotropy reflects not only the strength of that preference (which should be determined by the magnitude of the angular momentum relative to the emission temperature) but also the degree to which the observed IMF determines the reaction plane.

IV.2.2 Two-source Moving Source Model - Source #2

Typically, the process that is parameterized by the faster source is described as non-equilibrium or pre-equilibrium (PE) neutron emission [Ga71, Hi79]. Pre-equilibrium neutron emission occurs in the early stages of formation and prior to the thermalization of the target residue. While this process has been observed for some time, it is far from understood. Several distinctly different models have been suggested to explain this process [Ge77, Gr77, We77, Bo80, Bl85], each meeting with limited success. However, the moving source parameterization has been quite successful at describing the observed spectra. Typically, such a moving source has a velocity parameter slightly less than half of the beam velocity. This suggests that such emission occurs early in the collision process, specifically, after each projectile nucleon has undergone only a single nucleon-nucleon collision (accounting for the velocity equal to 1/2 of the beam velocity).

In the framework of these coincidence measurements, the importance of the PE neutron source is emphasized by the similarity between those fit parameters (given in Tables III.3.1 and III.3.2) and those for the intermediate mass charged particle inclusive spectra (given in Tables III.2.1 and III.2.2). Indeed, considering the uncertainty in the parameters due to the Coulomb shift, the parameters are similar to suggest they are parameterizations of the same moving source. (However, since this is just a model that parameterizes the data, it is not possible to conclude that the same physical process is responsible for the emission of both these neutrons and intermediate mass charged particles). In the discussion of the de-excitation of these intermediate mass fragments via final state interactions, only the PE neutrons (not the sequential neutrons from the target residue) can play a role. The model assumes a single thermal source for the fragments and the neutrons, which can then only be the PE neutron source. Secondly, the neutrons from the target residue occur in a sequential process, and could not all be available for final state interactions with a single intermediate mass fragment (the time of emission is too long). This process (final state interactions), is discussed later in this chapter.

The associated PE neutron multiplicities for the E/A=35 MeV data (given in Table III.3.1) are consistent with predictions by Fields et al. [Fi86] from associated proton PE multiplicities from a very similar reaction (^{32}S+Ag at E/A=22.5 MeV). Again, as with the neutrons emitted from the target residue, no left-right asymmetry is observed. For the E/A=35 MeV, A_2=0.5(2) while for the E/A=20 MeV data, A_2=0.4(2) for the PE source. This anisotropy is greater than that observed for the target residue source. Qualitatively, this is predicted by the theory of Ericson and Strutinsky [Er58] which says that the out-of-plane anisotropy should increase with a decrease in the moment of inertia of the source.

IV.2.3 Harp-Miller-Berne Model

The Harp-Miller-Berne model (HMB) as modified by Blann [Bl81] for heavy-ion reactions, predicts the time evolution of the system with the Boltzmann master equation. The model considers the target+projectile system in terms of single particle occupation probability densities for the total excitation energy available. For a given number of initial degrees of freedom, the model lets the system relax via either internal nucleon-nucleon scattering or particle emission over finite time steps ($\Delta t = 2.1 \times 10^{-23}$ s). The model can then predict the observed emission after any number of time steps. In the simplest model, the number of initial degrees of freedom, or exciton number n_0, is equal to the number of projectile nucleons, A_p [Bl81].

Other descriptions suggest that n_0 should equal A_p+3, to approximate effects due to collective degrees of freedom [Bl81, Bl85, Ho86]. In addition, empirical results from some works have suggested an energy dependence for n_0 [Aw82, Ho83, Ho86]. The exciton number is primarily responsible for the shape of the energy distribution predicted by the HMB model [Bl81]. The overall normalization is determined by the intranuclear transition rates, which are fixed parameters in the model [Bl81].

Since the HMB model is a phase space calculation, it only predicts the neutron energy distribution, $\frac{d\sigma}{dE}$. The prediction does not depend on the fragment with which the neutrons are in coincidence. From the results shown in Tables III.3.1 and III.3.2, the neutron moving source fit parameters do not depend strongly on the coincident isotope. For that reason, neutrons associated with a specific fragment (^{7}Li is chosen as it has the best statistics) will be compared directly to the HMB model predictions. Equation III.3 gives $\frac{d^2\sigma}{dEd\Omega}$ in terms of the moving source fit parameters. Integrating that equation over solid angle, $d\Omega$, gives [Hi79]:

$$\frac{d\sigma}{dE} = \sum_{i=1}^{2} \frac{M_i}{\sqrt{\pi\varepsilon_i kT_i}} \exp[-(E+\varepsilon_i)/kT_i] \times \sinh\left(\frac{2\sqrt{\varepsilon_i E}}{kT_i}\right). \qquad \text{(IV.3)}$$

Putting the fit parameters for neutrons in coincidence with ^{7}Li (averaged over the 50°, 70°, and 90° in-plane fragment angles) from Table III.3.1 (including the errors on the parameters) into the above equation for discrete energies (E) gives the <u>points</u> plotted in Figures IV.2.1. (for E/A=20 MeV) and IV.2.2 (for E/A=35 MeV). It is important

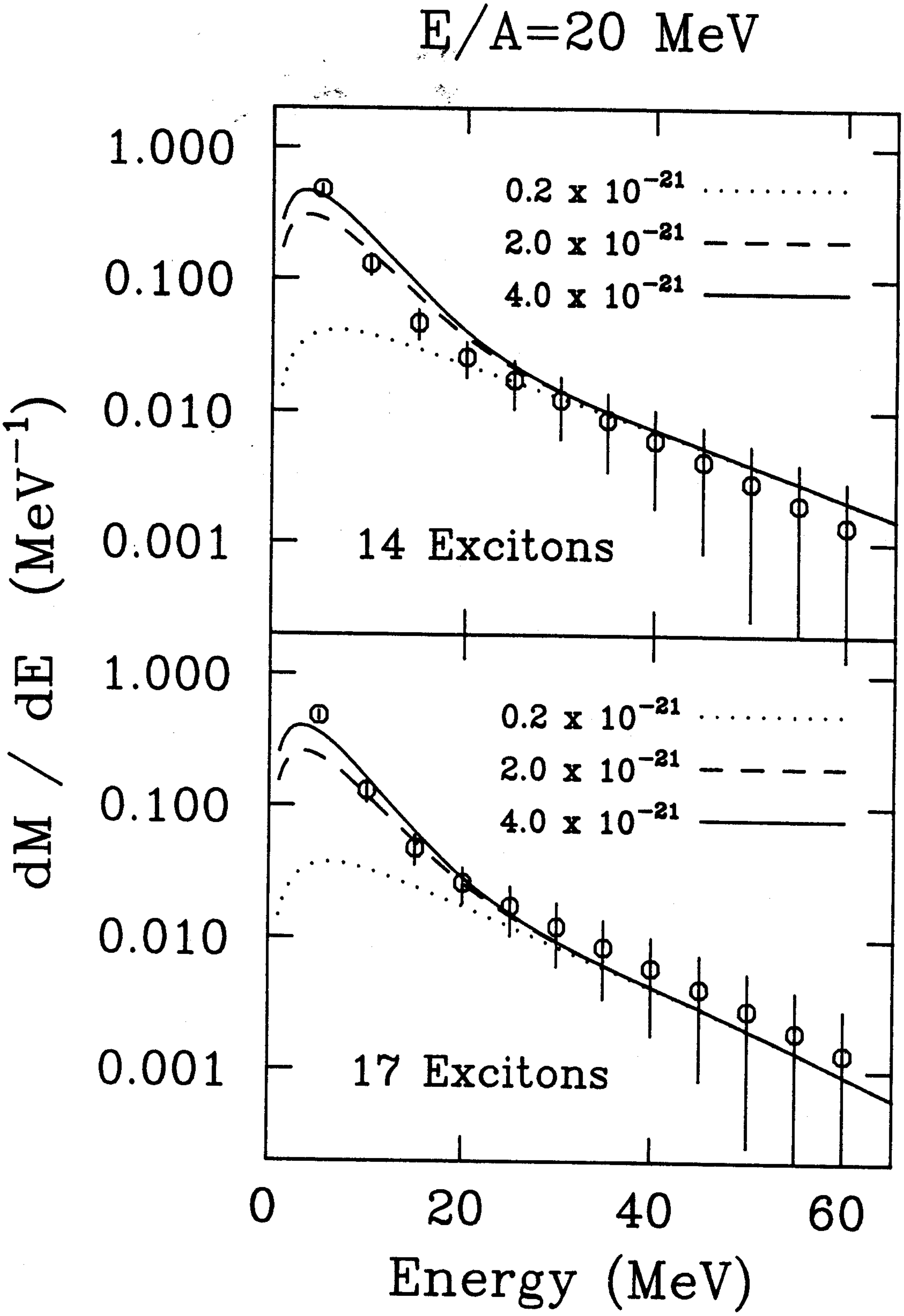

Figure IV.2.1 Neutron energy distribution from moving source model (representative points plotted) compared to that from Harp-Miller-Berne Model (lines) for E/A=20 MeV.

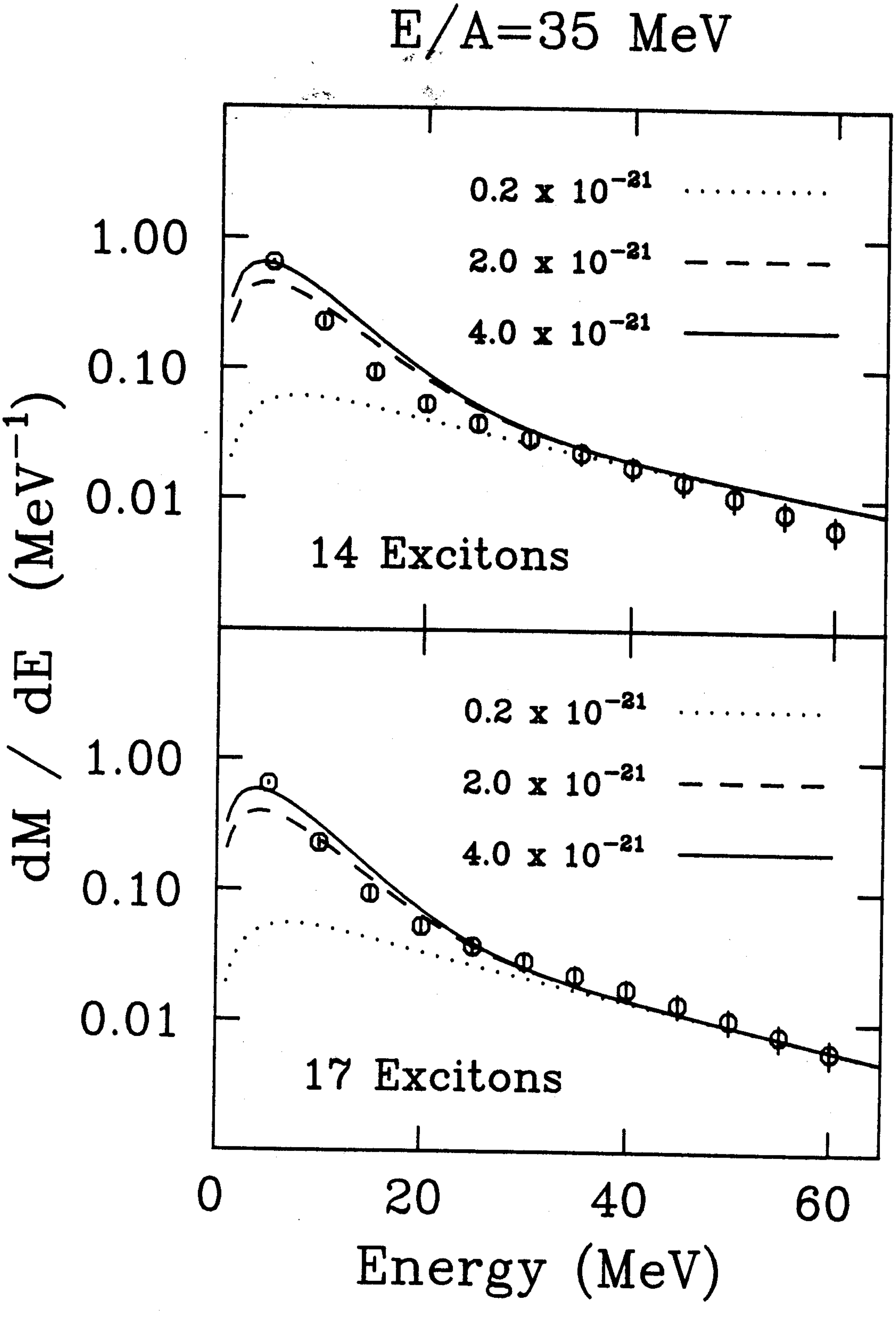

Figure IV.2.2 Neutron energy distribution from moving source model (representative points plotted) compared to that from Harp-Miller-Berne Model (lines) for E/A=35 MeV.

to note that while the normalization of the moving source model is a fit parameter, the normalization of the HMB model is absolute, as plotted.

Generally, the agreement between the moving source model and the data is excellent (for each type of coincident IMF, for each IMF angle, and for both beam energies). For convenience, the HMB model is compared to the moving source model, rather than the data. (The moving source model can easily be integrated over solid angle to obtain the energy distribution, which is predicted by the HMB model). As stated earlier, the most naive approach suggests that $n_0=A_p$, while a first change from that might be $n_0=A_p+3$. Calculations based on these two choices are shown in Figures IV.2.1 (for E/A=20 MeV) and IV.2.2 (for E/A=35 MeV). In each figure, the HMB model predictions are shown for three time slices in the reaction: t=0.2, 2.0, and 4.0×10^{-21} seconds after the collision. Considering primarily the high energy end of the neutron spectrum, the best agreement between the two models (and hence between the HMB model and the data) occurs for $n_0=17$ ($=A_p+3$) for the E/A=35 MeV data. For the E/A=20 MeV data, it is not clear which value, $n_0=14$ or $n_0=17$, is better, but these values seem to provide reasonable limits on the exciton number. Certainly this range of variation in the exciton number is sufficient to describe all of the data presented here.

These results contrast somewhat to those presented in Refs. Aw82, Ho83, and Ho86. In their paper on light particle emission from $^{16}O+^{197}Au$ reactions at 140, 215, and 310 MeV, Awes et al. report that to describe the proton spectra, exciton numbers of 18, 25, and 30 must be assumed for the three beam energies, respectively [Aw82]. In addition, in both Ho83 and Ho86, agreement between the HMB model and the neutron data could be obtained only with arbitrary normalizations. In addition, Holub et al. summarize what is described as an energy dependence of n_0. The dependence is given as a function of $(E_{cm}-V_c)/\mu$, where E_{cm} is the center of mass energy, V_c is the Coulomb barrier, and μ is the reduced mass. For the present work, this value is 16 and 31 MeV/nucleon for E/A=20 MeV and E/A=35 MeV, respectively. These results support the statement in Ho86 that for $(E_{cm}-V_c)/\mu \geq 20$ MeV/nucleon n_0 is constant at roughly A_p+3. However, based on the E/A=20 MeV data where $(E_{cm}-V_C)/\mu=16$, the present work does not support the observation of a pronounced rise in n_0 above A_p+3 for $5 \leq (E_{cm}-V_c)/\mu \leq 20$ MeV/nucleon. In the present work, no energy dependence of n_0 is seen beyond a possible rise from $n_0=A_p$ to $n_0=A_p+3$. In both that respect and the overall normalization of the HMB predictions, the HMB model appears to agree with the data very well.

Finally, the HMB model predicts the time evolution of the system. The predictions given by this model are entirely consistent with the two-source moving source model and more quantitative. From Figs. 4.2.1 and 4.2.2, it can be seen that the PE component of the evaporation occurs entirely within the first 0.2×10^{-21} s. On the other hand, it takes 10 to 20 times as long for the target residue to reach equilibrium. This reinforces the moving source model description of the PE neutron emission being very prompt, and the target residue emission being of a compound nucleus like sequential nature (hence it occurs over a much longer time span).

IV.3 Final State Interactions

One mechanism previously put forth to reconcile the low temperatures reported in Refs. Mo84, Mo85, and Bl86 is cooling via final state interactions [Bo84b]. Fragments emitted in excited states can be de-excited by interactions with other simultaneously emitted fragments, which would lead to a low observed excited state population. In his estimate of this effect, Boal assumes the ^{7}Li coincident fragment multiplicity has the equivalent cross section of 20 neutrons [Bo84b]. Based on the neutron multiplicities reported in this thesis and light charged particle multiplicities reported for a similar reaction [Fi86], a better estimate of the effective cross section is possible.

In his paper on final state interactions [Bo84b], Boal addresses the de-excitation of ^{7}Li from its first excited state (0.478 MeV) via collisions with other nuclei being emitted from the same thermal system. These de-excitations will result in a low apparent temperature based on observed excited state populations. In comparing the observed temperature, T^*, to the actual temperature, T_0, Boal writes:

$$\frac{T^*}{T_0} = \left\{ \frac{\Delta^4 \pi^4 \mu}{m A^2 \sigma^2} \right\}^{1/3}, \qquad \text{(IV.4)}$$

where Δ is related to the spatial extent of the expanding nucleon gas, specifically,

$$\Delta = \frac{R}{\sqrt{5}} = \frac{1.2 \times A^{1/3}}{\sqrt{5}} \text{ fm}, \qquad \text{(IV.5)}$$

μ is the ^{7}Li-n reduced mass,

$$\mu = \frac{7 \times 1}{7 + 1} m, \qquad \text{(IV.6)}$$

where m is the nucleon mass, A is the equivalent number of neutrons in the gas, and σ is the inelastic cross section for n+^{7}Li(0.478) for neutrons in the 1/2 to 15 MeV region.

For ^{32}S+Ag at E/A=22.5 MeV, Fields et al. report an associated PE proton multiplicity of 2.0 for protons in coincidence with Li of momentum, $\langle P_x \rangle$=820 MeV/c. (This momentum most closely resembles the typical momentum of ^{7}Li fragments observed in the E/A=35 MeV data presented here). Based on the similarity between that measurement and the associated PE neutron multiplicity for neutrons in coincidence with ^{7}Li reported here for E/A=35 MeV (1.86 given in Table III.3.1), the charged particle multiplicities reported in Fi86 are probably close to the corresponding multiplicities for this reaction. Under that assumption, then, for this reaction at E/A=35 MeV the number of coincident light fragments is 6, and the total associated PE baryon multiplicity is 10. In calculating the effect of final state interactions, Boal used the significantly larger values of 17.6 and 28.4 for estimates of the number of coincident fragments and the total associated baryon multiplicity at E/A=35 MeV [Bo86b].

As given in the previous chapter, at E/A=20 MeV the associated PE neutron multiplicity is typically 1, half the typical value at E/A=35 MeV. Under the assumption that all associated PE light fragment multiplicities have the same dependence on beam energy, the number of coincident light fragments would be 3, and the total associated PE baryon multiplicity would be 5 for the E/A=20 MeV case.

To obtain the values of 17.6 coincident light fragments and 28.4 coincident baryons, Boal used as his estimates:

$$M_p + M_n = 12.7$$

$$M_d = 1.4$$

$$M_t = 1.1$$

$$M_\alpha = 2.4$$

If σ_p, σ_n, σ_d, σ_t, and σ_α are the inelastic cross sections for scattering p, n, d, t, and α respectively from ^{7}Li(0.478) then

$$M_p\sigma_p+M_n\sigma_n+M_d\sigma_d+M_t\sigma_t+M_\alpha\sigma_\alpha \geqq (M_p+M_n+M_d+M_t+M_\alpha)\sigma_n = 17.6\times\sigma_n \qquad \text{(IV.7)}$$

under the assumption σ_p, σ_d, σ_t, and $\sigma_\alpha \geqq \sigma_n$. (17.6 is the total number of ejectiles associated with a ^{7}Li fragment in the estimate Boal used). Similarly, it seems apparent that when the number of baryons is considered,

$$M_p\sigma_p+M_n\sigma_n+M_d\sigma_d+M_t\sigma_t+M_\alpha\sigma_\alpha \leqq (M_p+M_n+2M_d+3M_t+4M_\alpha)\sigma_n = 28.4\times\sigma_n \qquad \text{(IV.8)}$$

(28.4 is the total number of baryons in the ejectiles associated with a ^{7}Li fragment in the estimate Boal used). So Boal assumes that

$$M_p\sigma_p+M_n\sigma_n+M_d\sigma_d+M_t\sigma_t+M_\alpha\sigma_\alpha = 20\times\sigma_n \qquad \text{(IV.9)}$$

(i.e. A=20 where A is the effective number of coincident neutrons), which relies on σ_p, σ_d, σ_t, and $\sigma_\alpha \geqq \sigma_n$.

Putting in numerical values gives: $\Delta^2 = 2.88\ A^{2/3}$ mb, which implies that

$$\frac{T^*}{T_0} = \left\{ \frac{(2.88\ \mathrm{mb})^2 \pi^4 (7/8)}{(500\ \mathrm{mb})^2} \right\}^{1/3} A^{-2/9} = 0.141\ A^{-2/9}. \qquad \text{(IV.10)}$$

For Boal's assumption of A=20, this gives, $T^* = 0.073 \times T_0$. Then for T_0=8.6, T^*=0.62, and for T_0=40, T^*=2.9, both predictions made by Boal. However, the multiplicities Boal used were estimates and we can now use better values. For E/A=35 MeV,

$$M_p + M_n = 4.0$$
$$M_d = 0.5$$
$$M_t = 0.3$$
$$M_\alpha = 1.2$$

[Fi86, Bl87]. Then, the number of ejectiles is 6 and the number of baryons is 10.7. So $6 \leqq A \leqq 10.7$. Suppose A=8. Then, $T^* = 0.141(8)^{-2/9} \times T_0 = 0.089 \times T_0$, which is not significantly different from the result obtained by Boal. Furthermore, for E/A=20 MeV, the associated multiplicities are reduced by half. This implies that $3 \leqq A \leqq 5.3$. If we choose A=4, then $T^* = 0.10 \times T_0$ which is still not significantly different. In fact, if we have only one coincident ejectile (on average) then, $T^* = 0.14 \times T_0$. For final state interactions to be negligible, $T^*/T_0 \sim 1$ which occurs when $A \approx 1.5 \times 10^{-4}$. This shows that Boal's model of cooling is very insensitive to the associated multiplicities. If the model is correct, significant cooling must always be present. Essentially, these associated multiplicities do not change the conclusions made in Bo84b. However, as suggested in Mo85, Boal's model of the cooling represents a limiting case.

IV.4 Sequential Decay

Charged particle decay measurements in reference B186 show that the bound excited state populations increase slightly with increasing beam energy. This trend is contrary to the sequential decay argument previously put forth to explain the apparent low temperature [Mo85, Ha86]. At lower beam energies, a lower temperature is expected, which corresponds to lower populations of particle-unstable states that can decay to ^{7}Li or ^{7}Be, which will result in less feeding of the ground state. If this feeding were the sole cause of the discrepancy between the excited state production temperature measurements and the kinetic energy slope parameter, its effect would be reduced at lower beam energies, and the result would be higher observed temperatures at lower beam energies. Nevertheless, there is certainly some feeding which occurs, as evidenced by the correlated neutrons, and it is possible to give quantitative estimates of the effects.

In order to determine the extent to which feeding from sequential decay reduces the observed fractions reported in Refs. Mo84, Mo85, and B186, we need to estimate the total feeding from the present measurements of the feeding from a single decay channel. An attempt at this can be made with the quantum-statistical model of Hahn and Stöcker [Ha86]. The calculation assumes an initial statistical equilibrium distribution from infinite nuclear matter which is determined by the binding energy of the isotopes, including the excited state populations (using all known states). Subsequently, the final isotope distributions are calculated using all known decays and their branching ratios. The model assumes the temperature, kT, the break-up density, ρ, and the initial proton to neutron ratio, Z/N, for the system in equilibrium are known. The results are relatively insensitive to the break-up density over the range investigated (10% to 150% normal nuclear matter density, ρ_0). The calculations reported here are all for $\rho=\rho_0/4$. At this density it is plausible to assume nuclear interactions are negligible. In choosing the proton to neutron ratio, we assumed that the system consisted of the 14 beam nucleons, plus 14 target nucleons which form a "hot-spot". Based on the proton to neutron ratios of the constituents, this provides 13 protons and 15 neutrons (Z/N=0.88). The source velocity extracted from moving source fits of the inclusive particle spectra is roughly half the beam velocity, which suggests that this picture is appropriate. The isotope distribution is the most sensitive test of Z/N, and Z/N=13/15 reproduces the Li isotope distribution to within 30 percent for E/A=35 MeV and to within 15 percent for E/A=20 MeV (for kT=3 MeV and $\rho/\rho_0=0.250$). Table IV.4.1 compares the Li isotope distributions calculated for three values of Z/N to the experimental values.

For temperatures above 2 MeV and the other parameters in the ranges specified above, the model predicts a large amount of feeding (from 30 to 70%) to the ground states of the Li and Be isotopes. The feeding is significant in that the predicted fractions of excited state populations for some low-lying particle bound states are brought close to the observed values [Mo84, Mo85, Bl86] (as shown in Table IV.4.2). While the model does not agree with the data in every case, these and similar calculations [Xu86] still suggest that feeding may contribute significantly to the discrepancies in the reported temperatures. The

TABLE IV.4.1 Li isotope distributions.
(Yields normalized such that the ^{7}Li yield equals 1).

	Quantum-Statistical Model Predictions (with kT=3.0 MeV and ρ/ρ_0=0.250)			Experimental[a]	
IMF	Z/N=13/15	Z/N=19/23	Z/N=54/68	E/A=35 MeV	E/A=20 MeV
^{6}Li	0.70	0.50	0.39	0.76(2)	0.708(9)
^{7}Li	1.00	1.00	1.00	1.00	1.00
^{8}Li	0.13	0.18	0.24	0.183(5)	0.151(2)

[a] Experimental values are for a fixed energy range in the lab at 50°.

TABLE IV.4.2 Fraction of fragments in an excited state for several
γ-emitting states.

	Quantum-Statistical Model (with Z/N=13/15 and ρ/ρ_0=0.250)				Experimental[b]	
State	kT=2.0	kT=3.0	kT=4.0	kT=5.0	E/A=35 MeV	E/A=20 MeV
^{6}Li(3.0)	0.044	0.048	0.056	0.065	0.01(2)	unknown
^{7}Li(0.5)	0.228	0.199	0.186	0.183	0.171(24)	0.079(24)
^{8}Li(1.0)	0.271	0.269	0.262	0.255	0.051(47)	unknown
^{7}Be(0.4)	0.273	0.257	0.240	0.230	0.183(29)	0.083(22)

[b] These values from Refs. Mo84, Mo85 and Bl86.

present data provides an independent check of this. Since, for each initial parameter set, the model predicts (among other things) the number of ^{8}Li initially in the 2.255 MeV excited state, ^{7}Li initially in the 7.456 MeV excited state, ^{7}Li in the final distribution, and ^{6}Li in the final distribution, we can readily compare the predicted feeding from specific branches to that observed. Figure IV.4.1 shows the predicted feeding to the ^{7}Li yield from the neutron decay of the 2.255 MeV state in ^{8}Li. (Note, these predictions are not peculiar to Hahn and Stöcker's model, as comparable results are predicted by a microcanonical ensemble model [Fa83]). A comparison of the feeding of 7% observed for a single decay channel for E/A=35 MeV to the calculation shown in Figure IV.4.1, indicates that the temperature should be about 4 MeV. Then with a temperature of 4 MeV (and the other model parameters unchanged) the model predicts that the <u>total</u> feeding to the ^{7}Li yields from all known decays is 55 percent. That is, 55% of the observed ^{7}Li yield is from particle decay of other nuclei. Furthermore, the model predicts significant feeding to the first excited state (26%). The 0.478 MeV excited state to ground state population ratio, R, can be obtained from the observed excited state fraction, f_{ex}, and the observed fraction in any γ-emitting states, f_γ, including feeding to the ground state, F_{gs}, and to the excited state, F_{ex}, from the relation:

$$R = \frac{f_{ex}}{1 - f_\gamma - F_{gs}} \times (1 - F_{ex}). \qquad \text{(IV.11)}$$

Then, the bound excited state fraction of 0.171±0.024 from Ref. Bl86 gives the ratio of the populations of the first excited state to the ground state of ^{7}Li as 0.45±0.11 which (using equation I.1) corresponds

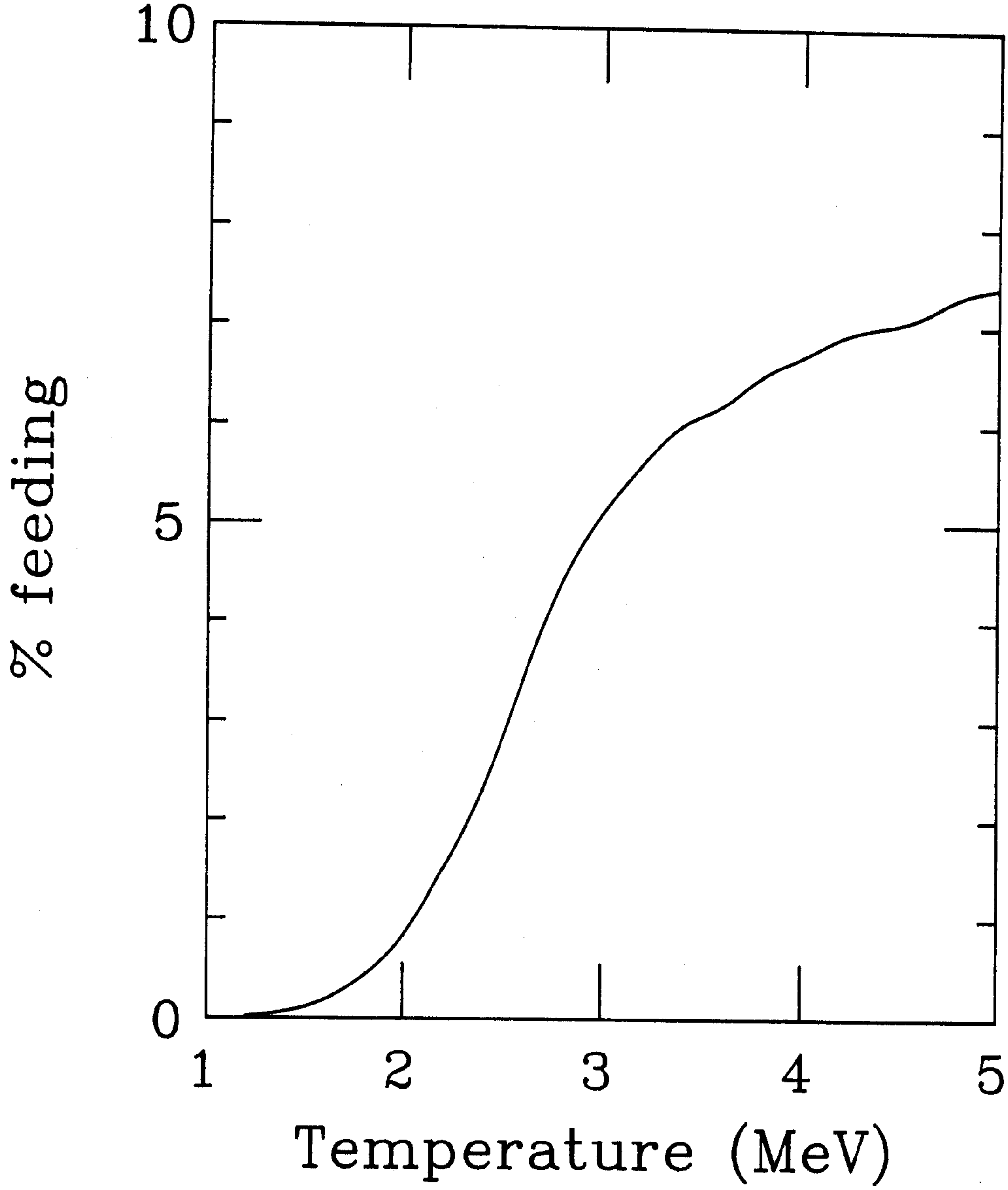

Figure IV.4.1 Feeding to the ^{7}Li ground state via the neutron decay of the 2.255 MeV state of ^{8}Li, as calculated by the quantum statistical model.

to a temperature of $4.5^{+\infty}_{-3.3}$ MeV. Note that both feedings (0.55 to the ground state and 0.26 to the 0.478 MeV state) were used as exact (while they clearly are not). This temperature is then consistent with that obtained by comparing the two excited state populations. Furthermore, the ratio of the populations of the 7.456 MeV state to the ground state in ^{7}Li reported in Table III.3.1 can be corrected for feeding in a similar manner. (The feeding to the 7.456 MeV state of ^{7}Li is negligible at this temperature). In that case, the corrected ratio is 0.15±0.03 which corresponds to a temperature of 3.2±0.3 MeV. Again, no attempt was made to include errors on the feeding values. Similarly, this procedure can be carried out for the E/A=20 MeV data. In that case, the observed feeding from the 2.255 MeV state of ^{8}Li to the ground state of ^{7}Li, 4.4(9) percent, implies a temperature of around 3 MeV when compared to the calculation shown in Figure IV.1.1. At 3 MeV, the quantum statistical model predicts 31% feeding to the ^{7}Li ground state and 16% total feeding to the 0.478 MeV excited state of ^{7}Li. The corrected ratios and their corresponding temperatures for both energies are shown in Table IV.4.3. Considering that there is a large uncertainty in the total feeding, it is reasonable to say that for E/A=35 MeV, all three temperatures obtained from the populations of levels of ^{7}Li and the extent of the feeding to the ^{7}Li yield from the 2.255 MeV state in ^{8}Li provide consistent temperatures. For the E/A=20 MeV, the observed level of feeding indicates a temperature of about 3 MeV; the population of the 7.456 MeV state of ^{7}Li compared to both the ground state and the 0.478 MeV state indicates a temperatures of 2.2 and 3.3 MeV, respectively. Of the ^{7}Li measurements, only the population of the 0.478 MeV state of ^{7}Li relative to the ground state still (after

TABLE IV.4.3 Excited state ratios, R, corrected for feeding via equation IV.11 and their corresponding temperatures, kT, according to equation I.1.

E/A=35 MeV:

States Compared	R (ratio)	kT (from Eq. I.1)
^{7}Li(0.478)[a] to ^{7}Li(g.s.)	0.45(11)	$4.5^{+\infty}_{-3.3}$ MeV
^{7}Li(7.456) to ^{7}Li(g.s.)	0.15(3)	3.2(3) MeV

E/A=20 MeV:

States Compared	R (ratio)	kT (from Eq. I.1)
^{7}Li(0.478)[a] to ^{7}Li(g.s.)	0.11(4)	$0.32^{+0.08}_{-0.07}$ MeV
^{7}Li(7.456) to ^{7}Li(g.s.)	0.047(12)	2.2(2) MeV

[a] Population of γ-emitting state from Ref. B186.

corrections for feeding) indicates a low temperature (kT<0.5 MeV). Considering how rapidly the predicted feeding changes as a function of temperature in this region and the large uncertainties in the corrections, it is possible that this discrepancy is due to an error in estimating the effects of the feeding.

CHAPTER V: SUMMARY AND CONCLUSIONS

V.1 Summary

Kinetic energy spectra were obtained for neutrons in coincidence with intermediate mass fragments observed at 50°, 70°, and 90° in the lab from the reaction of ^{14}N+Ag at both E/A=35 MeV and E/A=20 MeV. While there have been numerous previous neutron coincidence experiments [Hi79, Ga83, Ho83, Hi84a, Ca85, Ca86, De86a, De86b, Ho86, Re86], these were limited to measuring neutrons in coincidence with either projectile-like fragments, fission fragments, or evaporation residues. The present measurement represents the first time that neutrons have been measured in coincidence with intermediate-mass fragments observed at large angles.

These neutron kinetic energy spectra were fit with a two-source moving source model [Ja83]. This model provided an excellent parameterization of the data in terms an associated multiplicity, an effective temperature parameter, and a source velocity for both a target residue source and a pre-equilibrium source. The associated neutron multiplicities for neutrons in coincidence with ^{6}Li, ^{7}Li, ^{8}Li, ^{7}Be, ^{9}Be, ^{10}Be, ^{10}B, and ^{11}B fragments are reported in Tables III.3.1 and III.3.2. For E/A=35 MeV, the target residue multiplicity is typically 6 to 7 (depending primarily on the type of fragment with which the neutrons were in coincidence) while the PE multiplicity is about 2. For the E/A=20 MeV data these values are 4 to 5 and 1, respectively. No dependence is seen on fragment angle for angles greater than θ=50°. No preference is seen for the neutrons to be emitted either on the same side or on the opposite side of the beam as the observed fragment. An out-of-plane anisotropy is observed. It is approximately 20% for the target residue source and about 50% for the PE source. The measured multiplicities are used to replace estimates used by Boal [Bo84b] to determine the effect of final state interactions on bound excited state population measurements. While the observed multiplicities are significantly different than those estimates, the model is fairly insensitive to these values in this region, and the correction to its effects are negligible.

A physically significant interpretation of the source velocities and effective temperature parameters can be made. For the target residue source, the velocities are 65% and 80% of the center of mass velocity for E/A=35 MeV and E/A=20 MeV, respectively. The corresponding effective temperature parameters (from the fits) are 3 and 2.5 MeV. These values are typical of what would be expected for incomplete fusion. For the PE source, the velocities are approximately 35% of the beam velocity for both beam energies. The corresponding effective temperature parameters are approximately 12 and 10 MeV. These values are are similar to values obtained for particle inclusive measurements of fragments from Z=1 to Z=7.

Finally, by integrating the moving source model's analytic expression for the neutron spectra over solid angle an expression for the neutron energy distribution, $\frac{d\sigma}{dE}$, is obtained. With the above moving source fit parameters, this energy distribution is then readily compared to predictions made by a Harp-Miller-Berne Exciton Model as modified for heavy ion induced reactions by Blann [Bl81]. Reasonable agreement is obtained for exciton number, n_0, equal to either the number of beam nucleons, A_p, or for $n_0=A_p+3$. The agreement is both in the shape of the energy distribution (i.e. its energy dependence) and in the overall normalization (i.e. associated multiplicity). This is in contrast to several similar works [Ga81, Aw82, Ho83, Ho86].

In addition to measurement of the associated neutron multiplicities, quantitative observations were made of several particle unbound excited states in the intermediate mass fragments using a technique developed by Kiss et al. [Ki87]. Specifically, the neutron decays of the 7.456 MeV excited state of ^{7}Li, the 2.255 MeV excited state of ^{8}Li, the 7.371 MeV excited state of ^{10}Be, the 3.89 MeV excited state of ^{11}Be, and the 3.388 MeV excited state of ^{12}B were observed. These observations were used to determine the population of the excited state relative to the ground state and any existing bound excited state population measurements, where possible. By assuming a Boltzmann distribution of excited state populations, these measurements were used to obtain temperatures. Neglecting the effects of sequential decay on such measurements [Mo85, Ha86], the extracted temperatures were around 2 or 3 MeV. Finally, while quantitative results were not possible, it appears the decay of the 1.69 MeV excited state of ^{9}Be has been observed.

In addition to interpreting the unbound excited state population measurements in terms of temperature, they are also measurements of feeding due to sequential decay. This mechanism is considered to significantly alter the observed population ratios, especially for ratios involving the ground state or states of small excitation energy [Mo85, Ha86, Xu86]. This thesis reports the measured extent of feeding from sequential decay for a system previously used in a bound state temperature measurement [B186]. This was done via a measurement of the neutron decay of the 2.255 MeV excited states of ^{8}Li nuclei observed from the reaction of ^{14}N+Ag at E/A=20 and 35 MeV. This decay feeds the ground state of ^{7}Li by 7% for E/A=35 MeV and by 4% for E/A=20 MeV. These measured feedings were compared to predictions made by Hahn and Stocker's Quantum Statistical Model [Ha86]. Quantum-statistical calculations predict that the 2.255 MeV state of ^{8}Li will account for 10 to 20% of the total feeding to the ground state of ^{7}Li. The observed degree of feeding via that channel (7% and 4%) clearly indicates that sequential decay can significantly alter the observed population of states, particularly that of the ground state. The results are used to estimate the temperature (4 and 3 MeV are the predictions for the two beam energies) and to estimate the total feeding to the ^{7}Li ground state (55% and 31%, based on the estimated temperatures) to correct the excited state population temperature measurements. In most cases, the corrected excited state population measurements are significantly higher (than the uncorrected version) and are all somewhat self consistent. The resulting temperatures are also consistent with charged-particle correlation measurements [Po85a, Ch86a]. In this way, some of the originally observed discrepancies are explained.

In order to compare ^{7}Li excited state production to that of the ground state, the ^{7}Li energy spectrum is corrected for contamination by pairs of α particles from the ground state decay of ^{8}Be [B186]. This correction is based on a previous measurement for the same reaction (at

E/A=35 MeV). For the E/A=35 MeV data, the contamination is about 20%, while it is about 13% for the E/A=20 MeV data.

V.2 Conclusions

An important component of heavy ion reactions in this energy region (10 MeV $\leq$ E/A $\leq$ 100 MeV) has been the observation of intermediate mass fragments ($4<A<A_{beam}$) at large angles in the lab ($\theta \gg \theta_{grazing}$) [Me80, We82, We84, Wo85, Fi86]. Since this is the first measurement of neutrons in coincidence with fragments of this type, many interesting conclusions can be drawn.

A logical comparison to make is between the results presented here and those from neutrons in coincidence with IMF's at forward angles (projectile-like fragments). In Re86, a definite increase in the observed target residue associated neutron multiplicities is seen as a function of IMF angle. The lack of dependence on fragment angle in the data presented here indicates that for any given angle, the events represent a range of impact parameters. As the fragment angle is increased, this range is biased towards more violent collisions, up to a maximum angle. After that point, it appears the collisions are all characterized by fairly central collisions (giving rise to the highest average associated multiplicities). Generally, the observed multiplicities are also consistent with those seen from neutrons in coincidence with evaporation residues for similar reactions [Ho83, Ho86].

The moving source model is generally successful at describing the energy spectra of fragments emitted from such reactions. The present data are no exception, with excellent fits to the in-plane data provided by a two source description. However, in that model the thermal assumption implies that the emission is isotropic in the rest frame. In that sense, the model is in direct conflict with the observed data. The measured out-of-plane anisotropy proves the emission in not isotropic. For that reason, one should be very wary of interpreting the source parameters (particularly the source velocity and the effective temperature parameter). As shown by Chitwood et al., the observed parameters can vary significantly if similar models with different assumptions are adopted [Ch86b]. For this particular case, a preferred plane of emission is probably due the angular momentum of the system. Certainly a relatively low energy intermediate mass fragment does not determine the reaction plane as well as a fragment of larger mass and of relatively high energy (observed at a large angle). The implication of this is that the observed anisotropy is a lower limit. It is likely that the coincident fragments were not as effective in determining the reaction plane as evaporation residues could be.

For this data, the HMB exciton model also provided a good description. Essentially, this model makes several assumptions about the physics of the problem, and then makes predictions without any adjustable parameters. If the predictions match the data well, one would hope to be able to conclude that the physical approximations are fairly reasonable. However, recently attempted applications of the basic model have been somewhat unsuccessful [Ga81, Aw82, Ho83, Ho86]. In order to explore the possibilities, adjustments in the parameters have been introduced [Aw82, Ho83, Ho86]. These include letting the exciton number be a free parameter, generally energy dependent, adjusting the intra-nuclear transition rates, and including arbitrary overall normalizations to the cross section. While these may aid in describing the data, it is not clear that any conclusions can then be made regarding the physics. Finally, it is possible that such adjustments may not be necessary. It may be that agreement with the data is actually being accomplished with offsetting adjustments. This is suggest by Blann [Bl85] as the explanation for the result obtained by Holub et al. [Ho83]. In particular, large values of n_0 can be offset by arbitrary normalizations of the cross section combined with different intra-nuclear transition rates. However, such a cancellation of errors is more easily obtained when observing only the PE contribution to the neutron spectrum. By including the neutrons from both sources, the problem becomes more constrained. The agreement obtained here with the HMB model is both for the spectrum shape and the multiplicity. Furthermore, the model predicts the time development of the neutron spectrum.

One application of the associated neutron multiplicities is in calculating the effects of final state interactions on bound excited state population measurements. Boal made such a calculation using a relatively simple model [Bo84b] and estimated associated fragment multiplicities. The measurement of these associated PE neutron multiplicities combined with measurements of the associated PE multiplicities for light charged particles for similar reactions [Fi86] allowed Boal's calculation to be redone with more accurate estimates of the necessary parameters. The model is very insensitive to the multiplicities in this region, however, and the results are little changed. Basically, Boal was able to conclude that final state interactions could lower the observed temperatures by an order of magnitude from the emission temperature. Based on the model he used, this result remains. However, as pointed out in Mo85, that model of cooling is one limiting case. In their work, Morrissey et al. also present a model at the opposite limit (predicting the minimum cooling instead of the maximum). Now that reasonable estimates of the associated multiplicities are available a more sophisticated model would be very useful.

The second type of result presented here are excited state population measurements. These can be interpreted as a nuclear temperature under the assumption that the distribution of nuclei in their various quantum states is given by a Boltzmann distribution. At this point, the temperatures obtained have no significance. Previous measurements of this type [Mo84, Mo85, Po85b, Bl86, Ch86a, So86, Xu86] have yielded inconsistent results, both with each other and with respect to the observed particle inclusive slope parameters from moving source fits. Currently, significant effort is being spent in an attempt to reconcile the various temperature measurements. With a limited amount of data the possibility exists that more than one solution would appear feasible. By expanding the data base, it may be possible to determine a unique solution. Quantitatively, the observed temperatures agree with the trends observed to date. Temperatures extracted from measurements of unbound excited state populations are consistently higher (3 to 5 MeV) than those extracted for bound excited state population measurements (~0.5 MeV). Furthermore, population ratios not involving the ground state and ones involving a state with a very high excitation energy give higher temperatures than ratios not in these categories. The present results adhere to these trends.

Generally, the largest uncertainty in the above population measurements (and hence the extracted temperatures) is in determining the absolute geometric efficiency of the system. In this work, the efficiencies were calculated based on the measured geometry. Under the best circumstances this technique will always be subject to large uncertainties. Ideally it would be best to measure directly the geometric efficiency during the experiment. A technique to do this would greatly reduce the uncertainty of the measurement.

Finally, one of the most significant results reported here is the measurement of the feeding from sequential decay, for several specific channels. For most of the feedings listed in Table III.3.5, no corresponding temperature measurement exists. The exception is for the neutron decay of the 2.255 MeV excited state in ^{8}Li to the ground state of ^{7}Li. A significant portion of the observed ^{7}Li yield comes from this one branch. This is absolute proof that feeding from sequential decay plays a major role in the observed population ratios (at least in some cases). By requiring the predictions made by the quantum statistical model [Ha86] to match the feeding from this one branch (by adjusting the model parameters), the temperatures based on ^{7}Li populations can be corrected for feeding from sequential decay from all known branches. Generally, this proved successful. For the E/A=35 MeV data, the corrected temperatures are reasonably consistent. The results are not as good for the E/A=20 MeV data, but there are several possible explanations. For one, the temperatures are very sensitive to the feeding corrections. A change by a factor of two in the feeding can result in a temperature change of over an order of magnitude. Secondly, there are large uncertainties in the data which make accurate predictions difficult. It should be remembered that the corrected temperatures and their uncertainties given in Table IV.4.3 do not include any uncertainty in the model predictions. Reasonable estimates of those uncertainties would lead to completely undetermined temperatures. The quantum statistical model itself is certainly only an approximation in this energy region. The model was intended to make predictions at much higher temperatures (where the energy per nucleon is well beyond the binding energy per nucleon). Considering these limitations, the results obtained are quite consistent.

For the other isotopes for which bound state population measurements exist (^{6}Li, ^{8}Li, and ^{7}Be) such a complete picture does not exist. The only other measurement of feeding from sequential decay is from the 7.456 MeV state of ^{7}Li to the ground state of ^{6}Li. While the excited state fraction predicted by the quantum-statistical model (which includes the effect of feeding from sequential decay) for any temperature from 1 to 5 MeV is larger than that observed, there are considerable uncertainties in both the measurement and the model predictions. In particular, the model has not yielded particularly good predictions for the isotope distributions (at least for the parameter ranges consider in this paper), and there is considerable debate about the proper value of the density parameter. In light of the sucess in describing the ^{7}Li system, it is possible that the excited state populations of other systems will also be understood in terms of temperature as more data becomes available. At this point, the validity of the temperature assumptions in this area is far from settled. Hopefully, the additional unique data reported here will help facilitate such a determination.

APPENDIX A: ^{8}BE CONTAMINATION OF ^{7}LI SPECTRA

Recently reported measurements of the production of excited states of ^{7}Li and ^{7}Be nuclei emitted at large angles from the reaction of ^{14}N+Ag at E/A=35 MeV [Mo84, Mo85] indicated a slight discrepancy (about 2 standard deviations) between the temperatures determined from the excited state populations of these two nuclei. The fraction of the population of the ^{7}Li excited state indicated a temperature of 340±50 keV while the same measurement for ^{7}Be nuclei indicated 530±150 keV. Very similar results are expected for these two mirror nuclei since they are a mirror pair. However, this discrepancy was ignored then; the interesting fact was that they both indicated temperatures much lower than the 10 to 12 MeV expected. In a subsequent experiment [Mo86], the cause of this 2 standard deviation discrepancy became a much more important discrepancy.

Initial analysis (unpublished) of the data obtained by Morrissey et al. indicated that for 112 MeV ^{14}N on C, the excited state fraction for ^{7}Be was roughly five times greater than that for ^{7}Li. In Mo86, the authors explain that this prevented them from including results based on ^{7}Li observations. The clue to solving this huge discrepancy was found in the ^{7}Li coincident γ-ray spectrum, shown in Figure A.1.1. In addition to the peak at 478 keV corresponding to the first excited state of ^{7}Li is a peak at 718 keV, which happens to be the first excited state of ^{10}B. For the reaction of 112 MeV ^{14}N on C, the reaction partner of

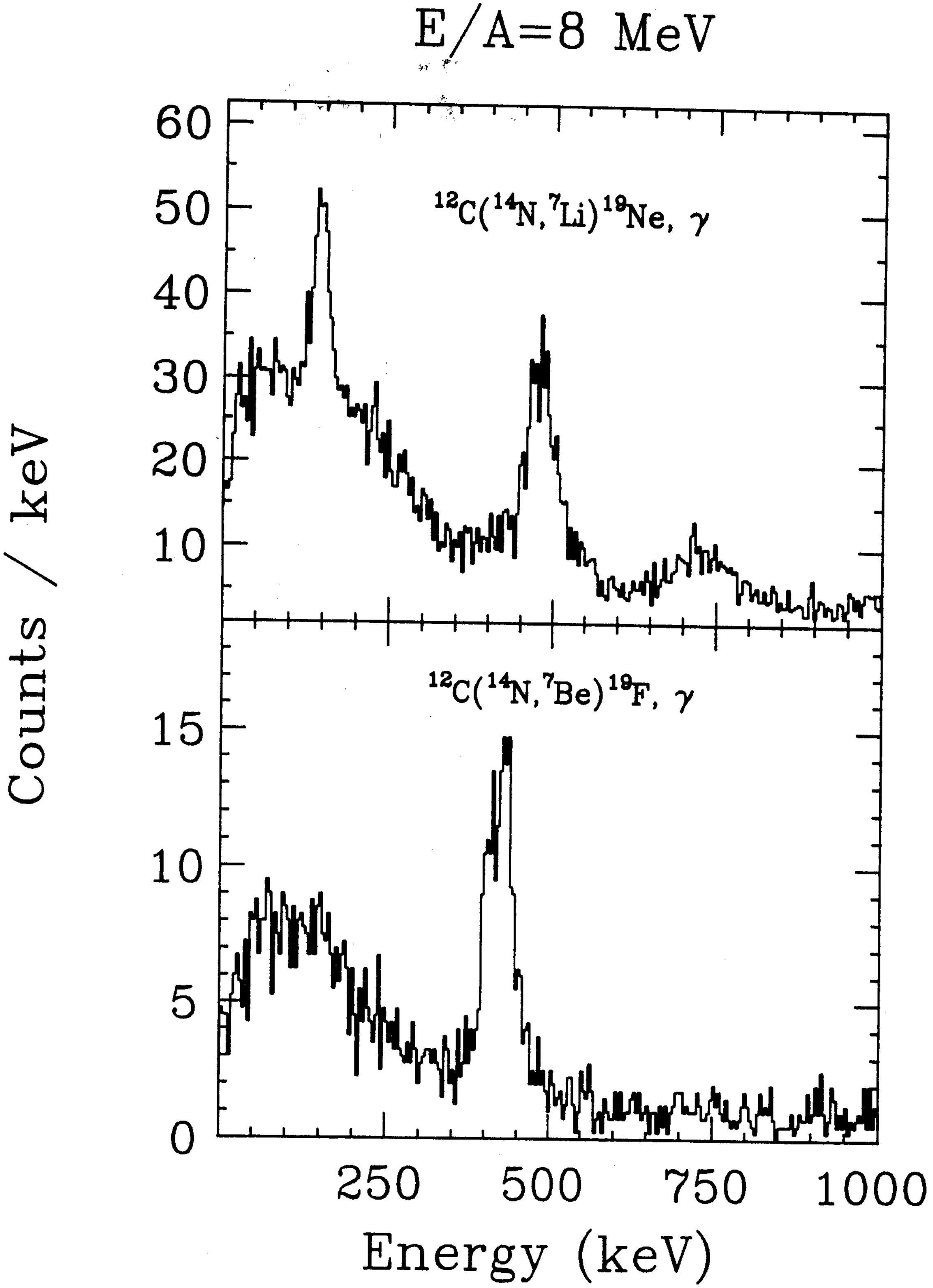

Figure A.1.1 γ rays in coincidence with fragments identified as ^{7}Li and ^{7}Be from ^{14}N+C at E=112 MeV.

^{7}Li is ^{19}Ne which has no such γ ray in its decay chain. Conversely, the reaction partner for ^{10}B should be ^{16}O. Indeed, what was thought to be ^{7}Li sometimes was actually a misidentified product from the decay of ^{16}O which was in coincidence with ^{10}B and hence the γ ray from ^{10}B. (The spectrum of γ rays in coincidence with ^{7}Be is shown in Figure A.1.1 for comparison).

In most cases, the identification of an isotope in a ΔE-E silicon telescope is unambiguous. However, this is not true for ^{7}Li. In the previous measurements [Mo84, Mo85], the ^{7}Li spectra included misidentified ^{8}Be decay products. Ground state ^{8}Be nuclei decay into pairs of alpha particles with a Q value of 92 keV. This low relative energy between the α particles (compared to typical ^{8}Be kinetic energies of 30 MeV) means that they will continue along trajectories almost identical to that of the initial ^{8}Be. There is, therefore, a high probability that both α particles from a ^{8}Be fragment will be detected in a single silicon telescope [Wo72]. As discussed in B186, when both of the α particles pass through a silicon detector, they produce a specific ionization approximately 2% different from that of a ^{7}Li fragment, which is much less than the spread in the ΔE signal due to straggling. In the reaction of $^{14}N+^{12}C \rightarrow ^{10}B+^{16}O$, it is very likely that the excited ^{16}O nuclei will break up into either two ^{8}Be or $^{12}C+\alpha$. In this latter case, the ^{12}C can then break up into $^{8}Be+\alpha$. So in each case, the ^{16}O provides a source of ^{8}Be which will decay into α pairs which are easily mistaken for ^{7}Li. This explains how ^{10}B γ-rays are in coincidence with fragments identified as ^{7}Li from the reaction ^{14}N+C. Also, the propensity for that reaction to give $^{10}B+^{16}O$ as opposed to

^{7}Li+^{19}Ne was responsible for the fact that α pairs overwhelmed ^{7}Li by roughly 4 to 1 in the ^{7}Li particle identification gate.

Clearly any ^{8}Be fragments which are identified as ^{7}Li increase the denominator of the fraction and thus reduce the inferred temperature. In the reaction of 112 MeV ^{14}N on C, 70-90% of the particles identified as ^{7}Li were actually α pairs from ^{8}Be decay. (This result depends on the solid angle of the silicon detectors. The results given here are for a 25 msr detector). The size of the contamination in that particular system made it impossible to determine accurately the number of ^{7}Li particles. However, the ^{8}Be to ^{7}Li ratio is not so great in the reaction of ^{14}N+Ag at E/A=35 MeV. In B186, measurements of the yields of ^{6}Li, ^{7}Li, and ^{9}Be fragments from the reaction of E/A=35 MeV ^{14}N+Ag as a function of detector solid angle allowed a determination of the extent of the contamination of the ^{7}Li spectrum by ^{8}Be decay. In that case, only 33% of the events identified as ^{7}Li were actually α pairs, and it was possible to correct the measured excited state fraction and the resulting temperature. The corrected values gave excellent agreement between the temperatures extracted from ^{7}Li and ^{7}Be.

Part of the experiment described in B186 determined what portion of the particles identified as ^{7}Li was actually α pairs from ^{8}Be decays for the reaction ^{14}N+Ag at E/A=35 MeV. The extent of such a contamination was determined by varying the solid angle of the silicon detectors, since the yield of ^{7}Li fragments detected is linearly proportional to the solid angle while the yield of α pairs from ^{8}Be decay is not. This difference is due to the fact that the alpha particles are emitted within a cone of finite opening angle along the ^{8}Be trajectory, and therefore both particles will not always enter the detector. The observed ^{7}Li differential cross section is then the sum of the true ^{7}Li differential cross section plus a solid-angle-dependent differential cross section of α pairs. This is represented by the equation:

$$\int \frac{d^2\sigma}{dEd\Omega}(^7\mathrm{Li}_{\mathrm{obs}}) \times dE = \int \frac{d^2\sigma}{dEd\Omega}(^7\mathrm{Li}) \times dE + \int \frac{d^2\sigma}{dEd\Omega}(\alpha+\alpha) \times dE, \qquad (A.1)$$

where the double-differential cross sections are of the products in parenthesis, $^7\mathrm{Li}_{\mathrm{obs}}$ represents any particle which identifies as a ^{7}Li, and $\alpha+\alpha$ is a coincidence of two α particles in one detector. $\frac{d^2\sigma}{dEd\Omega}(\alpha+\alpha)$ has an implicit dependence on solid angle, $\Delta\Omega$, from the dependence of the relative efficiency for detecting both α particles in the single detector. This is generally less than one, due to the fact that the alpha particles have a finite opening angle. This relative efficiency, $\varepsilon_{\Delta\Omega}(E)$, is a function of the original ^{8}Be energy, E, and the solid angle of the detector [Me74]. For a given $\Delta\Omega$, E, and Θ, the angle between the original ^{8}Be trajectory and the detector axis, a Monte Carlo calculation was used to determine the probability, $P_{\Delta\Omega}(E,\Theta)$, that both alpha particles, emitted isotropically in the moving ^{8}Be frame, would enter the detector. Then, $\varepsilon_{\Delta\Omega}(E)$ is given by the following integration:

$$\varepsilon_{\Delta\Omega}(E) = \frac{2\pi}{\Delta\Omega} \times \int_0^{\Theta_0} P_{\Delta\Omega}(E,\Theta) \times \sin(\Theta) \times d\Theta, \qquad (A.2)$$

which was computed numerically (see the Fortran code at the end of this appendix), where Θ_0 is the half angle of a detector with solid angle $\Delta\Omega$, given by:

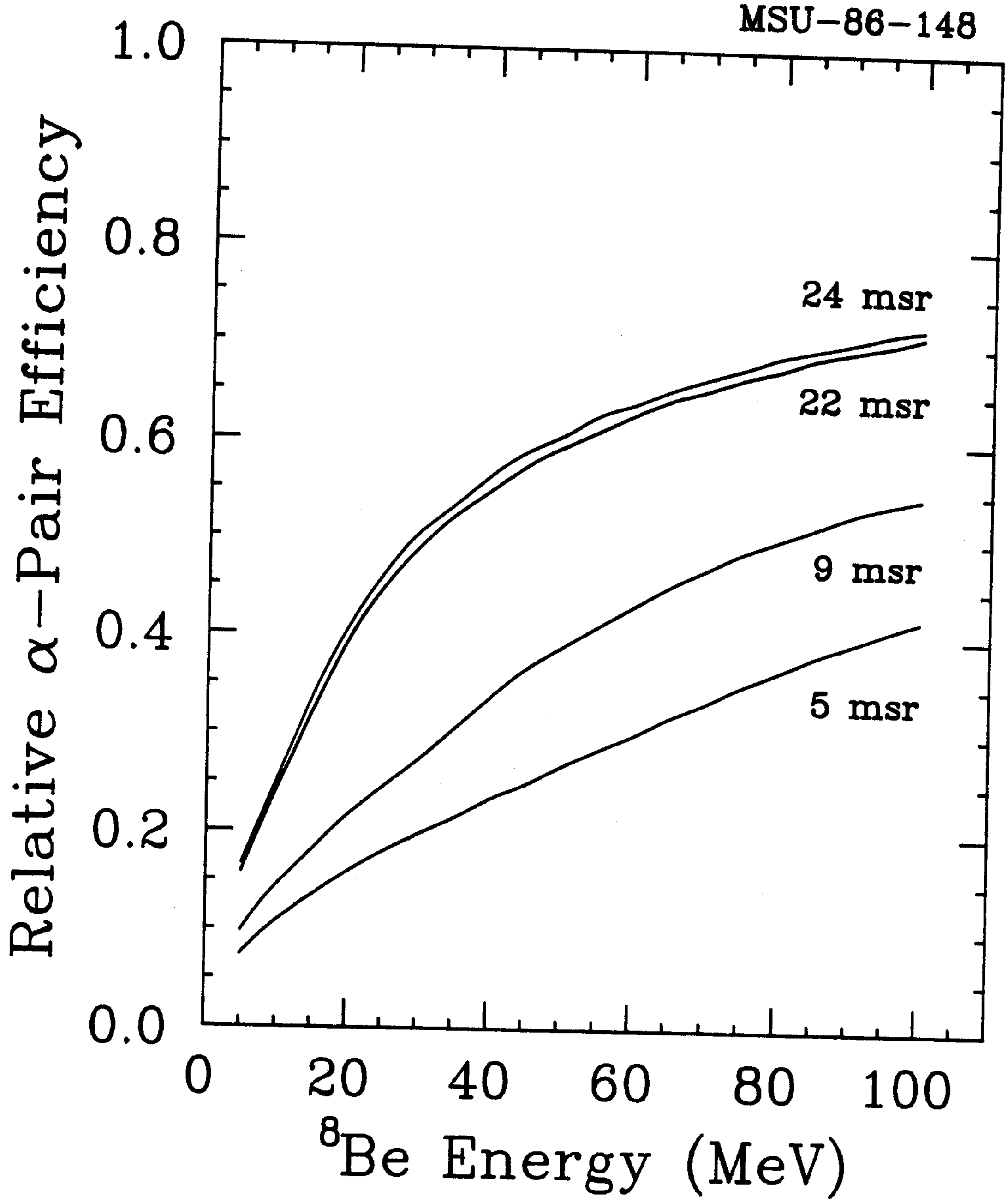

Figure A.1.2 $\varepsilon_{\Delta\Omega}(E)$ for $\Delta\Omega$=5, 9, 22, and 24 msr.

$$\Theta_0 = \cos^{-1}(1 - \frac{\Delta\Omega}{2\pi}). \qquad (A.3)$$

The results of such a calculation for the solid angles used in the present measurement are shown in Figure A.1.2. Since $\varepsilon_{\Delta\Omega}(E)$ is the relative efficiency for detecting both α particles from a ^{8}Be decay, i.e. the probability of detecting both α particles given the initial ^{8}Be trajectory was within the detector's angular acceptance,

$$\frac{d^2\sigma}{dEd\Omega}(\alpha+\alpha) = \frac{d^2\sigma}{dEd\Omega}(^8\mathrm{Be}) \times \varepsilon_{\Delta\Omega}(E) \qquad (A.4)$$

must hold and can be inserted into equation A.1. By assuming the shape of the ^{7}Li and ^{8}Be spectrum with arbitrary normalizations m and b respectively the resulting equation can be integrated over an appropriate energy range to yield

$$U = m \times V + b \times W, \qquad (A.5)$$

where

$$U = \int\frac{d^2\sigma}{dEd\Omega}(^7\mathrm{Li}_{obs}) \times dE, \qquad V = \frac{1}{m} \times \int\frac{d^2\sigma}{dEd\Omega}(^7\mathrm{Li}) \times dE, \qquad (A.6a,b)$$

and

$$W = \frac{1}{b} \times \int\frac{d^2\sigma}{dEd\Omega}(^8\mathrm{Be}) \times \varepsilon_{\Delta\Omega}(E) \times dE, \qquad (A.6c)$$

all of which are known. (U is a measured quantity, V and W are calculated). At this point, U and W depend on $\Delta\Omega$. Dividing equation A.5 by W gives:

$$Y = m \times X + b, \qquad (A.7)$$

where Y=U/W and X=V/W both depend on $\Delta\Omega$ but are known quantities for any $\Delta\Omega$ (assuming U is measured for each $\Delta\Omega$). Then by determining X and Y for more than one $\Delta\Omega$, a linear fit will give m and b. Since m is the magnitude of the ^{7}Li cross section, and the shape of the spectrum is assumed, the true ^{7}Li spectrum is determined and can be compared to the observed ^{7}Li spectrum to determine to what extent the observed spectrum is contaminated by the decay of ^{8}Be.

In B186, the shape of the ^{8}Be kinetic energy spectrum was assumed to be given by a Coulomb-shifted Maxwell-Boltzmann function fit to the ^{9}Be spectrum. Similarly, the shape of the true ^{7}Li spectrum (with no contamination from α pairs) was assumed to be given by the shape of the ^{6}Li spectrum. Then, the values given in that paper for b and m are relative normalizations between ^{8}Be and ^{9}Be and between ^{7}Li (the true spectrum) and ^{6}Li, respectively. Strictly speaking, they are only valid for that reaction (^{14}N+Ag at E/A=35 MeV) and for the kinetic energy range observed. Particle singles data as a function of detector solid angle was not obtained for beam energies other than E/A=35 MeV, and therefore a definite measurement of the level of the α-pair contamination of the ^{7}Li particles does not exist for this reaction at E/A=20 MeV. On the assumption that the mechanism for producing these fragments does not change drastically over this energy range, and since in this work the observed energy ranges are very similar (the ΔE and E elements of the silicon detectors are nearly the same thicknesses), the same values for m and b (m=1.22±0.10 and b=2.1±0.5) will be used. (In B186, the data for ^{14}N+Ag at energies of E/A=20 and 25 MeV were consistent with the same solid angle dependence of the relative yields at E/A=35 MeV, which indicates that it is reasonable to assume that the α-pair contamination is not a strong function of beam energy). Therefore, the true ^{7}Li yield is "m" times the ^{6}Li yield, as given by

$$Y(^{7}\mathrm{Li}) = m \times Y(^{6}\mathrm{Li}), \tag{A.8}$$

where Y(^{6}Li) is the yield of ^{6}Li, integrated ever the energy range of the ^{7}Li fragments with which the observed neutrons were in coincidence. Comparison of 1.22 times the ^{6}Li spectrum to the observed ^{7}Li spectrum indicates that the latter include a contamination from ^{8}Be decay of 20(2) percent for E/A=35 MeV and 13(1) percent for E/A=20 MeV. So, everywhere in this thesis that excited state ^{7}Li yields are compared to total ^{7}Li yields, which are identified only by silicon telescopes, the observed yield is reduced by multiplying by either 80(2) or 87(1) percent (depending on the beam energy). Ground state ^{7}Li yields, are obtained by subtracting excited state yields from the corrected total yield.

There is one instance where the ^{7}Li yield is not corrected. In determining the associated neutron multiplicity for neutrons in coincidence with ^{7}Li, the uncorrected ^{7}Li yield (including α pairs from the decay of ^{8}Be) is used. Presumably ^{8}Be has a comparable associated neutron multiplicity, and there is no way to discriminate (in general) neutrons in coincidence with ^{8}Be from those in coincidence with ^{7}Li. So the associated multiplicities given for ^{7}Li are actually a weighted average of the associated multiplicities for ^{7}Li and ^{8}Be.

There is one final instance where the misidentification of α pairs from the decay of ^{8}Be complicates the data. In the relative velocity histograms of neutrons in coincidence with ^{7}Li (see section 4.4) there is a strong possibility for contamination. ^{9}Be can decay via neutron emission. In that case, the neutron will be emitted with a very small velocity relative to the remaining ^{8}Be. The ^{8}Be will be in its ground state and decay to a pair of α particles, which will appear to be a ^{7}Li in the silicon detectors. Thus the decay of the first excited state of ^{9}Be will appear to be a ^{7}Li in coincidence with a neutron at low relative velocity. This will be confused with the decay of the third excited state of ^{8}Li, which is identified by a ^{7}Li in coincidence with a neutron at low relative velocity. As of yet, there is no measurement to indicate to what extent this contamination takes place. For that reason, the error this misidentification causes (overestimation of the population of the third excited state of ^{8}Li) remains uncorrected.

The following program was used to calculate $\varepsilon_{\Delta\Omega}(E)$:

```
      PROGRAM BE8_MONTE

C     This MONTE-CARLOS the efficiency for detecting a pair of alpha
C     particles if a 8Be was heading into a detector.

      CHARACTER FNAME*12
      FNAME='MSR00.DAT'
      S=SECNDS(0.)
      III=INT(S)
```

```
      pi=3.1415926        !π
      Q = .0919           !Q-value for ⁸Be decay
      DV = SQRT(Q)

      TYPE *,' ENTER THE SOLID ANGLE IN MSR.'
      ACCEPT *,S_ANGLE

      ENCODE (2,1003,FNAME(4:5)) NINT(S_ANGLE)
      OPEN (UNIT=11,FILE=FNAME,STATUS='NEW')
      TYPE *,' The output will be in a file named:',fname

      s_angle=s_angle/1000.        !converts to steradians
      THETA_MAX=acosd(1.-s_angle/(2.*pi)) !half angle
      delta=THETA_MAX/100.         !angle integration step size.

C  Select Be-8 energy...
   Do 199 i_energy=0,19
      energy=5.+5.*real(i_energy)
      V=SQRT(ENERGY)

C  Select Be-8 direction...
      Do 150 jtheta=0,99
        theta=delta/2.+delta*real(jtheta)

C  Weight is the fraction of the total "IN" Be-8's that are in this
C  direction (less factor of 2*pi/s_angle, added later).

        weight=cosd(theta-delta/2.)-cosd(theta+delta/2.)
        arg=SQRT(ENERGY/Q)*sind(theta_max-theta)

        if (arg.GE.1.) then
          PERCENT=1.
        ELSE
          DO I=1,1000    !Monte-Carlo over alpha directions
            theta_a=90.*RAN(III)
            phi_a  =180.*RAN(III)
            dx=dv*cosd(theta_a)*sind(phi_a)
            dy=dv*sind(theta_a)*sind(phi_a)
            dz=dv*cosd(phi_a)

            x = v*sind(theta) + dx
            y = dy
            z = v*cosd(theta) + dz

            rho = sqrt(x*x + y*y)
            rho_max = z*tand(theta_max)

            if(rho.le.rho_max) then                   !one alpha in...

              x = v*sind(theta) - dx
              y = -dy
              z = v*cosd(theta) - dz
```

```
              rho = sqrt(x*x + y*y)
              rho_max = z*tand(theta_max)

              if(rho.le.rho_max) then                  ! BOTH ALPHAS IN !
                 COUNT=COUNT+1.
               ENDIF
             ENDIF
           ENDDO

           PERCENT=COUNT/1000.
           COUNT=0.

         endif

         probability=probability+weight*percent

150    percent=0.

       probability=2.*pi*probability/s_angle
       write(11,1001)energy,probability

199    percent=0.
       CLOSE (11)

1001  format(2f)
1003  format(I2)

      stop
      end
```

APPENDIX B: CALCULATION OF RELATIVE VELOCITY GEOMETRIC EFFICIENCIES

The number of neutrons observed from the decay of the 7.456 MeV state of ^{7}Li observed in coincidence with ^{6}Li depends on three quantities: the population of the state in question, the geometric efficiency for observing such coincidences, and the neutron detector efficiency. We have measured the number of such neutrons for the decay of several excited nuclei, and wish to deduce the population of the states in question. This is possible by calculation of the two efficiencies mentioned. The neutron detector efficiency has been calculated, as discussed in section III.1. This quantity gives the probability that a neutron which enters the neutron detector will produce a signal larger than the threshold set. For a given detector, this efficiency is a function of the threshold and the neutron kinetic energy. The purpose of this appendix is to discuss the geometric efficiency mentioned.

The geometric efficiency is the probability that if the fragment from such a decay enters the silicon detector, the neutron enters the neutron detector, regardless of the signal produced. This efficiency accounts for the geometric and kinematic effects of the decay. The geometric factors include the solid angle of both the silicon detector and the neutron detector, and their positions relative to one another. The kinematic considerations include the velocity or kinetic energy of the original fragment (before decay), the decay energy in that frame (i.e. the Q value), and the relative masses of the two decay products (the neutron and the remaining fragment). This geometric efficiency, $\varepsilon(E,Q,m,M,\Delta\Omega_1,\Delta\Omega_2,\Delta\theta)$, is then a function of the original fragment energy, E, the Q value, Q, the neutron mass, m, the mass of the remaining fragment, M, the solid angle of the silicon detector $\Delta\Omega_1$, the solid angle of the neutron detector, $\Delta\Omega_2$, and the angle between the axes of the two detectors, $\Delta\theta$. The calculation of this geometric efficiency is actually a generalization of the problem discussed in Appendix A. In that case, the efficiency was for detecting both α particles from the ground state decay of ^{8}Be. Since both fragments were observed in the same detector, $\Delta\Omega_1=\Delta\Omega_2$, and $\Delta\theta=0$. Also, the Q value was fixed at 92 keV and the two masses were constant and identical. Then, $\varepsilon(E,Q,m,M,\Delta\Omega_1,\Delta\Omega_2,\Delta\theta)$ could be written as $\varepsilon_{\Delta\Omega}(E)$. A more general code was written to allow for different Q values, different masses, two different solid angles, and a finite angle between the two detector axes. The calculation, however, basically remained unchanged. There is a subtle difference in what efficiency was being calculated. In the case of the ^{8}Be decay, particle inclusive measurements were being studied. The efficiency there gave the probability that both α particles from a given ^{8}Be would be detected. The neutron case is a coincidence measurement. It is assumed that the decay fragment is detected in the silicon, and the probability that the neutron will enter the neutron detector is computed.

For a given decay (i.e. initial fragment and state -- this fixes Q, m, and M), $\Delta\Omega_1$, $\Delta\Omega_2$, E, $\Delta\theta$, and Θ, the angle between the original fragment (either ^{7}Li, ^{8}Li, ^{10}Be, ^{11}Be, or ^{12}B) trajectory and the silicon detector axis, a Monte Carlo calculation was used to determine the probability, $P(E,Q,m,M,\Delta\Omega_1,\Delta\Omega_2,\Delta\theta,\Theta)$, that if the decay fragment (^{6}Li, ^{7}Li, ^{9}Be, ^{10}Be, or ^{11}B, respectively) entered the silicon detector the neutron would enter the neutron detector, under the assumption of isotropic emission in the moving frame of the original fragment. Then, $\varepsilon(E,Q,m,M,\Delta\Omega_1,\Delta\Omega_2,\Delta\theta)$ is given by the following integration:

$$\varepsilon(E,Q,m,M,\Delta\Omega_1,\Delta\Omega_2,\Delta\theta) = \frac{2\pi}{\Delta\Omega_2}\times\int_0^{\Theta_0} P(E,Q,m,M,\Delta\Omega_1,\Delta\Omega_2,\Delta\theta,\Theta)\times\sin(\Theta)\times d\Theta, \quad (B.1)$$

which was computed numerically (see the Fortran code at the end of this appendix), where Θ_0 is the half angle of the neutron detector with solid angle $\Delta\Omega_2$, given by:

$$\Theta_0 = \cos^{-1}(1 - \frac{\Delta\Omega_2}{2\pi}). \qquad (B.2)$$

This geometric efficiency, $\varepsilon(E,Q,m,M,\Delta\Omega_1,\Delta\Omega_2,\Delta\theta)$, was determined separately for neutrons emitted in the direction of the moving system and for neutrons emitted in the opposite direction. The value of $\Delta\theta$ is discussed later in this appendix.

Figure B.1.1 shows the geometric efficiency for detecting neutrons (in coincidence with ^{6}Li) emitted from the 7.456 MeV state of ^{7}Li as a function of the kinetic energy of the emitting ^{7}Li for the solid angles of silicon telescope-1 and neutron detector-1. Both the efficiency for neutrons emitted in the direction of the moving system and for neutrons emitted in the opposite direction are shown. For each of these calculations (i.e. for all five systems being considered and for each direction of neutron emission), an average geometric efficiency, $\langle\varepsilon(Q,m,M,\Delta\Omega_1,\Delta\Omega_2,\Delta\theta)\rangle$, was then obtained by weighting

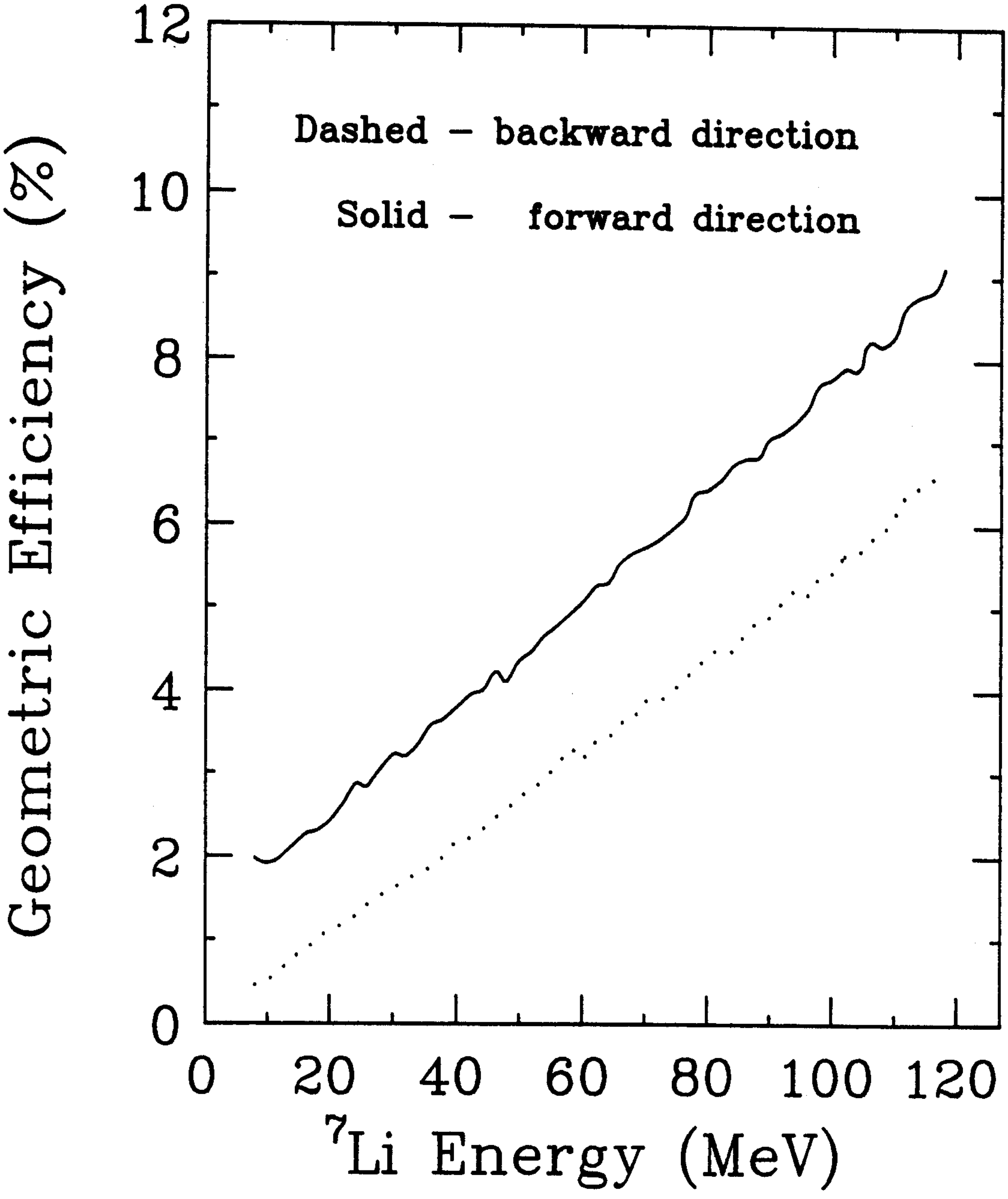

Figure B.1.1 $\varepsilon_n(E)$ for neutrons in coincidence with ^{6}Li, forward and backward relative velocity peaks.

$\varepsilon(E,Q,m,M,\Delta\Omega_1,\Delta\Omega_2,\Delta\theta)$ by the kinetic energy spectrum of the parent fragments, Y(E), which was determined from inclusive data, integrating over energy and dividing by the total yield. That is,

$$\langle\varepsilon(Q,m,M,\Delta\Omega_1,\Delta\Omega_2,\Delta\theta)\rangle = \frac{\int\varepsilon(E,Q,m,M,\Delta\Omega_1,\Delta\Omega_2,\Delta\theta)Y(E)dE}{\int Y(E)dE}. \qquad (B.3)$$

(For simplicity, this geometric efficiency and the related average efficiency are referred to as $\varepsilon_n(E)$ and $\langle\varepsilon_n\rangle$, respectively, throughout this thesis, except in this appendix). This average efficiency had to be calculated separately for each system, for each direction of neutron emission (forward and backward), and for both beam energies used. The geometric efficiency was the same for each beam energy, but the charged particle singles spectra were different. The resulting values for the average efficiencies are listed in Table III.3.3.

Since the silicon telescope and the neutron detector were colinear for the cases under consideration, ideally $\Delta\theta=0$. As discussed in section III.4, the uncertainty in this alignment was ±0.1°. The geometric efficiency obtained when $\Delta\theta=0.1°$ is slightly smaller than that obtained when $\Delta\theta=0.0°$. A much greater effect on the efficiency is caused by the finite-sized beam spot and possible error in centering the beam. The axis of each detector is the line from the fragment source (a point-like target) to the center of the detector. The angle between the two detector axes depends on the position of the point-like fragment source on the finite sized target. Averaging over all possible positions for the point-like source (as limited by the estimated size of the beam spot and beam spot position, as described in section III.4) yields an average effective detector misalignment of about 0.6 degrees.

This is the value of $\Delta\theta$ used in the calculations of the geometric efficiency. The uncertainties given with the average geometric efficiencies reflect the uncertainty in this value of $\Delta\theta$.

The following program was used to calculate $\varepsilon(E,Q,m,M,\Delta\Omega_1,\Delta\Omega_2,\Delta\theta)$:

```
      PROGRAM   geo_eff
C                Nov. 8, 1986.  C. Bloch

C                                        (A,Z) --> (A-1,Z) + n

C  This MONTE CARLOS the efficiency for detecting a neutron emitted from
C  a FRAG(A), given a FRAG(A-1) was detected.

      CHARACTER FNAME*20,dir*1

C  number of integration steps...
      ntheta=100
      monte=1000
      nphi=1

      S=SECNDS(0.)
      III=INT(S)
      pi=3.1415926

      OPEN (UNIT=5,STATUS='OLD',READONLY)

C  Input parameters...
      TYPE *,' Enter the solid angle (in msr) of the neutron
     1 detector'
      READ(5,*) s_angle

      TYPE *,' Enter the solid angle (in msr) of the silicon
     1 detector'
      READ(5,*) sil_sa

      type *,' Enter the angle (deg) between the two detectors.'
      READ(5,*) dtheta

      type *,' Enter the name of the output file.'
      read(5,1010) fname

      type *,' Enter the energy (in MeV) of the decay.'
      READ(5,*) Q
```

```
      type *,' Enter A for the fragment before decay.'
      READ(5,*) a_parent

      type *,'Enter # of integration steps for fragment theta.'
      READ(5,*) ntheta

C  If the angle between the two detector axes is zero, the problem has
C  azimuthal symmetry, and nphi should be left equal to 1
      type *,' Enter # of integration steps for fragment phi.'
      type *,' ( for azimuthal symmetry, enter 1)'
      READ(5,*) nphi

      type *,'Enter # of neutron decays for each frag direction.'
      READ(5,*) monte

      type *,' Enter F for forward peak, B for backward peak.'
      READ(5,1010) dir

      CLOSE(5)

      if(dir.eq.'F'.or.dir.eq.'f') then    !forward peak
        sgn=1.
      else
        sgn=-1.
      endif

C  A for daughter...
      a_daughter = a_parent - 1.

C  Velocities in frame of parent
      dV_n = sqrt(2.*Q/(1./(a_daughter*931.5)+1./939.55))/939.55*30.
      dV_Frag = 939.55*dV_n/(a_daughter*931.5)

C  Determine the condition for "forward" or "backward".  For dtheta=0,
C  the plane separating these hemispheres is determined by the detector
C  normal.  For non-zero dtheta, the normal is between the two detector
C  normals.  Using small angle approximations, the change of the normal
C  from the frag-det. normal is given by...

      dtheta=dtheta*pi/180.      !change to radians
      theta_norm=(dV_n*dtheta-dV_frag*(1.-cos(dtheta)))/
     1          (dV_n+dV_frag)
      theta_norm=theta_norm*180./pi       !converts back to degrees
      type *,' theta_norm=',theta_norm

C  solid angle stuff...
      theta_max  = acosd(1.- sil_sa/(2000.*pi))
      theta_test = acosd(1.-s_angle/(2000.*pi))
C  angle integration step size...
      dcos = (1.-cosd(theta_max+theta_norm))/real(ntheta)
      dphi = 360./real(nphi)

      OPEN (UNIT=11,FILE=FNAME,STATUS='NEW')
```

```
        Do ifake=0,1
          write(11,1001)Ifake,0,0.0
        enddo

C  Select parent energy...
        Do i_energy=2,127 !begin energy loop

          E_parent = real(2*i_energy)
          V = sqrt(2.*E_parent/(A_parent*931.5))*30. !cm/ns

C  Select parent frag direction...
          Do jtheta=0,ntheta-1     !begin parent theta loop
            domega=dcos/2.+dcos*real(jtheta)
            theta=acosd(1.-domega)
            do iphi=0,nphi-1        !begin parent phi loop
              phi=dphi/2.+real(iphi)*dphi

              DO I=1,monte          !monte carlo over neutron directions
                theta_n = acosd(RAN(III))-theta_norm
                phi_n   = 360.*RAN(III)

C  Check to see if daughter is in silicon detector:
                dx=-sgn*dV_Frag*cosd(phi_n)*sind(theta_n)
                dy=-sgn*dV_Frag*sind(phi_n)*sind(theta_n)
                dz=-sgn*dV_Frag*cosd(theta_n)

                x = v*cosd(phi)*sind(theta) + dx
                y = v*sind(phi)*sind(theta) + dy
                z = v*cosd(theta) + dz

                rho = sqrt(x*x + y*y)
                rho_max = z*tand(theta_max)

                if(rho.le.rho_max) then              !Frag in...

                  denom=denom+1.

C  Check to see if neutron is in NEUTRON detector:
C  Shift to new frame, z-axis in neutron detector direction...

                  dx=sgn*dV_n*cosd(phi_n)*sind(theta_n)
                  dy=sgn*dV_n*sind(phi_n)*sind(theta_n)
                  dz=sgn*dV_n*cosd(theta_n)

                  x = v*cosd(phi)*sind(theta) + dx
                  y = v*sind(phi)*sind(theta) + dy
                  z = v*cosd(theta) + dz

                  xprime =  x*cos(dtheta) + z*sin(dtheta)
                  yprime =  y
                  zprime = -x*sin(dtheta) + z*cos(dtheta)

                  rho = sqrt(xprime*xprime + yprime*yprime)
```

```
                 rho_max = zprime*tand(theta_test)

                 if(rho.le.rho_max) then    ! neutron in too!
                   COUNT=COUNT+1.
                 ENDIF
               ENDIF
             ENDDO        !End Monte Carlo over neutron directions

             IF(DENOM.EQ.0.) THEN
               PERCENT=0.
             ELSE
C  denom=# frags detected, count=# neutrons detected, out of #=monte
C  decays.
               PERCENT=COUNT/denom
             ENDIF
             denom=0.
             COUNT=0.

             probability=probability+percent

             percent=0.
           ENDDO                   !End loop over parent phi
         enddo            !End loop over parent theta

         probability=probability/real(ntheta*nphi)

         write(11,1001)I_ENERGY,NINT(probability*100000.),0.0

         probability=0.
       ENDDO              !End loop over parent energy

       CLOSE (11)

1001   format(I,2X,I,2X,f)
1003   format(I2)
1010   format(a)

       stop'PROGRAM DONE'

       end
```

LIST OF REFERENCES

Aj84 F. Ajzenberg-Selove, Nucl. Phys. A413, 1 (1984).

Aj85 F. Ajzenberg-Selove, Nucl. Phys. A433, 1 (1985).

Aw79 T.C. Awes, C.K. Gelbke, B.B. Back, A.C. Mignerey, K.L. Wolf, P. Dyer, H. Breuer, and V.E. Viola, Jr., Phys. Lett. 87B, 43 (1979).

Aw80 T.C. Awes, C.K. Gelbke, G. Poggi, B.B. Back, B. Glagola, H. Breuer, V.E. Viola, Jr., and T.J.M. Symons, Phys. Rev. Lett. 45, 513 (1980).

Aw81a T.C. Awes, G. Poggi, C.K. Gelbke, B.B. Back, B.G. Glagola, H. Breuer, and V.E. Viola, Jr., Phys. Rev. C 24, 89 (1981).

Aw81b T.C. Awes, G. Poggi, S. Saini, C.K. Gelbke, R. Legrain, and G.D. Westfall, Phys. Lett. 103B, 417 (1981).

Aw82 T.C. Awes, S. Saini, G. Poggi, C.K. Gelbke, D. Cha, R. Legain, and G.D. Westfall, Phys. Rev. C 25, 2361 (1982).

Ba80 B.B. Back, K.L. Wolf, A.C. Mignerey, C.K. Gelbke, T.C. Awes, H. Breuer, V.E. Viola, and P. Dyer, Phys. Rev. C 22, 1927 (1980).

Ba83 F.C. Barker, Can. J. Phys. 61, 1371 (1983).

Be83 G. Bertsch and P.J. Siemens, Phys. Lett. 126B, 9 (1983).

Bl76 M. Blann, A. Mignerey, and W. Scobel, Nukleonika 21, 335 (1976).

Bl81 M. Blann, Phys. Rev. C 23, 205 (1981).

Bl85 M. Blann, Phys. Rev. C 31, 1245 (1985).

Bl86 C. Bloch, W. Benenson, E. Kashy, D.J. Morrissey, R.A. Blue, R.M. Ronningen, and H. Utsunomiya, Phys. Rev. C 34, 850 (1986).

Bl87a C. Bloch, W. Benenson, A.I. Galonsky, E. Kashy, J. Heltsley, L. Heilbronn, M. Lowe, B. Remington, D.J. Morrissey, and J. Kasagi, MSUCL-592 and accepted by Phys. Rev. C (1987).

Bl87b C. Bloch and E. Kashy, MSUCL-594 and submitted to Phys. Rev. C (1987).

Bo80 J.P. Bondorf, J.N. De, G. Fai, A.O. Karvinen, B. Jakobsson, and

J. Randrup, Nucl. Phys. A333, 285 (1980).

Bo83 D. Boal, Phys. Rev. C 28, 2568 (1983).

Bo84a D. Boal, Phys. Rev. C 28, 119 (1984).

Bo84b D. Boal, Phys. Rev. C 30, 749 (1984).

Bu68 G. Butler, J. Cerny, S.W. Cosper, and R.L. McGrath, Phys. Rev. 166, 1096 (1968).

Ca85 G. Caskey, A. Galonsky, B. Remington, M.B. Tsang, C.K. Gelbke, A. Kiss, F. Deak, Z. Seres, J.J. Kolata, J. Hinnefeld, and J. Kasagi, Phys. Rev. C 31, 1597 (1985).

Ca86 G. Caskey, A. Galonsky, B. Remington, F. Deak, A. Kiss, and Z. Seres, Phys. Rev. C 34, 506 (1986).

Ce79 R.A. Cecil, B.D. Anderson, and R. Madey, Nucl. Instrum. and Meth. 161, 439 (1979).

Ch83 C.B. Chitwood, D.J. Fields, C.K. Gelbke, W.G. Lynch, A.D. Panagiotou, M.B. Tsang, H. Utsunomiya, and W.A. Friedman, Phys. Lett. 131B, 289 (1983).

Ch85 C.B. Chitwood, J. Aichelin, D.H. Boal, G. Bertsch, D.J. Fields, W.G. Lynch, M.B. Tsang, J.C. Shillcock, T.C. Awes, R.L. Ferguson, F.E. Obenshain, F. Plasil, R.L. Robinson, and G.R. Young, Phys. Rev. Lett. 54, 302 (1985).

Ch86a C.B. Chitwood, C.K. Gelbke, J. Pochodzalla, Z. Chen, D.J. Fields, W.G. Lynch, R. Morse, M.B. Tsang, D.H. Boal, and J.C. Shillcock, Phys. Lett. 172B, 27 (1986).

Ch86b C.B. Chitwood, D.J. Fields, C.K. Gelbke, D.R. Klesch, W.G. Lynch, M.B. Tsang, T.C. Awes, R.L. Ferguson, F.E. Obenshain, F. Plasil, R.L. Robinson, and G.R. Young, Phys. Rev. C 34, 858 (1986).

Cu80 J. Cugnon, Phys. Rev. C 22, 1885 (1980).

Cu83 M.W. Curtin, H. Toki, and D.K. Scott, Phys. Lett. 123B, 289 (1983).

Da86 N.R. Dagdeviren, Phys. Lett. 176B, 283 (1986).

De86a F. Deak, A. Kiss, Z. Seres, G. Caskey, A. Galonsky, B. Remington, C.K. Gelbke, M.B. Tsang, and J.J. Kolata, MSUCL-561 and submitted to Nucl. Phys. (1986).

De86b F. Deak, A. Kiss, Z. Seres, G. Caskey, A. Galonsky, and B. Remington, MSUCL-575 and submitted to Phys. Rev. Lett. (1986).

Do78 G.D. Doolen, Phys. Rev. Lett. 40, 1695 (1978).

Er58 T. Ericson and V. Strutinski, Nucl. Phys. 8, 284 (1958).

Ey78 Y. Eyal, A. Gavron, I. Tserruya, Z. Fraenkel, Y. Eisen, S. Wald, R. Bass, G.R. Gould, G. Kreyling, R. Renfordt, K. Stelzer, R. Zitzmann, A. Gobbi, U. Lynen, H. Stelzer, I. Rode, and R. Bock, Phys. Rev. Lett. 41,625 (1978).

Fa82 G. Fai and J. Randrup, Nucl. Phys. A381, 557 (1982).

Fa83 G. Fai and J. Randrup, Nucl. Phys. A404, 551 (1983) and L.P. Csernai, private communication.

Fa85 M. Fatyga, K. Kwiatkowski, V.E. Viola, C.B. Chitwood, D.J. Fields, C.K. Gelbke, W.G. Lynch, J. Pochodzalla, M.B. Tsang, and M. Blann, Phys. Rev. Lett. 55, 1376 (1985).

Fi67 M.E. Fisher, Physics (N.Y.) 3, 355 (1967).

Fi84 D.J. Fields, W.G. Lynch, C.B. Chitwood, C.K. Gelbke, M.B. Tsang, H. Utsunomiya, and J. Aichelin, Phys. Rev. C 30, 1912 (1984).

Fi86 D.J. Fields, W.G. Lynch, T.K. Nayak, M.B. Tsang, C.B. Chitwood, C.K. Gelbke, R. Morse, J. Wilczynski, T.C. Awes, R.L. Ferguson, F. Plasil, F.E. Obenshain, and G.R. Young, Phys. Rev. C 34, 536 (1986).

Fi87 D.J. Fields, C.K. Gelbke, W.G. Lynch, and J. Pochodzalla, MSUCL-576 and to be published.

Fr83a W.A. Friedman and W.G. Lynch, Phys. Rev. C 28, 16 (1983).

Fr83b W.A. Friedman and W.G. Lynch, Phys. Rev. C 28, 950 (1983).

Ga83 A. Gavron, J.R. Beene, B. Cheynis, R.L. Ferguson, F.E. Obenshain, F. Plasil, G.R. Young, G.A. Petitt, C.F. Maguire, D.G. Sarantites, M. Jaaskelainen, and K. Geoffroy-Young, Phys. Rev. C 27, 450 (1983).

Ge77 C.K. Gelbke, M. Bini, C. Olmer, D.L. Hendrie, J.L. Laville, J. Mahoney, M.C. Mermaz, D.K. Scott, and H.H. Wieman, Phys. Lett. 71B, 83 (1977).

Ge78 K.A. Geoffroy, D.G. Sarantites, L. Westerberg, J.H. Barker, D.C. Hensley, R.A. Dayras, and M.L. Halbert, Bull. Am. Phys. Soc. 23, 950 (1978).

Go74 A.S. Goldhaber, Phys. Lett. 53B, 306 (1974).

Go78 A.S. Goldhaber, Phys. Rev. C 17, 2243 (1978).

Gr77 D.H.E. Gross and J. Wilczynski, Phys. Lett. 67B, 1 (1977).

Ha86 D. Hahn and H. Stöcker, LBL - preprint LBL-22378 (1986) and submitted to Nucl. Phys.

Ha68 G.D. Harp, J.M. Miller, and B.J. Berne, Phys. Rev. 165, 1166 (1968).

Ha71 G.D. Harp and J.M. Miller, Phys. Rev. C 3, 1847 (1971).

Hi78 D.L. Hillis, O. Christensen, B. Fernandez, A.J. Ferguson, J.D. Garrett, G.B. Hagemann, B. Herskind, B.B. Back, and F. Folkmann, Phys. Lett. 78B, 405 (1978).

Hi79 D. Hilscher, J.R. Birkelund, A.D. Hoover, W.U. Schroder, W.W. Wilke, J.R. Huizenga, A.C. Mignerey, K.L. Wolf, H.F. Breuer, and V.E. Viola, Jr., Phys. Rev. C 20, 576 (1979).

Hi84a D. Hilscher, E. Holub, G. Ingold, U. Jahnke, H. Orf, H. Rossner, W.P. Zank, W.U. Schroder, H. Gemmeke, K. Keller, L. Lassen, and W. Lucking, in Proceedings of the Workshop on Coincidence Particle Emission from Continuum States in Nuclei, Bad Honnef, 1984, edited by H. Machner and P. Jahn (World-Scientific, Singapore, 1984), p. 268.

Hi84b A.S. Hirsch, A. Bujak, J.E. Finn, L.J. Gutay, R.W. Minich, N.T. Porile, R.P. Scharenberg, B.C. Stringfellow, and F. Turkot, Phys. Rev. C 29, 508 (1984).

Ho83 E. Holub, D. Hilscher, G. Ingold, U. Jahnke, H. Orf, and H. Rossner, Phys. Rev. C 28, 252 (1983).

Ho86 E. Holub, D. Hilscher, G. Ingold, U. Jahnke, H. Orf, H. Rossner, W.P. Zank, W.U. Schroder, H. Gemmeke, K. Keller, L. Lassen, and W. Lucking, Phys. Rev. C 33, 143 (1986).

Ja83 B.V. Jacak, G.D. Westfall, C.K. Gelbke, L.H. Harwood, W.G. Lynch, D.K. Scott, H. Stocker, M.B. Tsang, and T.J.M. Symons, Phys. Rev. Lett. 51, 1846 (1983).

Ja84 B.V. Jacak, H. Stocker, and G.D. Westfall, Phys. Rev. C 29, 1744 (1984).

Ja86 U. Jahnke, G. Ingold, D. Hilscher, M. Lehmann, E. Schwinn, and P. Zank, Phys. Rev. Lett. 57, 190 (1986).

Ka85 J. Kasagi, B. Remington, A. Galonsky, F. Haas, J.J. Kolata, L. Satkowiak, M. Xapsos, R. Racca, and F.W. Prosser, Phys. Rev. C 31, 858 (1985).

Ki87 A. Kiss, F. Deak, Z. Seres, G. Caskey, A. Galonsky, L. Heilbronn, B. Remington, and J. Kasagi, submitted to Phys. Lett.

Ko77 S.E. Koonin, Phys. Lett. 70B, 43 (1977).

Ku64 R.J. Kurtz, University of California Radiation Lab Internal Report No. UCRL-11339, (1964).

Le59 K.J. Le Couteur and D.W. Lang, Nucl. Phys. 13, 32 (1959).

Ly83 W.G. Lynch, C.B. Chitwood, M.B. Tsang, D.J. Fields, D.R. Klesch, C.K. Gelbke, G.R. Young, T.C. Awes, R.L. Ferguson, F.E. Obenshain, F. Plasil, R.L. Robinson, and A.D. Panagiotou, Phys. Rev. Lett. 51, 1850 (1983).

Me74 A. Menchaca-Rocha, Nucl. Instrum. and Meth. 114, 425 (1974).

Me80 W.G. Meyer, H.H. Gutbrod, C. Lukner, and A. Sandoval, Phys. Rev. C 22, 179 (1980).

Mo84 D.J. Morrissey, W. Benenson, E. Kashy, B. Sherrill, A.D. Panagiotou, R.A. Blue, R.M. Ronningen, J. van der Plicht, and H. Utsunomiya, Phys. Lett. 148B, 423 (1984).

Mo85 D.J. Morrissey, W. Benenson, E. Kashy, C. Bloch, M. Lowe, R.A. Blue, R.M. Ronningen, B. Sherrill, H. Utsunomiya, and I. Kelson, Phys. Rev. C 32, 877 (1985).

Mo86 D.J. Morrissey, C. Bloch, W. Benenson, E. Kashy, R.A. Blue, R.M. Ronningen, and R. Aryaeineyad, Phys. Rev. C 34, 761 (1986).

Ne82 J. Negele, Rev. Mod. Phys. 54, 913 (1982).

Oc78 W.J. Ockels, Z. Phys. A 286, 181 (1978).

Pa84 A.D. Panagiotou, M.W. Curtin, H. Toki, D.K. Scott, and P.J. Siemens, Phys. Rev. Lett. 52, 496 (1984).

Pa85 A.D. Panagiotou, M.W. Curtin, and D.K. Scott, Phys. Rev. C 31, 55 (1985).

Pe77 J. Peter, M. Berlanger, C. Ngo, B. Tamain, B. Lucas, C. Mazur, M. Ribrag, and C. Signarbieux, Z. Phys. A283, 413 (1977).

Po71 A.M. Poskanzer, G.W. Butler, E.K. Hyde, Phys. Rev. 3, 882 (1971).

Po85a J. Pochodzalla, W.A. Friedman, C.K. Gelbke, W.G. Lynch, M. Maier, D. Ardouin, H. Delagrange, H. Doubre, C. Gregoire, A. Kyanowski, W. Mittig, A. Peghaire, J. Peter, F. Saint-Laurent, Y.P. Viyogi, B. Zwieglinski, G. Bizard, F. Lefebvres, B. Tamain, and J. Quebert, Phys. Rev. Lett. 55, 177 (1985); Phys. Lett. 161B, 275 (1985).

Po85b J. Pochodzalla, W.A. Friedman, C.K. Gelbke, W.G. Lynch, M. Maier, D. Ardouin, H. Delagrange, H. Doubre, C. Gregoire, A. Kyanowski, W. Mittig, A. Peghaire, J. Peter, F. Saint-Laurent, Y.P. Viyogi, B. Zwieglinski, G. Bizard, F. Lefebvres, B. Tamain, and J. Quebert, 161B, 256 (1985).

Po86a J. Pochodzalla, C.B. Chitwood, D.J. Fields, C.K. Gelbke, W.G. Lynch, M.B. Tsang, D.H. Boal, and J.C. Shillcock, Phys. Lett. 174B, 36 (1986).

Po86b J. Pochodzalla, C.K. Gelbke, C.B. Chitwood, D.J. Fields, W.G. Lynch, M.B. Tsang, and W.A. Friedman, Phys. Lett. 175B, 275 (1986).

Pu77 F. Puhlhofer, Nucl. Phys. A280, 267 (1977).

Ra81 J. Randrup and S.E. Koonin, Nucl. Phys. A356, 223 (1981).

Re86 B.A. Remington, G. Caskey, A. Galonsky, C.K. Gelbke, L. Heilbronn, J. Heltsley, M.B. Tsang, F. Deak, A. Kiss, Z. Seres, J. Kasagi and J.J. Kolata, Phys. Rev. C 34, 1685 (1986) and B.A. Remington, Ph.D. Thesis, Michigan State University (1986).

Sh85 B. Sherrill, Ph.D. Thesis, Michigan State University (1985).

So86 L.G. Sobotka, D.G. Sarantites, H. Puchta, F.A. Dilmanian, and M. Jaaskelainen, M.L. Halbert, J.H. Barker, J.R. Beene, R.L. Ferguson, D.C. Hensley, and G.R. Young, Phys. Rev. C 34, 917 (1986).

St74 R.G. Stokstad, in Proceedings of the International Conference on Reactions Between Complex Nuclei, Nashville, Tennessee, edited by R.L. Robinson, F.K. McGowan, J.B. Ball, and J.H. Hamilton. Eds., (North-Holland, Amsterdam, 1974), Vol. II, p. 327.

Va85 A. Vander Molen, R. Au, R. Fox, and T. Glynn, Nucl. Instrum. and Meth. A236, 359 (1985).

We76 G.D. Westfall, J. Gosset, P.J. Johansen, A.M. Poskanzer, W.G. Meyer, H.H. Gutbrod, A. Sandoval, and R. Stock, Phys. Rev. Lett. 37, 1202 (1976).

We77 R. Weiner and M. Westrom, Nucl. Phys. A286, 282 (1977).

We78a G.D. Westfall, R.G. Sextro, A.M. Poskanzer, A.M. Zebelman, G.W. Butler, and E.K. Hyde, Phys. Rev. C 17, 1368 (1978).

We78b L. Westerberg, D.G. Sarantites, D.C. Hensley, R.A. Dayras, M.L. Halbert, and J.H. Barker, Phys. Rev. C 18, 796 (1978).

We82 G.D. Westfall, B.V. Jacak, N. Anantaraman, M.W. Curtin, G.M. Crawley, C.K. Gelbke, B. Hasselquist, W.G. Lynch, D.K. Scott, M.B. Tsang, M.J. Murphy, T.J.M. Symons, R. Legrain, and T.J. Majors., Phys. Lett. 116B, 118 (1982).

We84 G.D. Westfall, Z.M. Koenig, B.V. Jacak, L.H. Harwood, G.M. Crawley, M.W. Curtin, C.K. Gelbke, B. Hasselquist, W.G. Lynch, A.D. Panagiotou, D.K. Scott, H. Stocker, and M.B. Tsang, Phys. Rev. C 29, 861 (1984).

Wo72 G.J. Wozniak, H.L. Harney, K.H. Wilcox, and J. Cerny, Phys. Rev. Lett. 28, 1278 (1972).

Wo74 G.J. Wozniak, N.A. Jelley and J. Cerny, Nucl. Instrum. and Meth. 120, 29 (1974).

Wo85 K.L Wolf, J.P. Sullivan, G.M. Berkowitz, H.L. Kent, K.M. Pierpoline, B.S. Potts, C.T. Spillett, and J. Shoemaker, "Intermediate Mass Fragment Emission", presented at the Symposium on Nuclear Physics at Oaxtepec, Mexico, 8-10 January, 1985.

Xu86 H.M. Xu, D.J. Fields, W.G. Lynch, M.B. Tsang, C.K. Gelbke, M.R. Maier, D.J. Morrissey, J. Pochodzalla, D.G. Sarantites, L.G. Sobotka, M.L. Halbert, D.C. Hensley, D. Hahn, and H. Stocker, Phys. Lett. 182B, 155 (1986).

Za86 W.P. Zank, D. Hilscher, G. Ingold, U. Jahnke, M. Lehmann, and H. Rossner, Phys. Rev. C 33, 519 (1986).

Zi80 J.F. Ziegler, Handbook of Stopping Cross-sections, (Pergamon, New York, 1980).